Development of a three-photon microscope for awake and behaving non-human primates

Marie Guillemant

université PARIS-SACLAY

Development of a three-photon microscope for awake and behaving non-human primates.

Développement d'un microscope à trois photons adapté à l'imagerie du primate non humain vigile.

Thèse de doctorat de l'université Paris-Saclay

École doctorale n°568 : signalisations et réseaux intégratifs en biologie (Biosigne)
Spécialité de doctorat : Neurosciences
Graduate School : Sciences de la vie et santé, Référent : Faculté de Médecine

Thèse préparée dans l'unité de recherche UNICOG (Université Paris-Saclay, Inserm, CEA), sous la direction de Béchir Jarraya, directeur de recherche et praticien hospitalier, INSERM, NeuroSpin et la co-direction de Timo van Kerkoerle, chargé de recherche, CEA, NeuroSpin

Thèse soutenue à Paris-Saclay, le 16 mars 2023, par

Marie GUILLEMANT

Composition du jury
Membres du jury avec voix délibérative

Alexandra Fragola Professeure à l'Université Paris-Saclay, Institut des Sciences Moléculaires d'Orsay (ISMO)	Présidente
Anitha Pasupathy Professeure des universités, Université de Washington	Rapporteur & Examinatrice
Laurent Bourdieu Directeur de recherche, CNRS, Institut de Biologie de l'Ecole Normale Supérieure (IBENS)	Rapporteur & Examinateur
Wim Vanduffel Directeur de recherche, Leuven Brain Institute	Examinateur

THESE DE DOCTORAT
NNT : 2023UPSASL025

université PARIS-SACLAY

ÉCOLE DOCTORALE
Signalisations et réseaux intégratifs en biologie (BIOSIGNE)

Titre : Développement d'un microscope à trois photons adapté à l'imagerie du primate non humain vigile.

Mots clés : microscope multiphotonique, primate non humain, vigile, fluorescence, dure-mère

Résumé : La microscopie multiphotonique est devenue un outil essentiel pour étudier l'activité fonctionnelle de la souris mais son application à des animaux plus grands se heurte à plusieurs obstacles. Il serait particulièrement avantageux de pouvoir l'appliquer aux macaques, car ils représentent un modèle animal de choix pour comprendre les mécanismes neuronaux des fonctions cognitives de haut niveau, telles que l'attention, la mémoire et la conscience. L'un des principaux facteurs limitant à l'imagerie chez les grands animaux est la dure-mère. Cette couche de tissu épaisse et opaque protège le cerveau, mais elle est si épaisse chez les grands animaux qu'elle entrave l'imagerie. Elle est donc couramment enlevée mais cela conduit à une préparation hautement invasive et instable. L'objectif principal de ce travail est d'étudier la possibilité d'enregistrer l'activité fonctionnelle du cortex du macaque rhésus à travers la dure-mère naturelle.

Une installation de microscopie multiphotonique a été conçue avec des chemins optiques de microscopie à deux et trois photons pour pouvoir faire des enregistrements sur des primates non humains vigiles. La fréquence de répétition du laser est de 2MHz, ce qui permet une profondeur d'imagerie maximale à l'intérieur du cortex de 520μm à 960nm et 715μm à 1300nm en la présence d'une dure-mère de 120μm d'épaisseur à la surface. Le champ de vision est de 620x630μm2 avec une fréquence d'acquisition de 7,8Hz en utilisant un balayage unidirectionnel. En plus de cette installation, des implants chirurgicaux ont été développés pour une imagerie stable sur le long-terme de sujets vigiles.

En utilisant une étude *ex vivo* de la dure-mère d'un macaque rhésus, les aberrations optiques induites par celle-ci ont été étudiées en mesurant la diminution de la résolution spatiale du microscope pour une épaisseur variable de dure-mère. Ceci révèle qu'elle n'a pas d'impact significatif sur la résolution pour une épaisseur allant jusqu'à 150μm à 1300nm. La longueur d'atténuation effective de la dure-mère naturelle est estimée à 56.5$\pm$10.1μm à 960nm et 80.7$\pm$5.3μm à 1300nm. Ces valeurs sont utilisées pour modéliser la profondeur maximale d'imagerie en fonction de la fréquence de répétition du laser et de l'épaisseur de la dure-mère. Ce modèle est ajusté et validé à l'aide de données *in vivo* provenant de deux primates non humains. La longueur d'atténuation effective de la dure-mère naturelle et d'une repousse de tissu après une durectomie (appelée "néomembrane") sont étudiées. Des enregistrements fonctionnels ont été réalisés chez la souris et prétraités avec Suite2P. Les paramètres d'injection virale ont été testés chez trois macaques et nous avons enregistré l'activité structurelle et fonctionnelle de neurones pour l'un d'eux au moment de l'étude.

Enfin, la comparaison entre l'utilisation de la microscopie à deux ou trois photons pour l'étude du primate non humain est discutée.

En conclusion, nous avons mis en place et optimisé un microscope multiphotonique pour l'imagerie vigile et à long-terme du cortex de primates non humains et montré qu'il était possible d'enregistrer le cortex jusqu'à plus de 700μm de profondeur (ce qui correspond aux couches L2/L3) tout en gardant la dure-mère naturelle en place.

Title : Development of a three-photon microscope for awake and behaving non-human primates.
Keywords : multi-photon microscope, non-human primates, awake imaging, fluorescence, dura mater

Abstract : Multi-photon microscopy has become a standard technique to study the structural and functional activity in mice but it faces obstacles to be applied in larger animals. It would be particularly advantageous to be able to apply it to macaque monkeys, as they are the animal model of choice to understand the neural mechanisms of high-level cognitive functions such as selective attention, working memory and consciousness. One of the main limiting factors for imaging in larger animals is the dura mater. This tough and opaque layer of tissue protects the brain but is so thick in larger animals that it obstructs imaging. It is therefore commonly removed but this leads to a highly invasive and unstable preparation. The main aim of the current work is to investigate the possibility to record functional activity from the cortex of the rhesus macaque monkey through the natural dura.
A multi-photon microscopy setup has been designed with a two-photon and a three-photon microscopy optical paths to record from awake macaque monkeys. The repetition rate of the laser is 2MHz which allows a maximum imaging depth inside the cortex of 520μm at 960nm and 715μm at 1300nm with an additional 120μm-thick layer of dura mater at the surface. Resonance-galvo scanning is used to allow a maximal frame rate of 15.6Hz at a field of view of 620x630μm^2. In addition to the setup, surgical implants have been developed for long-term and awake imaging.
Using an *ex vivo* study of dura mater from a macaque monkey, the induced optical aberrations are studied by measuring the decrease in spatial resolution of the setup for a varying thickness of dura mater. This reveals that it has no significant impact on the spatial resolution for a thickness up to 150μm at 1300nm. The effective attenuation length of the dura mater is estimated to be 56.5$\pm$10.1μm at 960nm and 80.7$\pm$5.3μm at 1300nm. These measurements are used to model the maximum imaging depth that can be reached according to the repetition rate of the laser and the thickness of the dura.
This model is adjusted and validated using *in vivo* data from two non-human primates. The effective attenuation length of the natural dura mater and of a regrowth of tissue following a durectomy (called a 'neomembrane') are investigated.
Functional recordings have been performed in mice and preprocessed using Suite2P. Viral injection parameters have been tested in three macaque monkeys and we have so far recorded the *in vivo* structural and functional activity of neurons in one.
Finally, the comparison between the use of two- and three-photon microscopy to study non-human primates is discussed.
In conclusion, we have set up and optimized a multi-photon microscope for long-term awake imaging of the cortex of non-human primates and shown that it was possible to record down to over 700μm into the cortex (which corresponds to the layers L2/L3) while imaging through the natural dura mater or a neomembrane.

Acknowledgements

First, I would like to thank Timo for entrusting me with this project. When I came to you I did not know anything about neuroscience and you took the time to explain me a lot of the concepts and to introduce me to the relevant literature throughout the PhD. You have always made yourself available to discuss regularly or to help with the project.
Béchir, thank you for following the project throughout the PhD and for sharing your experience and knowledge, you have been a great support to me and the project.
To Wim and Stefan, the members of my thesis committee, thank you very much for our annual meetings that have always been very useful to gain some perspective on our project and thank you for sharing your experience.
To the members of the jury, thank you for taking the time to read and assess my thesis. Thank you for the insightful feedback and enjoyable discussions.
Thank you Emmanuel for your valuable feedback and help on the projects, I have always enjoyed our meetings and discussions.
Marion, you have been a great mentor to teach me about working with monkeys : how to train them but also how to understand and care for them. Thank you for making yourself available and for all your help on my projects.
Marie and Joachim, I have enjoyed working alongside you and learning from you about neuroscience. Thank you for introducing me to bouldering, it has become a great way to escape over time.
Jeremy, thank you for helping us turning our ideas into reality.
Melissa, Maxime and Marion, thank you for making our dark hallway livelier and enjoyable.
Davide and Erwan, thank you for always taking the time to share your experience and help us.
Fabrice, thank you very much for all your help and support.
Thank you Adrien for listening to me and for coaching and motivating me throughout the PhD, you have been a great support.

Table des matières

Acronymes

2PM Two-photon microscopy.

3PM Three-photon microscopy.

EAL Effective attenuation length.

ETL Electrically tunable lens.

FWHM Full-width at half maximum.

GECI genetically encoded calcium indicators.

HWP Half-wave plate.

MPM Multi-photon microscopy.

NHP Non-human primate.

OPA Optical parametric amplifier.

PMT Photomultiplier tube.

PSF Point spread function.

ROI Region of interest.

SBR Signal-to-background ratio.

SHG Second harmonic generation.

SNR Signal-to-noise ratio.

1 - OVERVIEW

Neuroscience or the science of understanding the brain has progressed hand in hand with the development of imaging tools. Different imaging technologies can be used to study the brain and its working mechanisms at different scales. Functional magnetic resonance imaging shows the brain activity at the meso scale over time, showing the brain regions involved in various mechanisms as well as their dynamics. In order to study the activity of single neurons, other recording technologies such as electrophysiology have been developed where electrodes are implanted into the cortex to record the local electric field generated by neurons.

As an addition to the previously cited techniques, multi-photon microscopy (MPM) has recently been developed, which can be used to record the neuronal response of a complete local population of neurons at the single cell resolution. Two-photon microscopy (2PM) has revolutionized neuroscience in mice thanks to the development of both the optical imaging technology and fluorescent markers, turning neuronal functional activity into a fluorescent signal that can be recorded to be interpreted. An overview of these technological developments and their potential is given in **Chapter 2.1**. Yet, despite the large adoption of MPM by neuroscientists using a mouse model, the technology meets resistance with larger animal models. Although the mouse is a very important animal model for human neuroscience, it would be advantageous to be able to apply MPM in non-human primates (NHPs) as well, and in particular in macaque monkeys, as this is generally considered as the animal model of choice to investigate the neural correlates of high-level cognitive functions [1] [2] [3].

The aim of this thesis is to develop and optimize a robust multi-photon microscope setup suited for long-term calcium imaging in the cortex of awake macaque monkeys. One crucial limitation for MPM for NHPs is the dura mater : a thick layer of scattering tissue that covers the brain. This layer is generally removed for optical imaging experiments in NHPs, but this leads to a highly invasive and unstable preparation. The current thesis aims to investigate the possibility to leave the natural dura in place, and image through it, as is commonly done in mice. For that, a dedicated microscope has been developed that allows an extended imaging depth while maintaining relatively large field of view (to allow imaging of large number of neurons) and a high frame rate (to reliably correct for the rapid motion artefacts common in awake experiments). The setup allows both two- and three-photon imaging, where three-photon imaging is thought to allow a substantial increase of the maximum imaging depth relative to two-photon imaging. Furthermore, the setup uses a relatively low repetition rate of the laser (the number of laser pulses per second), allowing to maximize the energy per laser pulse while remaining below

the power limit where thermal damage would take place.

The different components of a multi-photon microscope as well as the main imaging parameters are described and explained in **Chapter 2.2**. In **Chapter 3**, the technical development of the setup is detailed and its performance is tested and quantified.

In **Chapter 4** the imaging properties of the dura mater are investigated *ex vivo* using a sample of post-mortem NHP dura mater that is placed in a solution of agarose and polystyrene fluorescent beads. Its effective attenuation length (EAL) is first estimated to model the signal loss due to the presence of the dura mater and the corresponding loss in maximum imaging depth inside the cortex. Then, the optical aberrations caused by the membrane are characterized by measuring the apparent size of the fluorescent polystyrene beads that are below different thicknesses of dura mater.

In parallel to a dedicated MPM imaging setup, an imaging chamber and a headpost have been developed to perform MPM in macaque monkeys. With that, *in vivo* imaging of a natural dura has been performed and compared to the post-mortem study. The vasculature of two macaque monkeys has been imaged using fluorescein isothiocyanate-dextran to estimate the maximum depth of imaging with the dura in place. Finally, a proof of concept of MPM imaging in awake NHP has been established as well (**Chapter 5**).

2 - BACKGROUND

2.1 INTRODUCTION TO MULTI-PHOTON MICROSCOPY

2.1.1 The start of multi-photon microscopy in neuroscience

Multi-photon microscopy (MPM) was first demonstrated in the 1990s [4] [5]. It presented two main advantages over single-photon microscopy : intrinsic optical sectioning and the use of a larger excitation wavelength (more details in Section 2.2). The former leads to a greater collection efficiency despite scattering and enables deeper imaging in tissue and the tissue is less absorbent in the near infra-red than in the visible range of the light spectrum so the later contributes to deeper imaging and lower imaging power.

The adoption of MPM by neuroscientists was made possible by the simultaneous development of the imaging technology and fluorescent probes. A fluorescent probe is a molecule that becomes fluorescent under specific conditions that can be studied using MPM. On the one hand, plug-and-play two-photon microscopes have been developed and made affordable by companies making it easier for laboratories and biologists to use them without requiring prior knowledge in optics. On the other hand, a wide variety of fluorescent probes have been developed to investigate various questions.

Two of the categories of fluorescent probes that are used in neuroscience are the **voltage sensitive dyes** and the **genetically encoded calcium indicators** (GECIs) such as GCaMP indicators. The former are bound to the membrane of neurons and their absorption or emission spectrum varies with the potential going through the membrane. The later become fluorescent as they bind to calcium ions. Thus, both probes can be used to monitor and record the functional activity of neurons. One advantage with respect to electrophysiology is that the spiking activity, albeit with an indirect measure in the case of GECIs, of all the neurons within the field of view can be recorded simultaneously [6]. The development of fluorescent probes has broadened the applications of fluorescent microscopy such as MPM. In neuroscience, fluorescent probes can be used to trace the connectivity of a large number of neurons [7], record from specific neuromodulators [8] or be restricted to the soma and reduce the background fluorescence due to neuropil [9] for example. Recording the functional activity of neurons can be achieved with the use of voltage sensitive dies [10] or calcium indicators such as GCaMP. It is a

protein that fluoresces in the green range of the visible spectrum when it binds to calcium ions, Ca^{2+}. Indeed, the variation of the concentration of calcium ions in neurons correlates with their spiking activity [11].
In conclusion, thanks to fluorescent probes such as GCaMP and the use of fluorescence microscopy, the intensity of the fluorescent signal becomes a measure of the neuronal activity.

2.1.2 Two-photon microscopy : unlocking new potentials

In cognitive neuroscience, electrophysiological probes such as Utah arrays [12] [13] allow the functional recording of single cells in an acute or chronic manner. Besides, optical imaging such as light sheet microscopy combined with clearing techniques of post-mortem tissue [14] allow to visualize populations of neurons at the single-cell resolution which can be used to study the different cell types and reconstruct connectomes. Combined, these techniques can provide valuable information about the working principles of brain mechanisms such as vision, attention or consciousness. Yet, these studies cannot be done simultaneously and electrophysiology techniques do not permit to choose the neurons one want to study or the study of a large population of neurons at once with the knowledge of the associated micro-circuit. MPM can bridge this gap thanks to the association of a chronic imaging technique able to image several hundreds of micrometers deep into tissue with fluorescent indicators specific to either a cell type or representative of the cellular functional activity.

MPM combined with fluorescent probes allows **single-cell resolution** and even the visualization of axons [15]. This is comparable to other imaging techniques and electrophysiology. However, using 2PM, over **ten thousand neurons** have been imaged simultaneously down to 500μm deep in the mouse cortex [6]. The nominal field of view of 2PM is about 500x500 to 1000x1000μm^2 and several planes can be imaged simultaneously to further increase it although this is at the expense of the imaging speed [6] [16]. In addition, the **complete population of neurons** is labelled, independently of their spiking activity. This is not the case for electrophysiology and can be used for studies interested in mapping an area for various stimuli properties or investigating the proportion of neurons responding to specific stimuli [17].
MPM also offers visual information that helps **tracking cells** throughout a session despite motion artefacts and over multiple sessions [18] [16] [19].

Finally, efforts in miniaturization represent a technological feat and have led to MPM of freely-moving animals which opens up new perspectives to study animals in a natural setting, while they are interacting with other individuals or sleeping for

example [20] [21] [22] [23].

2.1.3 Multi-photon microscopy in larger animals than mice

2PM is a technology that is perfectly suited for small animals such as mice. It is common to image down to 500μm which is enough to record from the first three layers of the cortex [24] and it is possible to image the full cortical column under specific conditions [25] [26]. However, in larger animals 2PM only allows imaging the most superficial layers.
The dura, an opaque membrane that covers the brain, is very thin in mice (about 10μm) but becomes thicker for rats and NHPs. This is already a known issue for intrinsic imaging and voltage sensitive dies recordings where it is possible to record the cortex through the natural dura in rodents and cats [27] [28] but not in macaque monkeys for which the dura has to be surgically removed [29] [30].
Similarly, the dura of NHPs is commonly surgically removed to perform 2PM imaging and any regrowth of a neomembrane is detrimental to the imaging quality and maximum depth that can be reached [16] [31] [15] [32]. Even 100μm of neomembrane is enough to compromise 2PM imaging with a regular two-photon microscope [16] [33].
Some examples of 2PM in NHPs include the laboratory of Shiming Tang that has been successfully imaging macaques monkeys in the areas V1 and V4, up to 600μm deep into the cortex [34] [16] [35] [36]. However, this remains challenging and three-photon microscopy (3PM) may be a solution for these larger animals.

A significantly larger imaging depth has been demonstrated for 3PM which corresponds to imaging down to the bottom of the mouse cortex and into the hypocampus [37] [38] [39] or through its skull [40] and down to about 1mm in the macaque cortex [31]. 3PM is also more resilient to scattering [41] making it less sensitive to the presence of the dura or the growth of a neomembrane.

2.2 WORKING PRINCIPAL AND TECHNICAL DESCRIPTION OF MULTI-PHOTON MICROSCOPY

This section introduces the main concepts of multi-photon microscopy as well as the main pieces of equipment and parameters of such a setup and their dependency.

2.2.1 Fluorescence microscopy

Fluorescence corresponds to the absorption and re-emission of light by a molecule. Electrons of a molecule have several discrete energy levels that are given by a Perrin-Jablonski diagram (Figure 2.1). The ground state is the lowest energy level and an electron can get to a higher energy level by absorbing photons. It will relax by emitting a single photon which wavelength (λ) is given by $E = hc/\lambda$ with h the Plank constant and c the speed of light.
MPM is based on the excitation of a molecule by the simultaneous absorption of multiple photons. The molecule will then get back to its ground state by emitting a single photon at a lower wavelength [42] (Figure 2.1). The number of photons that are absorbed simultaneously is referred to as the **non-linearity order** of the process.

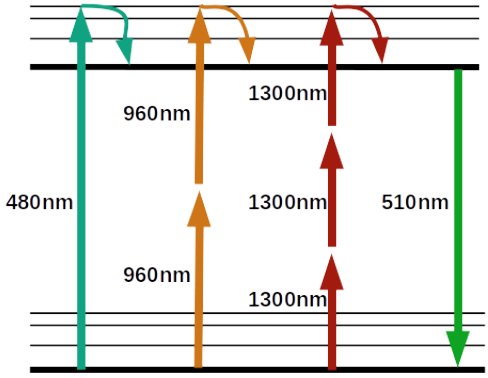

Figure 2.1 – Simplified Perrin-Jablonski fluorescence diagram for single-photon (blue), two-photon (orange) and three-photon (red) excitation. The wavelength of the absorbed photons varies with the order of excitation but a photon with the same wavelength is emitted (green) during the fluorescence.

The main advantage of MPM is that it provides **optical sectioning**. In microscopy, optical sectioning is the ability to image a thin layer of a sample by selectively collecting the photons coming from the focal plane. In confocal or single-photon microscopy, it is ensured by a **pinhole** : out-of-focus light will be blocked by the pinhole while photons coming from the focal plane will go through. Pinholes are efficient but this only takes into account ballistic photons that have traveled through

the sample without being scattered. Scattered photons coming from the focal plane will also be blocked by the pinhole which reduces the collection efficiency of these techniques and therefore limits their maximal depth of imaging (Figure 2.2).
On the contrary, optical sectioning is inherent for MPM. Multi-photon absorption is a probabilistic event that requires a high density of photons so the excitation of molecules can only occur in a small region of the sample in the vicinity of the focal point of the objective. This region can be characterized by the **point spread function** (PSF) of the laser beam. For 2PM, the fluorescence signal is proportional to $1/z^2$ and for 3PM it is proportional to $1/z^4$ with z the distance to the focal point [37]. Moreover, the wavelength of the photons emitted by the sample is different from the one of the photons used to excite it. Therefore, they can easily be discriminated by the use of a filter in the collection path of the microscope. A pinhole is no longer necessary and this leads to a major distinction between confocal and MPM : in MPM, all the photons coming out of the sample towards the objective are collected. This includes ballistic photons as well as scattered photons so the collection efficiency of 3PM is improved compared to confocal microscopy [42] (Figure 2.2).

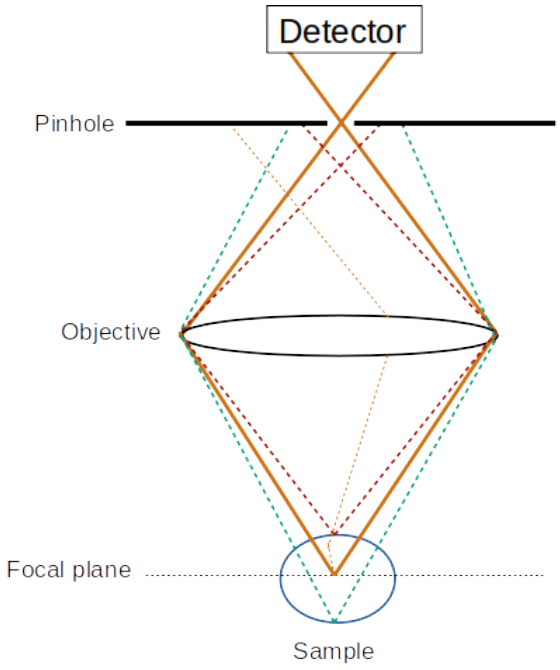

Figure 2.2 – Working principal of a pinhole : ballistic photons coming from the focal plane (orange path) go though the pinhole while out-of focus and scattered photons are stopped (dashed paths).

Thanks to the inherent optical sectioning of MPM, it is possible to image through a thick scattering tissue while keeping the advantages of an optical microscopy technique : visualizing live structures in real time. Combined with the use of a

wavelength chosen to minimize the absorption of photons by the sample [43], MPM is well suited to study living organisms such as mice[6] or even non-human primates[34][44][16][45].

Yet, for fluorescence to occur, the sample must produce **fluorophores** : fluorescent molecules that have the ability to absorb and re-emit photons. The first possibility is to perform a **transduction** : viral vectors (usually AAV) are locally injected in the cortex to infect the neurons. The genome of the infected neurons will be modified to produce the desired fluorescent proteins. This method can be used on any species and has a local action so it is possible to select the regions to infect and modulate the parameters of the injections to control for the sparsity of the labelling and size of the infected region for example [46][34].
For some species, **genetically modified lines** have been established where neurons already produce fluorescent probes. These lines present the advantages of a stable and reproducible production of fluorophores over time and individuals and to have the complete population of neurons infected [47][48]. A variety of such genetic lines have been designed for different applications. Yet, this solution is largely restricted to mice at the moment.
Finally, **systemic injections** are under development and have already been tested in mice [49]. This represents an alternative to genetically modified lines with similar advantages and could be applicable for other species like macaque monkeys.

2.2.2 Wavelength and effective attenuation length

The microscope is made of an excitation path and a collection path. The laser beam of photons is scanned over the sample to excite the fluorophores and the photons emitted by the later are then collected. The excitation photons that travel through the sample to reach the fluorophores and the re-emitted photons that travel back to the collection path are subjected to **absorption** by the tissue and **scattering** : deviation of the path due to the inhomogeneity of the sample. Both phenomena decrease the excitation and collection efficiency and their attenuation factor vary with the wavelength of the photons.

The **effective attenuation length** (EAL), noted l_e, is used to quantify the attenuation of a sample due to absorption and scattering for a given wavelength and can be decomposed as follow :

$$l_e = l_a + l_s \ or \ \frac{1}{\mu_e} = \frac{1}{\mu_a} + \frac{1}{\mu_s}$$

with l_a and l_s the absorption and scattering length constants and μ_e, μ_a and μ_s the attenuation, absorption and scattering coefficients respectively. These coefficients correspond to the number of photons lost due to absorption or scattering per unit distance.

The intensity of a laser beam (I) travelling through a sample of thickness z can be expressed as :

$$I(z) = I_0.exp(-\frac{z}{l_e}) \tag{2.1}$$

with I_0 the intensity of the laser beam at the surface of the sample. Therefore, the EAL corresponds to the depth that can be travelled by the photons before the intensity decreases by a factor of 1/e.
For tissue, these coefficients vary with the wavelength : the attenuation length of absorption decreases with the wavelength while attenuation length of scattering increases (Figure 2.3). While taking both phenomena into account, increasing the wavelength between 400nm and 1400nm leads to an increase in attenuation length and there exists some **optimal wavelengths around 1300nm and 1700nm**.

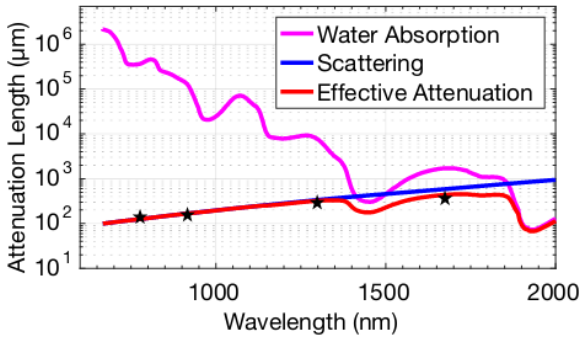

Figure 2.3 – Graph of the attenuation length of absorption (pink), scattering (blue) and the effective attenuation length of tissue (red) according to the wavelength. The black stars correspond to wavelength used in the literature for multi-photon microscopy. Figure taken from [43]

Another parameter to consider for the choice of the wavelength is the fluorophore's absorption spectrum. Indeed, each fluorophore can absorb photons within a specific range of wavelengths. For example, the excitation spectrum of GCaMP6f and fluorescein dextran are centered around 495nm (Figure 2.4) [50] [51]. This wavelength corresponds to the optimal wavelength to use with single-photon microscopy to excite these molecules. For 2PM and 3PM, the optimal wavelength is about twice and three times higher respectively.

In conclusion, a higher wavelength leads to a higher attenuation length in tissue. Therefore, for the same fluorophore, scattering and absorption will be less significant for higher orders of excitation process i.e. for 3PM than 2PM. Likewise, red fluorophores rather than green ones can be used to increase further the excitation wavelength [43].

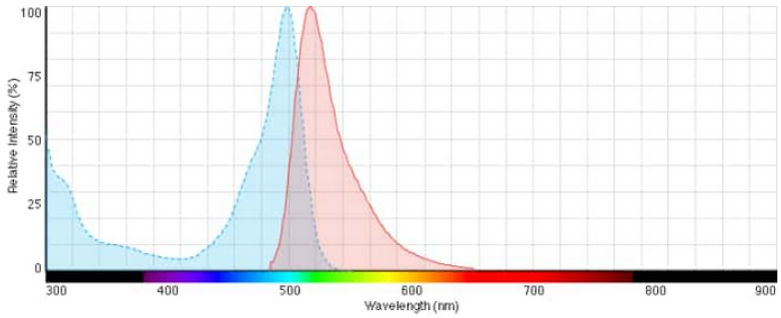

Figure 2.4 – Absorption (blue) and emission (red) spectra of fluorescein dextran. Spectrum taken from [51].

In a MPM setup, the wavelength is first defined by the laser source and may be adjusted by the use of an **optical parametric amplifier** (OPA).

2.2.3 Pulse width and repetition rate

MPM is based on the excitation of fluorophores by the simultaneous absorption of several photons. For the excitation to occur, several photons need to be in the vicinity of the fluorophore nearly simultaneously. Excitation efficiency can be optimized by the choice of the laser source and the use of a dispersion compensation unit.

A **pulsed laser** is used in MPM to boost the excitation efficiency. Unlike continuous lasers, pulsed ones send bursts of photons within small and periodic intervals of time. The **repetition rate** of the laser characterizes the frequency of the pulses and the **pulse width** corresponds to the pulse duration. The mean intensity of the laser beam (I) and the mean fluorescence generated by the sample (F) are given by :

$$< I >= R.\tau.I_p \; and \; < F >= R.\tau.F_p.$$

with τ the pulse width, R the repetition rate of the laser, I_p the peak intensity of one pulse and F_p the fluorescence generated during one pulse (Figure 2.5).

The fluorescence generated by a single pulse is given by :

$$F_p = \frac{1}{N}.\sigma.I_p^N \tag{2.2}$$

with σ the absorption cross-section that relates the probability for a fluorophore to absorb two or three photons simultaneously and N the non-linearity order of the excitation process.

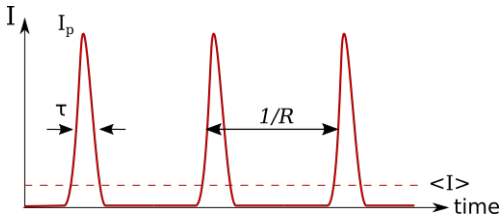

Figure 2.5 – Schematic of the intensity over time of a **pulsed laser** with I_p the peak intensity, τ the pulse width, *R* the repetition rate of the laser and <I> the average intensity of the laser beam.

Therefore, the mean fluorescence is given by :

$$< F >= R.\tau.\frac{1}{N}.\sigma.(\frac{1}{R.\tau}. < I >)^N$$

$$< F >= \frac{1}{N}.\sigma.(\frac{1}{R.\tau})^{N-1}. < I >^N . \quad (2.3)$$

As a comparison, for a continuous laser, $< I >= I_p$ and $R.\tau = 1$ so

$$< F >= \frac{1}{N}.\sigma. < I >^N .$$

In conclusion, using a pulsed laser leads to **a gain in fluorescence of $\frac{1}{R.\tau}$ in 2PM and $(\frac{1}{R.\tau})^2$ in 3PM** so the lower the repetition rate and pulse width, the higher the excitation efficiency. For a three-photon microscope with a repetition rate of 800kHz and a pulse width of 55fs, the gain is 2.10^7 [38].
A nominal value of the repetition rate is 80MHz for 2PM [52] and so far up to 1MHz has been used in 3PM setups [37] [53] to increase the excitation efficiency at the expense of the field of view and imaging speed. The repetition rate is set by the laser source and leads to a tread-off between imaging speed and signal intensity.
Besides, the absorption cross-section (σ) is of the order of 10^{-49}cm^4.s.photon^{-1} for 2PM and 10^{-83}cm^6.s^2.photon^{-2} for 3PM [54] [55] which relates the lower probability for three-photon fluorescence to occur with respect to two-photon fluorescence. Using the absorption cross-section, it is possible to calculate the pulse energy required to reach a given level of excitation probability. For fluorescein dextran, 3PM requires a pulse energy 15 times higher than 2PM to generate the same signal at the surface of the cortex. The pulse energy has to be 8 times larger for GCaMP6s-labeled neurons [41]. This ratio decreases for larger imaging depths thanks to the difference in effective attenuation lengths but there is a greater risk of tissue heating and damage when using 3PM rather than 2PM.

Pulsed lasers that generate a beam with a **pulse width** in the sub-picosecond range are suitable for 3PM and are currently commercially available. However, the pulse width expands between the laser source and the objective of the microscope as photons travel through the optics of the path.

Because of Heisenberg's uncertainty principle, the temporal dispersion of a pulse is inversely proportional to its spectral dispersion. This means that a pulsed laser cannot be monochromatic and that the shorter the pulse width, the larger the spectral bandwidth of the beam. This is important to take into account to design a MPM setup because it is the spectral dispersion that will cause an increase of the temporal dispersion. The refractive index of a material (n), glass for example, is modulated by the wavelength of the light going through it : the index is larger for shorter wavelengths. Since the speed of light in a medium is given by $v = \frac{c}{n}$ with c the speed of light in vacuum, shorter wavelength rays will travel slower through glass lenses than rays with a larger wavelength (Figure 2.6).
As a result, the pulse width will increase whenever the beam goes through a lens and in particular in the objective of the microscope that is made of several lenses. To compensate for this dispersion, a **dispersion compensation unit** can be added to the microscope.

Figure 2.6 – Illustration of the positive dispersion induced on a polychromatic beam of light going through an optical material. The refraction index and therefore the speed of light through a medium varies with the wavelength of the light going through it. Illustration taken from [56].

Prisms can be used to induce a negative chirp to the beam and compensate the dispersion.
A first prism is used to split a polychromatic laser beam by creating an angular dispersion based on the wavelength. This happens because the refraction index of the prism varies with the wavelength. A second prism is placed in the path so that optical rays come out parallel to each other and a mirror is positioned so that the beam travels back through the two prisms to reverse the angular dispersion.
Thanks to the angular dispersion created by the first prism, the path length inside the second prism varies with the wavelength. The difference in path lengths determines the amount of negative dispersion of the unit and can be tuned by changing the distance between the two prisms (Figure 2.7) [57]. Similarly, a pair of gratings or a silicon wafer [58] can be used to create an angular dispersion relative to the wavelength and create a negative chirp.

Thanks to these compression methods, it is possible to get a pulse width as

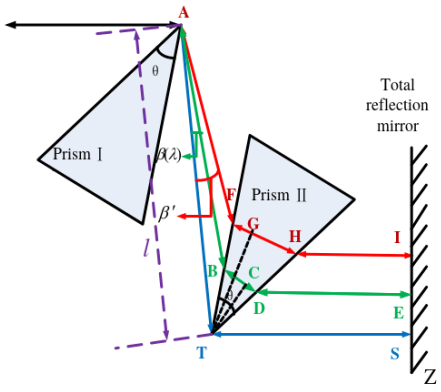

Figure 2.7 – Illustration of the negative dispersion gained by the addition of two prisms and a mirror to the optical path. The first prism separates the different components of the laser beam that will have different path lengths inside the second prism. The variation in path lengths creates a negative dispersion and the amount of dispersion can be adjusted by modulating the distance between the two prisms. The mirror is used to negate the angular dispersion caused by the first prism. Figure taken from [57].

low as 40fs [53] [40] at the objective. The nominal value for 3PM is in the range of 50 to 70fs for 3PM setups [59] [38].

2.2.4 Power management

The fluorescence generated by 3PM is proportional to the cube of the intensity of the excitation beam at the focus (Equation 2.3). However, because of absorption and scattering, the deeper the imaging, the more power at the surface of the sample is required to generate the same fluorescence level. Thus, for deep 3PM, the available power at the focus of the objective needs to be optimized. This can be done with the choice of the laser source and optics in the path.

The imaging power is characterized by two metrics : **the average power** and **the pulse energy**. The former is the mean power of the laser beam over time. The average power at the surface of a sample can easily be measured by placing a power meter under the objective of the microscope. The average power at an imaging depth z inside a sample needs to be calculated according to the average power at the surface and the attenuation length using Equation 2.3. As for the pulse energy, it corresponds to the power of a single pulse. It can be calculated by dividing the average power by the repetition rate of the laser. As the imaging depth increases, the average power has to be increased to compensate for absorption and scattering to maintain a constant pulse energy at the focus and fluorescence generation. Since the attenuation length is larger for 3PM than 2PM, the decrease in power at the focus with depth is faster for 2PM.

Yet, if either the average power at the focus or the pulse energy becomes too high, the evoked response of neurons may be altered or the tissue may be irreversibly damaged. The main source of tissue damage in MPM comes from phtochemical damage : molecules can be ionized following the absorption of photons and the released electrons can lead to a local formation of plasma that create photochemical damage and can cause tissue ablation if a power threshold is crossed [60].

In terms of pulse energy, there are three thresholds to consider :

— The first one is 2nJ at the focus. For this pulse energy, there is no visible alteration of cells but the functional response may be modified [53].

— Starting at 5nJ, there can be photo-bleaching : a chemical reaction can happen that prevents the fluorophores to get back to their ground state after the absorption of photons. This results in an increase of the baseline fluorescence intensity and can lead to a decrease in the signal-to-background ratio (SBR) preventing long recordings. However, this phenomenon is reversible in live tissue as new fluorophores will be generated by the cells.

— The last threshold is 10 to 15nJ : if the pulse energy reaches this threshold, the tissue may be irreversibly damaged or ablated.

As for the average power, it will cause an elevation of the tissue temperature which in turn can alter the cells responses [53] [41]. Another issue when the average power at the surface increases is the background fluorescence : the out-of-focus power may become sufficient to elicit fluorescence excitation which translates into an elevation of the background signal and a reduced SBR. However, this is much less problematic for 3PM than 2PM as three-photon excitation requires more power.

2.2.5 Scanning mechanism and parameters

During the excitation process, the laser beam is scanned over the sample thanks to scanning mirrors. The scanning technology together with the laser properties will set the scanning parameters such as the field of view and frame rate.

Scanning the sample is usually performed using a raster pattern : successive imaging of the lines of a frame, from top to bottom. This can be achieved using galvanometric mirrors or resonant mirrors. The position of a **galvanometric mirror** is set by a voltage and the voltage pattern determines the position of the mirror over time. With galvanometric mirrors, the dimensions of the image and the scanning pattern are variable so it can be possible to scan regions of interest only. **Resonant mirrors** are also controlled with a voltage but they oscillate at a constant speed and the voltage determines the amplitude of the oscillations.Their movements are faster than galvanometric mirrors. For example, using the mirrors from Scientifica, a pair of galvanometric mirrors give a frame rate of 4 frames per

second with frames of 512 by 512 pixels against 30 frames per second for a pair of resonant mirrors [61]. On the one hand, galvo-galvo scanners have a maximum scan frequency of 1kHz which corresponds to a line scan rate of 2kHz. On the other hand, galvo-resonant scanners typically have a scan frequency of 4, 8 or 12kHz (Thorlabs, Novanta photonics).
However, since the scanning pattern is the result of oscillations for a resonant scanner, the scanning speed is not constant and without correction the image would appear stretched. Thus, an inverse sine spatial look-up table is used to account for the varying speed [62]. As a result, the number of pixels per line is reduced to about 70% with respect to a galvanometric scanner. So far, only galvo-galvo scanners have been used in 3PM setups [31][39][41][53] with the exception of one setup [63]. In this setup, an adaptive excitation source is used to generate pulse trains that are synchronized to the scanning pattern in order restrict the illuminated area to selected regions of interest (surrounding neurons). In doing so, only a small portion of the field of view is illuminated which reduces the overall average power. Thus, a higher repetition rate and scanning speed can be used without risking to damage the sample. They are using a galvo-resonant scanner with a 32MHz laser and achieve a frame rate of 30Hz with a field of view of 512x512 pixels. However, imaging small regions of interest is not compatible with large motion artefacts.

Scanning can also be performed using **acousto-optics** : a pattern of acoustic waves is sent through a crystal and locally changes its refractive index periodically. The periodic variation of the refractive index acts as a diffraction grating that deflects the beam. By changing the acoustic wave pattern, the diffraction angle can be modulated and the laser beam can scan the sample. Acousto-optics can be used to selectively scan regions of interest and therefore increase the frame rate [64].

The time spent by the laser on one pixel is called the **dwell time**. It needs to be high enough for the fluorophores to be excited but a longer dwell time means a higher noise level [10].

Together, the dwell time and the chosen scanning mechanism, either mechanical or acousto-optical, limit the imaging speed and causes a tread-off between the **field of view** and the **frame rate**. The required frame rate depends on the application, for calcium imaging using the GCaMP6s calcium indicator, 14Hz is enough to record single spikes[41][46].

2.2.6 Collection path

The collection path of a MPM is constituted of an objective, a filter and a collector.

The choice of the **objective** is important to optimize the **resolution** as well as the light collection efficiency.
The resolution is given by the smallest distance between two object needed to distinguish them either laterally or axially. It is referred to as spatial resolution or resolving power for the former and depth of focus for the latter. The spacial resolution ($d_{x,y}$) is inversely proportional to the numerical aperture of the objective (NA) and the depth of focus (d_z) is inversely proportional to the square of the numerical aperture [65] :

$$d_{x,y} = \frac{1}{\sqrt{N}}.\frac{0.61.\lambda}{NA} \; and \; d_z = \frac{1}{\sqrt{N}}.\frac{2n}{(NA)^2}$$

with λ the wavelength of the excitation beam, *N* the non-linearity order of the excitation process and *n* the refractive index of the immersion medium.
The **numerical aperture** of an objective corresponds to the half-angle of the incident rays on the objective and characterizes the cone of light that can be emitted and collected by the objective (Figure 2.8). Thus, the numerical aperture should be high for MPM to boost the resolution as well as optimize the collection of the scattered light.
The resolution also determines the extent of the region of the sample where the laser beam is focused. Yet, as mentioned in Section 2.2.1, the fluorescence generation is proportional to $1/z^2$ for 2PM and $1/z^4$ for 3PM with z the distance to the center of the PSF. Therefore, the resolution of the optical setup and in particular the numerical aperture of the objective are essential to a multi-photon microscopy setup.

A **filter** is placed between the objective and the collector to reflect the photons coming from the excitation beam and transmit the photons generated by fluorescence. It is possible to use several fluorescent probes with different emission spectra and to have different filters and collectors to image them simultaneously [67].

The **collector** is a photomultiplier tube (PMT) : it is a very sensitive photon detector able to detect a single photon. Each photon will generate a group of electrons inside a PMT. A PMT has a **linearity range** where the current generated while one pixel is scanned is proportional to the received fluorescence intensity.

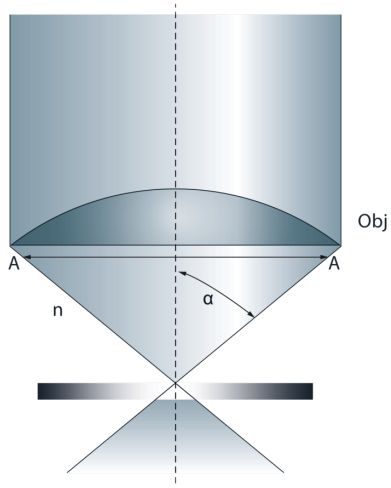

Figure 2.8 – Illustration of the numerical aperture (NA) of a objective : NA=n.sin(α) with n the refractive index of the immersion medium and α is half of the angle of the cone of light that can be emitted or collected by the objective. Figure taken from [66]

3 - DESIGNING A MULTI-PHOTON MICROSCOPY SETUP FOR DEEP IMAGING

In order to test and quantify the added value of a three-photon microscope, an optical path for two-photon microscopy (2PM) has been set up in parallel to be able to switch from 2PM to 3PM while keeping the same point of focus.
In this chapter the setup is described and the choices made during its development are detailed. Imaging in mice is used to test the setup, results of which are described as well.

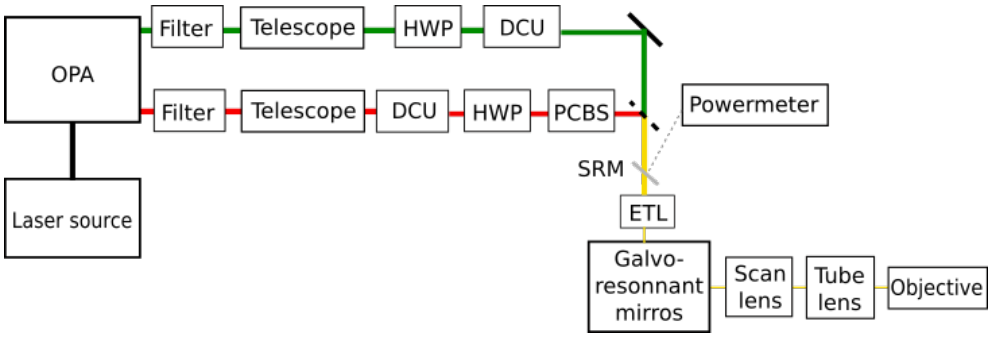

Figure 3.1 – Diagram of the microscopy setup with the three-photon path in green and the two-photon path in red. A laser source generates a beam at 1035nm. An optical parametric amplifier (OPA) is used to adjust the wavelength to either 1300nm (green path) or 960nm (red path), filters are used to narrow the beam spectrum and a telescope controls the beam diameter and vergence. A two-prism dispersion compensation unit (DCU) is used to compensate for the time dispersion of the beam. A half-wave plate (HWP) and a cube beam splitter (CBS) are used to modulate the power. In the 3PM path, the prisms of the compressor are used in place of the CBS. A semi-reflective mirror (SRM) is placed in the path to reflect about 3% of the power towards a power meter to have a readout of the power during imaging. An electrically tunable lens (ETL) can be used for multi-plane imaging. Finally, a galvanometric and a resonant mirror are used for scaning and are followed by a scan lens, a tube lens and the objective.

3.1 Introduction to the setup

The microscope is set up in a room that has been designed specifically for it. In particular, there is a ventilation system to ensure a stable temperature of 22°C $\pm$ 1°C and room humidity of 50% $\pm$ 5%. This is important as variations in temperature and humidity cause alignment variations in the optical paths and variations of power.

The setup is on an optical table (Newport RS 2000, 1.5m x 3m) resting on four air-pressured legs (Newport, Stabilizer S-2000) to compensate for any vibration of the floor. The table has a hole cut into it where the NHP transportation chair (Christ Instrument) can fit in. The chair is lifted off the ground and resting on the table when a NHP is positioned under the objective. This way, the head of the animal and the microscope are moving together.

In addition to the multi-photon microscopy paths that are detailed in this chapter, there is the possibility to perform widefield imaging. A LED (MCWHLP1, Thorlabs) together with a 469nm excitation filter provide the excitation beam that is reflected by a 498nm longpass dichroic mirror (DFM1, Thorlabs) positioned prior the objective. The emission beam is then transmitted by the dichroic mirror towards the 525nm emission filter and the CCD camera (Prosilica GT2750, Allied Vision) that is used for the collection.

3.2 Choice and description of the laser and optical parametric amplifier

3.2.1 Laser source and repetition rate

The laser source is the Monaco 1035-40-40 from Coherent. It has a master oscillator parametric amplifier (MOPA) architecture that enables a large average power of 40W with a repetition rate that can be set from 200kHz up to 50MHz while preserving the beam optical properties.
With the aim of three-photon microscopy, the main parameters of the laser are the average power that should be high enough for 3PM and the repetition rate that should be low compared to the standard of 2PM which is 80MHz [52]. As mentioned in Chapter 2, the choice of the repetition rate leads to a tread-off between the pulse energy and the field of view or frame rate.
Our goal is to do calcium imaging in awake and behaving NHPs so we aim at maintaining a frame rate high enough to allow offline motion correction (more than about 15Hz) as well as capturing the calcium transient, and a relatively large field of view with good spatial resolution (around 2μm) to visualize a population of neurons while imaging deep enough to be able to record neurons either through the natural dura or the neomembrane that grows when the dura is removed.

In order to choose a laser adapted to 3PM of the NHP cortex, one can estimate the maximal imaging depth according to the repetition rate of the laser. This can be achieved using the following equations (Equation 2.1) :

$$I = E_p.R \; and \; I(z) = I_0.exp(-\frac{z}{l_e})$$

with I the average intensity of the laser, E_p its pulse energy, R its repetition rate, z the depth of focus, I_0 the average laser intensity at the surface of the sample and l_e its effective attenuation length (EAL).
In addition, some values for the parameters are needed :

- the minimum pulse energy required to receive 0.1 photons per laser pulse, which is a typical signal strength for imaging the activity of neurons (E_{plim}). This is reported to be 0.24 $\pm$ 0.05 nJ for 2PM and 1.86 $\pm$ 0.27 nJ for 3PM with a pulse width of 60fs [41]. A similar value of 1.5nJ is reported at 1300nm with a pulse width of 55fs [38] and about 1nJ with 40fs [53].
- the maximum average power that can be used at the surface of the mouse cortex without causing damage (I_{0max}), which is 250mW for 2PM [68] and 100mW for 3PM [41].
- the EAL of the cortex is 154μm for 2PM and 293μm for 3PM [41].

The parameters are given for the mouse cortex rather than the NHP because no value was found in the literature for the latter. The attenuation length of the NHP is expected to be similar to that of mice and *in vivo* measurements are done in

Chapter 5 to test that and update the model. As for the maximum power that can be used safely, it would rather be larger for NHPs as the imaging chamber is larger which helps for heat dissipation so the calculated maximum imaging depth is rather underestimated.
Finally, we have :

$$z_{max} = ln(\frac{I_{0max}}{I_{lim}}).l_e = ln(\frac{I_{0max}}{E_{plim}.R}).l_e \tag{3.1}$$

with I_{lim} the laser intensity required to image neurons.

These equations can be used to estimate the maximum imaging depth inside the cortex of NHPs where a satisfying signal can be elicited without causing damage to the tissue. However, this does not take into account the quality of the imaging that can be characterized by the SBR. This is particularly an issue when recording at a large depth using 2PM.
In addition, the presence of tissue at the surface of the cortex, either granulation tissue or dura mater, is not considered here. Such tissue is expected to have a lower EAL than the cortex so the maximum imaging depth would be decreased. This will be discussed and investigated in the Chapters 4 and 5.

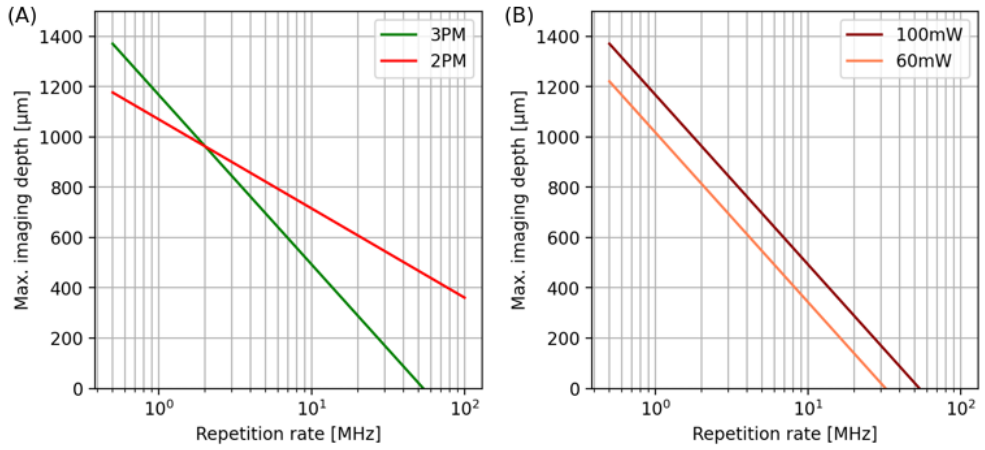

Figure 3.2 – **(A)** Maximum imaging depth that can be reached while keeping the power low enough not to damage the cortex according to the repetition rate of the laser for 2PM and 3PM. **(B)** Maximum imaging depth that can be reached using 3PM according to the repetition rate of the laser and the maximum average power available at the surface of the sample.

The goal with this microscope is to image 400μm deep inside the cortex of NHPs in the presence of the dura mater. Its natural thickness averages 467μm but we are expecting it to become thinner after the implantation of an imaging chamber that applies pressure at its surface (see Chapter 5) [69]. Therefore, a

repetition rate of 4MHz is chosen to ensure that we can image 400μm of cortex despite the presence of dura (Figure 3.2.A).

Initially, we had set the repetition rate to 4MHz to favor the field of view and imaging speed at the expense of imaging depth but we found the pulse energy after the objective not to be sufficient for NHP imaging. The maximum pulse energy that we could reach was about 60nJ and the maximal depth we commonly reached in mice was between 500 and 600μm. This is in accordance with Figure 3.2.B that shows the maximum imaging depth according to the repetition rate of the laser and the maximum average power available at the surface of the sample.

Thus, we have decided to lower the repetition rate down to 2MHz. By doing so, the pulse energy is doubled for the same average power.
We can estimate the gain in maximal imaging depth using Equation 3.1. The maximal depth of imaging with a repetition rate of 4MHz z_{max}^{4MHz} is given by :

$$z_{max}^{4MHz} = ln(\frac{I_{0max}}{I_{lim}}).l_e.$$

By changing the repetition rate, the pulse energy has doubled so the minimum power required to excite the fluorophores as been divided by two (to keep the pulse energy constant).
In addition, the average power at the input of the microscope increased by 150% during the process.
After the modification, the maximum imaging depth thus became :

$$z_{max}^{2MHz} = ln(\frac{I_{0max} * 1.5}{I_{lim}/2}).l_e = ln(\frac{I_{0max}}{I_{lim}}).l_e + ln(3).l_e$$

$$z_{max}^{2MHz} \approx z_{max}^{4MHz} + 1.1\ l_e$$

In the end, thanks to the change in repetition rate as well as the gain in power, we have increased our maximal imaging depth by over one EAL which is about 300μm for the mouse cortex using 3PM [41].
After the change in repetition rate, the maximum pulse energy at the surface of the sample became 90nJ and we were able to image the mouse cortex up to 1100μm (Figure 3.3).

3.2.2 Adjusting the wavelength

The laser beam is at 1035nm at the output of the laser source and an optical parametric amplifier (OPA) (Opera-F, Coherent) is used to modulate its wavelength. The OPA uses a pump laser to generate two complementary laser beams called signal and idler so that $\frac{1}{\lambda_p} = \frac{1}{\lambda_s} + \frac{1}{\lambda_i}$ with λ_p half of the wavelength of the pump laser, λ_s and λ_i the wavelengths of the signal and idler beams. With

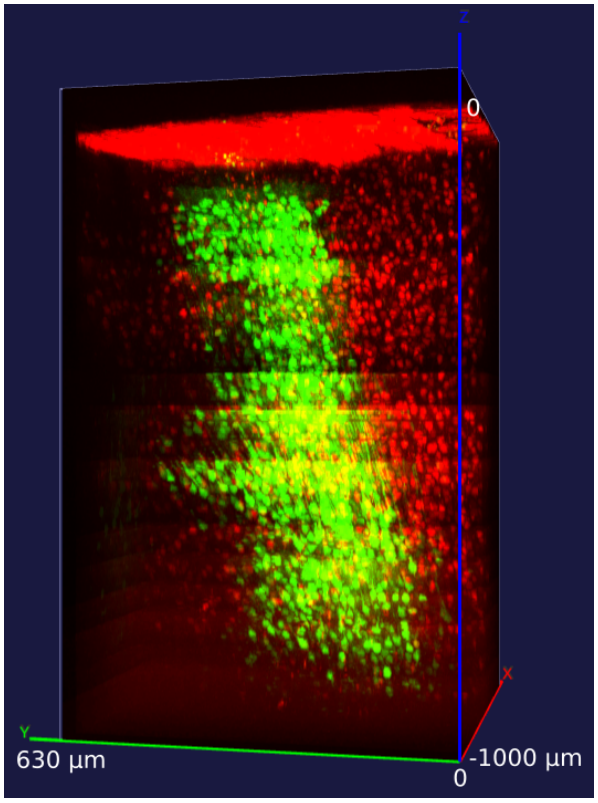

Figure 3.3 – 3D rendering of a z-stack of a GCaMP6s injection site in the anterior cingulate cortex of a GAD2-Cre-Rosa-TdTomato mouse. All the neurons can be recorded using the red channel and the neurons infected by the GCaMP virus can also be recorded in the greed channel.

an input laser beam at 1035nm, λ_p=517.5nm and the output wavelength ranges from 640nm to 940nm for the signal and from 1154nm to 2717nm for the idler. To generate an idler beam at 1300nm, the wavelength used for 3PM, the corresponding signal beam must be at 860nm. The average power at the output of the OPA ranges between 1.4W and 1.7W (Figure 3.4).

The beam at the output of the OPA also contains contamination from other wavelengths (mainly 517 and 860nm that correspond to the wavelengths of the pump and signal) and we can see several colors on laser cards when we are aligning which makes it more complicated. We therefore added a 1200nm high-pass filter after the OPA.

3.2.3 Perspectives

Since we have built our setup, the market for three-photon microscopy has expanded and new laser sources have been designed with that application in mind. The next generation of the Monaco laser from Coherent has 60W of output average

power (instead of 40W). And recently, Coherent, Class 5 and Spark have launched new and promising laser sources specific for 3PM that combine a laser and an OPA to deliver a 1300nm laser beam with a tunable repetition rate. These lasers are making it simpler and more accessible for new setups dedicated to 3PM to emerge.

3.3 Addition of a dispersion compensation unit

3.3.1 Temporal dispersion in the setup and compensation

The signal generation is proportional to $\frac{<I>^2}{\tau}$ for 2PM and $\frac{<I>^3}{\tau^2}$ for 3PM (Equation 2.3). Therefore, a small pulse width is essential to have a good excitation efficiency while using less power, especially to avoid damaging the cells or the tissue during deep imaging.

As the beam goes through optical lenses, its pulse width increases. At the focus of the objective, it is 160fs at 1300nm. We therefore added a dispersion compensation unit (femtoControl, A.P.E.) in the optical path that was optimized for wavelengths between 1150nm and 2500 nm. It is composed of two SF10 prisms with an adjustable distance between them. This distance is used to tune the pulse width of the laser beam after the objective and is chosen so as to minimize it. It is possible to measure the pulse width of a laser beam using an autocorrelator. On a daily basis, the position of the prisms is finely tuned using the fluorescence signal as a reference.
At the focus of the objective, **the pulse width is 60fs at 1300nm** using the sech^2 module of an autocorrelator (Carpe, A.P.E.) (Figure 3.4).

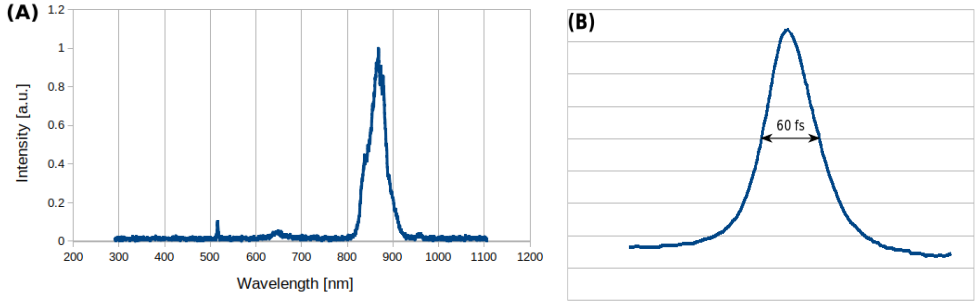

Figure 3.4 – (A) : Spectra of the signal beam at the output of the OPA for 3PM with a peak intensity at 860nm. (B) : Graph of the pulse width after the objective as measured with the autocorrelator, using the sech^2 setting for 1300nm.

The downside of the dispersion compensation unit is that it has a low transmission of power of 70 to 75% and the limiting factor for deep imaging using 3PM is power. However, this is made up for by the fact that less average power is required for smaller pulse-width pulses.

3.3.2 Quantification of the impact of the dispersion compensation unit

To quantify the impact of the dispersion compensation unit, we have added flip-mirrors in the 3PM optical path to have a path without compression and be able to easily image the same sample with the two configurations.
The pulse width at the objective is 160fs without pulse compression. As previously mentioned, fluorescence is proportional to $\frac{<I>^3}{\tau^2}$ (Equation 2.3). To get the same signal we have :

$$\frac{I^3}{\tau^2} = \frac{I'^3}{\tau'^2} \; so \; I = \sqrt[3]{(\frac{\tau}{\tau'})^2}.I'$$

with I' and τ' the intensity and pulse width without the compression.

With a pulse width of 60fs compared to a pulse width of 160fs, the power has to be : $I = \sqrt[3]{(\frac{60}{160})^2}.I' \approx 0.52.I'$, so about 50% less which offsets the power lost by transmission through the dispersion compensation unit.

3.4 Optics in the path

3.4.1 The arm of the microscope

The 3PM optical path, between the output of the OPA and the objective is about 4.5m long and contains 12 mirrors. This large number of mirrors is explained for the large part by the architecture of the arm of the microscope that contains 6 mirrors. Its architecture has been designed to be flexible and adaptable to the sample rather than the opposite. In particular, it is made of three translation stages to displace the objective in the three orthogonal directions of the space and the objective has a rotation span of about 180°. This is very useful for awake NHP recordings to be able to position the objective over the chamber and to adjust its angle to have it orthogonal to the surface of the chamber while the NHP keeps its head straight (Figure 3.5).

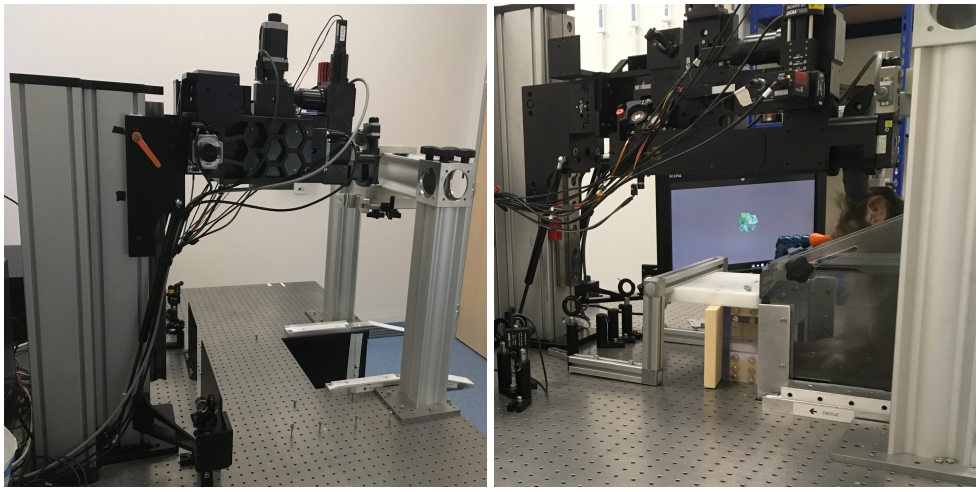

Figure 3.5 – Picture of the arm of the microscope that contains three axes of translation and one axis of rotation for the objective. A button-press and reward system can be added for cognitive tasks.

3.4.2 Mirrors and telescopes

Each **mirror** causes power loss so it is essential to select them carefully. We are using protected silver mirrors from Thorlabs (PF10-03-P01) with a specific coating for near-infrared wavelengths. The theoretical reflection of the mirrors is 97.9% at 1300nm and 96.9% at 960nm for an incidence angle of 45°[70]. The mirrors of the path have been tested at 1300nm and the reflection was measured between 97.1 and 98.4%, well in accordance with the literature.

The ETL can be a source of power loss so a customized lens with a coating specific to 1300nm was ordered from Optotune.

We are using **telescopes** in the optical paths to control both the vergence and the diameter of the beam. If the beam is convergent, there is a risk of damaging the optics at the focal point so a first telescope is used to have the beam collimated or slightly divergent. Projecting the beam on the wall, at a distance approximating the path length makes it easier to control the vergence and the absence of focal point in the path. To control for the beam diameter at the back aperture of the objective and therefore its filling, a second objective can be used.
There is one telescope inside the OPA but we have asked the company to remove it because we could not tune it, the beam at the output of the OPA was converging and the beam diameter was too large for the half-wave plate lens that is positioned before the dispersion compensation unit. The removal of the lenses of the telescope of the OPA led to an increase of 9% in power.
We had two telescopes as described earlier but the second one was deteriorating the beam profile and since a telescope is a source of time dispersion as well as loss in power, the second one was removed of the path and the lenses of the first telescope have been changed to increase its magnification.
The distance between the two lenses of the microscope controls the vergence of the beam and therefore the filling factor of the back aperture of the microscope. There is tread-off between the homogeneity of the illumination of the field of view and the maximum power that can be reached at the sample. Indeed, the intensity profile of the laser beam has a gaussian profile so underfilling the back aperture leads to a gaussian intensity profile of the field of view and it gets more significant for deep imaging. However, overfilling it to have a more linear profile means cutting off some of the power. Therefore, a tread-off has to be found to ensure that the whole field of view can be used the recordings while maximizing the power. To find the optimal parameter, a fluorescent plate is used to easily visualize the intensity profile (Figure 3.6). In our setup, we are currently slightly overfilling by 5.7%.

3.4.3 Power control and readout

Tuning the power and reading it out remotely is very useful to perform imaging. Adjusting the power is done using a half-wave plate (HWP) followed by a polarizing cube beamsplitter (CBS). A HWP polarizes a laser beam in a direction that depends on the HWP's angular position. The polarizing CBS separates an incident beam into two beams of orthogonal polarization that are transmitted in two orthogonal directions. Therefore, by rotating the HWP, the power of the beam transmitted straight through the CBS varies.
In the setup, the HWP (AHWP05M-1600, Thorlabs) is specifically coated to have

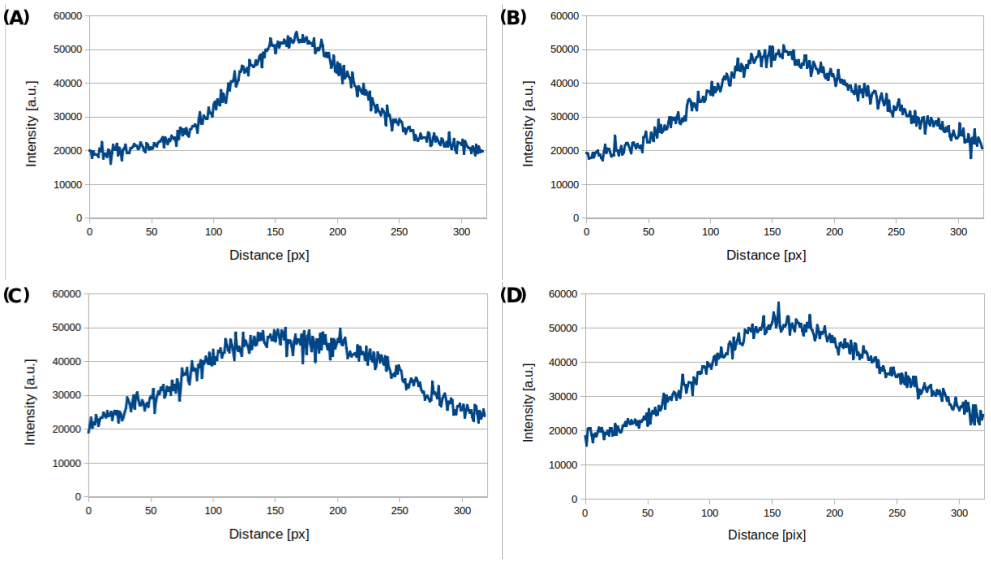

Figure 3.6 – Examples of intensity profiles for four telescope settings (2.35, 2.9, 3.1 and 3.35mm) using a fluorescent plate. The corresponding maximal power values are 167mW, 96mW, 71mW and 60mW.

a high transmittance around 1300nm and it is mounted on a motor that can rotate it and that can be controlled from the computer. The prisms of the negative dispersion unit act as polarizing CBS so the HWP has been placed before it and there is no CBS in the path. Removing the CBS saves some power.

Measuring the power after the objective is not possible during imaging so, to have a live readout of the power, a semi-reflective mirror (SRM) is added to the path. It reflects about 3% of the power towards a power meter. The power measured this way is proportional to the power after the objective.
Before an imaging session, the correspondence between the power measured by the power meter and the power after the objective is made for several values and this is later used to estimate the power at the surface of the sample.

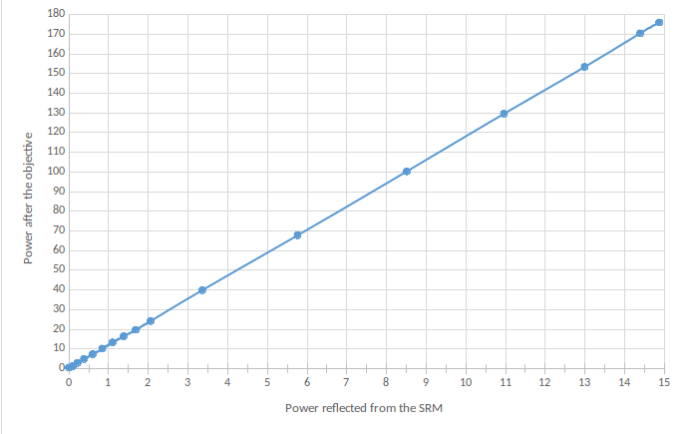

Figure 3.7 – Graph of the power after the objective according to the power reflected from the semi-reflective mirror (SRM). Data points correspond to measurements and a linear fit is used to estimate other power values.

3.5 Objectives and resolution

3.5.1 Description and use of the objectives

As mentioned in Chapter 2, the choice of the **objective** impacts the collection efficiency and the resolution of the microscope (see section 2.2.6). Its magnification will also impact the field of view and pixel resolution of the imaging as the number of pixels per frame is set by the scanning system.
Thus, we have three objectives that are used for different applications. One additional objective has been tested but did not satisfy us. These objectives and their characteristics are detailed in this section.

The **TL4X-SAP** from Thorlabs is an objective with a low magnification, 4X, a low numerical aperture, 0.2, a large working distance of 17mm and that does not require any immersion medium. It is not optimal for MPM but it enables a large field of view of 3.64mm x 3.14mm using 1PM which is very useful to map an imaging chamber before the start of the recordings and to orient oneself quickly. We are usually mapping out a new imaging chamber with this objective and 1PM and we use it as well at the start of every imaging session in NHPs to orient ourselves with 1PM and use the aforementioned map to select a region of interest (Figure 3.8).

The **XLPLN25XWMP2** objective from Olympus has been designed specifically for MPM. It has a high numerical aperture of 1.05, a high magnification of 25 and a small working distance of 2mm. The working distance is not sufficient for NHPs and is not compatible with the shape of our imaging chambers but it is ideal for mice image. It works under immersion and the correction collar can be

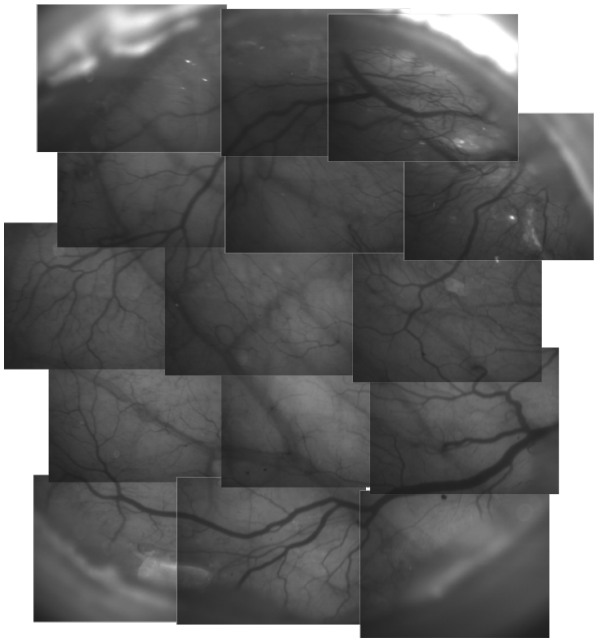

Figure 3.8 – Reconstruction of the chamber of one NHP using the Olympus PLN4X objective and 1PM.

adjusted to work with water.

The **XLSLPLN25XSVMP2** objective is similar to the XLPLN25XWMP2 with a numerical aperture of 0.95 but has a 8mm working distance that is better for NHPs. It also works under immersion and it's correction collar can be adjusted to work with water. However, considering the higher working distance, regular water can no longer be used. First, our chamber is not high enough to contain enough water, especially if the objective and chamber are tilted, so a gel has to be used. Second, distilled water and ultrasound gel absorb a lot of power [41]. We have tested other transparent and commercially available gels such as ocular lubricants, but the transmission was not improved. To palliate this issue, **deuterium oxide** (D_2O) can be used [71] [72]. A gel out of D_2O was developed by adapting the protocol for regular ultrasound gel, as described in Rothstein et al. [73] (see Appendix B).
The **transmission** through 8mm of immersion medium has been tested for water, ultrasound gel, a water gel made following the same protocol as for deuterium oxide and deuterium oxide gel made using carbopol. Using air as a reference, the transmission was 51%, 50%, 49% and 97% respectively.

The objective **CFI75 LWD 16x W** from Nikon has an intermediate magnification of 16, a numerical aperture of 0.8 and a working distance of 3mm. We were hoping we could use it for NHPs in place of the XLSLPLN25XSVMP2. Its

advantages are a larger field of view and the possibility to use deuterium oxide in a liquid form. However, the imaging quality was much worse, due to the lower NA. Also, the transmission of the objective at 1300nm is below that of the Olympus objectives, and so the imaging depth would have been more limited.

3.5.2 Evaluation of the resolution

The **resolution** can be measured using fluorescent beads with a sub-resolution diameter. The full-width at half maximum (FWHM) of the apparent size of the beads is used as the value of the resolution.
Using the XLPLN25XWMP2 objective, the FWHM of beads has been measured at 1300nm and 960nm along the three axis (Figure 3.9). The measurements are summarized in the following tables.

Axis	Median FWHM	Standard deviation	Number of beads
X	0.58 μm	0.067 μm	1418
Y	0.62 μm	0.048 μm	1525
Z	2.79 μm	0.73 μm	1487

Table 3.1 – Resolution of the microscope at **1300nm** using 0.5μm fluorescent beads.

Axis	Median FWHM	Standard deviation	Number of beads
X	0.58 μm	0.065 μm	1383
Y	0.61 μm	0.046 μm	1541
Z	2.80 μm	0.40 μm	1402

Table 3.2 – Resolution of the microscope at **960nm** using 0.5μm fluorescent beads.

These measurements are averaged over ten recording sessions spanning over three months which make them robust to small variations of alignment of the setup. The beads diameter, 0.5μm, is somewhat large and a more precise estimation of the lateral resolution could be obtained with smaller beads. However, the resolution of the microscope is well below neuronal cell bodies and is good enough to observe thick axons and boutons [74]. Besides, this is not the optimal resolution that one can get with this objective and this can be explained by the fact that we are only slightly overfilling the objective, in order to have more power at the sample.
The sample preparation, data acquisition and analysis are detailed in Appendix A.

3.5.3 Protecting the objective from external light

During imaging, it is essential that no external light from the monitors of the room be picked up by the objective and interpreted as fluorescence as this would increase the noise level. Yet, monitors may be used to present visual stimuli to

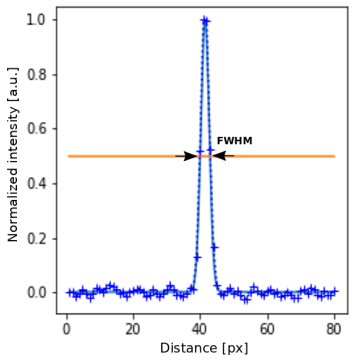

Figure 3.9 – Example of the measurement of the FWHM of one bead in one direction using a gaussian fit.

the animal during imaging. In order to solve this issue, we have designed and 3D-printed a cap for our XLPLN25XWMP2 and XLSLPLN25XSVMP2 objectives (Figure 3.10). It can slide up and down on the objectives to be able to visualize the chamber, refill the immersion medium if needed and be adjusted to the imaging depth. A ring ensures the stability and two handles have been added to help sliding the cap. The shape and resin (Elastic 50A, Formlabs) have been chosen to increase the flexibility of the cap. Since the resin is transparent, a black oil paint is sprayed to make it opaque.

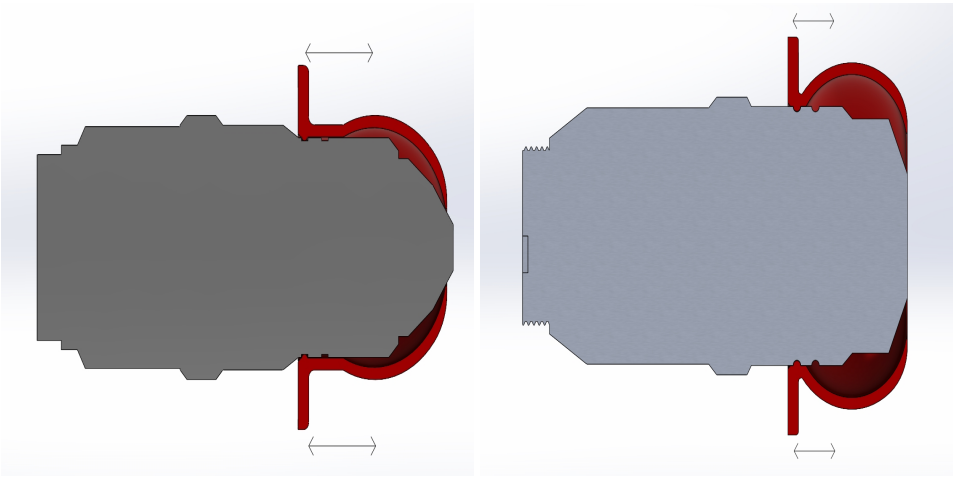

Figure 3.10 – Schematics of the XLPLN25XWMP2 (left) and XLSLPLN25XSVMP2 (right) objectives with the protective caps that are 3D-printed and can slide along the objective (arrows).

3.6 Scanning system

3.6.1 Resonant-galvo scanner

Our scanning system is composed of a resonant (CRS4, Cambridge technology) and a galvo scanner (6215H, Cambridge technology). The resonant mirror oscillates at a constant frequency of 4kHz and allows a faster imaging. The corresponding frame width is fixed to 160 pixels but we are generating images with a width of 320 pixels by interpolating the adjacent pixels. The galvanometric mirror adds flexibility with a variable amplitude of scanning. We are commonly imaging a field of view of 312x520 pixels (i.e. 620x630μm^2) with a 15Hz frame rate.

With the XLPLN25XWMP2 objective at magnification 1, the corresponding field of view is 620μm in the resonant direction and up to 1mm in the galvanometric direction. In order to further increase our field of view, we have an ETL (EL-10-30-TC, AQAC0843, Optotune) which enables us to image several planes simultaneously. However, this is at the expense of the frame rate. For example, we can image three planes simultaneously at a frame rate of 20Hz for the three planes with a field of view of 620μm^2. Imaging several planes simultaneously is useful to record a larger population of neurons at once for the same experiment and stimuli presentation.

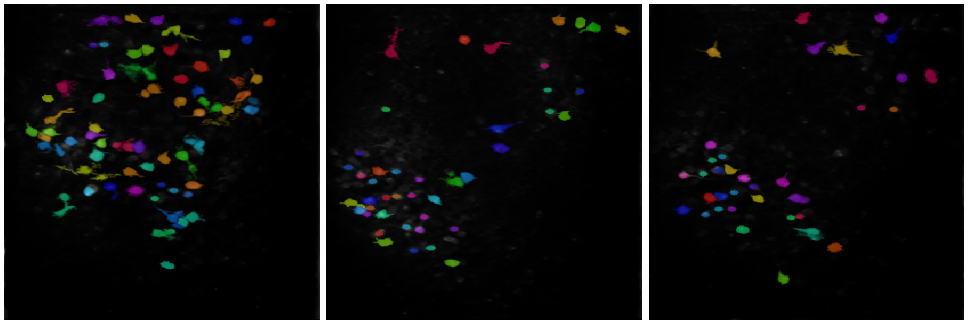

Figure 3.11 – Pictures of three planes imaged simultaneously. Averaged frames and cells marked using Suite2P.

3.6.2 Edge-blanking

During scanning, because of the resonant scanner, the laser beam slows down and focuses longer on the edges of the frames which can cause heating or damage of the tissue locally. To avoid this, **edge-blanking** is used : the laser beam is temporally blocked by a shutter when it scans the edges of the frame. The duration of the blanking can be adjusted in the software of the microscope, Scanbox (Neurolabware).
Besides, it is possible to either scan bidirectionally, half of the lines are scanned

from left to right and the other half are scanned from right to left, or unidirectionally, the laser beam is then blanked half of the time and all the lines are scanned in the same direction. Using unidirectional scanning leads to a frame rate twice lower than bidirectional scanning but the average power is also divided by two so it is possible to increase the power of the laser beam and therefore the pulse energy while maintaining a lower average power in the tissue.
To estimate the pulse energy at the focus of the objective, it is the average power after the objective without edge-blanking and using bidirectional scanning that should be taken into account. Indeed, this is the power that corresponds to the repetition rate and pulse energy of the laser.

3.7 Collection path

The photons that are emitted by the sample, including the fluorescence, are collected by the objective. A dichroic mirror (FF705-Di01, Semrock) filters them and directs them towards the PMTs (H16201-40, Hamamatsu). The PMTs convert the photons into an electric signal that is transmitted to the scanbox tower (Neurolabware) that handles the data acquisition. The setup has two PMTs preceded by two distinct filters : one for the green range of the visible spectrum (FF01-510/84, Semrock) and one for the red range (FF01-607/70, Semrock).

3.8 Addition of a two-photon microscopy optical path

In order to test the performance of the three-photon microscope, we have set up an optical path for 2PM in parallel to the 3PM one.
The wavelength can be adjusted at the level of the OPA and the built-in compression unit of the Opera-F is used. The wavelength we are using for 2PM has been chosen to get the smallest pulse width possible with our setup while remaining in the two-photon absorption range of the fluorescence spectrum of fluorescein dextran and GCaMP (Figure 2.4). At 960nm, the pulse width at the focus of the objective is 183fs, which significantly larger than what we have at 1300nm, but standard for a regular 2-photon microscope (Figure 3.12).

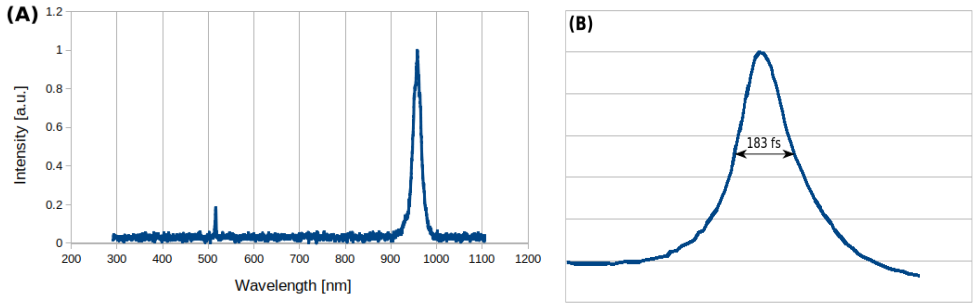

Figure 3.12 – (A) : Spectra of the signal beam at the output of the OPA for 2PM with a peak intensity at 960nm. (B) : Graph of the pulse width after the objective as measured with the autocorrelator, using the sech^2 setting for 960nm.

At 960nm, the average power at the output of the OPA is 2.54W. Similarly to the 3PM path, a 800nm high-pass filter followed by a 1000nm low-pass filter are positioned at the output of the OPA to improve the spectrum of the laser beam and a telescope is used to adjust the beam diameter and vergence.
Like in the 3PM path, a HWP is used to change the polarization of the laser beam, with a coating optimized for the lower wavelength (AHWP05M-980, Thorlabs). In this path, the HWP is positioned after the negative dispersion unit so a polarizing CBS is added after the HWP. In this path, more power is available and the imaging quality and maximal depth are not limited by power so having a CBS is not an issue. An advantage is that the reflection is more optimal so near zero power can be more effectively obtained.
After the CBS, the 2PM beam joins the 3PM optical path using a flip-mirror. The only difference in the rest of the path for 2PM imaging is that we have two ETLs, one for 960nm (EL-C-10-30-TC, AQAA0844, Optotune) and one with a specific coating for 1300nm (EL-C-10-30-TC, AQAC0843, Optotune).

3.9 Conclusion

In conclusion, it is possible to perform single-photon microscopy, 2PM and 3PM imaging at the same location of a sample using this setup, although not simultaneously. The repetition rate of the laser is 2MHz.
At 1300nm, the pulse width after the objective is 60fs and the maximum pulse energy available during imaging is 90nJ at the surface of the sample.
At 960nm, the pulse width is 183fs and the maximum pulse energy in similar conditions is 150nJ.

4 - IMAGING THROUGH THE DURA : A POST-MORTEM STUDY

The dura mater is a tough and opaque membrane enveloping the brain that protects it from mechanical constraints and infections. Its thickness widely varies across species : it is about 10μm thick for mice, 50μm in rats, 200μm in cats [75] and 450μm thick in macaque monkeys [69].
In small animals such as rodents and cats, it is possible to image through the dura to visualize blood vessels or voltage sensitive dyes in the cortex [27] [28]. However, the dura mater of macaque monkeys is too thick to image through it, even when using near infrared light [29] [30], so it needs to be surgically removed for intrinsic optical imaging or voltage sensitive dye imaging.
Similarly, the dura in small animals is thin enough to be imaged through with 2PM, while it is commonly surgically removed prior to 2PM in macaque monkeys [16] [31] [15] [16][32]. Even 100μm of dura is enough to compromise 2PM imaging with a regular two-photon microscope [16] [33]. It is thought that for long-term optical imaging, the dura can be replaced with an 'artificial dura', a silicone membrane placed at the surface of the cortex that maintains the edges of the natural dura away from the imaging site [76][32][77]. Yet, as soon as the natural dura is removed, granulation tissue starts growing on top of the cortex (sometime called a 'neomembrane'), and with time it will grow into a new dura [16] [69] [15] [78]. Also, any surgical implant will cause a foreign-body response, where the body will try to encapsulate the implant, first with soft and highly vascularized granulation tissue that develops into a tough collagen-rich layer of fibrosis over the course of around 4-6 weeks [79] [80] [81]. It is possible to slow down the foreign-body response by local application of dexamethasone [79] [82] [83], which is also used to prevent the formation of a neomembrane in imaging chambers [84]. However, this won't stop the regrowth completely, and generally has serious side-effects. In particular, dexamethasone has been shown to inhibit neuroplasticity [85]. Furthermore, dexamethasone treatment is generally combined with long-term antibiotics to compensate for the reduced immune response [84], which has an important risk for the development of antibiotic-resistant strains of bacteria.
As an alternative to the use of an artificial dura, it is also thought that applying some pressure with the imaging chamber on the dura will reduce the growth of granulation tissue [86]. However, excessive pressure will restrict blood flow [86], and can even locally compress the cortex below it [30] [78]. Therefore, 2PM in NHPs is either possible for acute recordings or the regrown dura has to be periodically removed [76] [16] [30] [15]. It is possible to surgical remove the neomembrane before it has developed into a regrown dura, but this is challenging as it is fragile and highly vascularized [84] [30]. Also, it is only possible for a limited amount of

times before the neomembrane starts attaching to the cortex and can no longer be removed without rupturing the blood vessels positioned on top of the cortex [15] [87].
All in all, the presence of the dura mater is one of the main obstacles of long-term and stable MPM imaging in larger animals than mice such as macaque monkeys. It is essential to find solutions for stable imaging, in particular for cognitive neuroscience where animals are extensively trained prior recording to perform complicated behavioral tasks.

In this chapter, the optical properties of *post-mortem* dura mater are studied at 1300nm and 960nm to infer on the feasibility of 2PM and 3PM through the natural dura and the imaging depth that could be reached.

4.1 Description of the project and objectives

If the dura mater is so disruptive to optical imaging, it is because it is made of a succession of layers of tissue creating as many interfaces for the light to be scattered. This has three main consequences on the imaging of the cortex below it :

- An attenuation of the power at the focus of the objective due to absorption and scattering happening in the dura.
- The creation of optical aberrations that can distort the point-spread-function of the laser beam and therefore reduce the optical resolution.
- The addition of a dense layer that can create out-of-focus fluorescence and therefore reduce the signal-to-background ratio.

The first two phenomena are studied at 1300nm and 960nm with a 2MHz pulsed laser and using a sample of post-mortem dura from a rhesus macaque monkey and polystyrene fluorescent beads.
Some of the questions we would like to answer are the amount of additional power that is required to image through the dura and the subsequent loss in imaging depth, as well as the loss in imaging quality.

4.1.1 Power attenuation through the dura

The dura mater, as for any layer of tissue, is a source of scattering and absorption that causes power loss as the laser beam goes through it. The attenuation of power can be estimated by measuring the effective attenuation length (EAL) of the dura mater. The dura itself does not have fluorescent markers but it is possible to image its second harmonic generation (SHG) at 960nm and 1300nm to visualize the structure of the dura. The emission will then be at 480nm and 650nm respectively so collected by the green channel for the study at 960nm and the red channel for the study at 1300nm. The EAL is expected to be larger at 1300nm than 960nm because the scattering by the tissue is less in the near infra-red range (Figure 2.3) so the dura mater would cause a larger drop in power for 2PM than 3PM.

4.1.2 Distortion of the point spread function and impact on the resolution

In MPM, the image formation can be modelled as the convolution of the object by the point-spread function (PSF) of the microscope. Because of scattering, the PSF of the laser beam may be distorted which can result in a distortion of the image of the beads and therefore impact the resolution of the microscope.
Besides, a distortion of the PSF will impact two- and three-photon excitation differently. For 2PM excitation, the signal generation is proportional to $1/z^2$ with z the distance relative to the center of the PSF, whereas it is proportional to $1/z^4$

for 3PM excitation (see Section 2.2.1), so a smaller portion of the PSF will contribute to three-photon excitation. Therefore, if the PSF becomes distorted and more spread out in space, three-photon excitation will still remain confined to a relatively small region within the PSF. This will reduce the fluorescence signal as the peak amplitude will be reduced, but it is not expected that the resolution be largely impacted. On the contrary, 2PM is less dependent on the spatial confinement of the PSF, so a larger portion of the PSF contributes to the fluorescence generation, and so the fluorescence signal will be less affected by a distortion while it will impact the resolution of the imaging more significantly.

To quantify this effect, fluorescent beads with a diameter of 500nm are imaged above and below the dura, for different thicknesses of dura. The apparent size of the beads in the axial direction will be used as a measure of the resolution.

4.2 Estimation of the effective attenuation length of the dura at 960nm and 1300nm

In this section, the EAL of a post-mortem sample of NHP dura mater is estimated at 960nm and 1300nm.

4.2.1 Sample preparation

First, agarose powder (Sigma-Aldrich) is diluted in distilled water with a ratio of 1.5 wt% and heated up on a hot plate until the solution clears up and becomes homogeneous. Then, fluorescent polystyrene beads (FluoSpheres carboxylate, Invitrogen, yellow-green (505/515), 0.5μm, 2% solids) are added to the agarose to a concentration of 0.1wt%. The concentration of beads has been set to have enough of them spread around the sample while being able to study them individually. The liquid agarose mixed with fluorescent beads is poored in a cell culture petri dish. Once the agarose solution is cooled down to about 30°C, a post-mortem piece of dura of about 0.5cm x 1cm is immersed in it. A coverslip is then placed on top and distilled water can be used to ensure that no air be trapped below the coverglass. Agarose is used to seal the edge of the coverslip and a layer of distilled water is kept at the surface of the sample to avoid drying of the agarose.

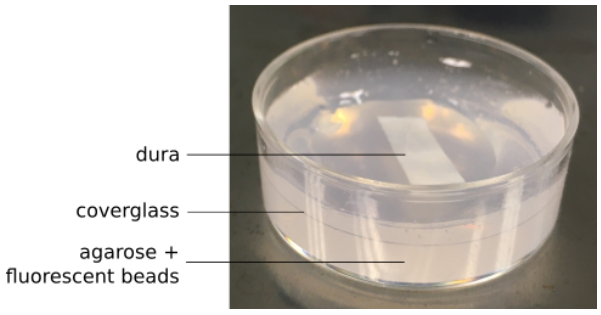

Figure 4.1 – Picture of the sample : a piece of post-mortem dura is embedded is a solution of fluorescent beads and agarose and covered by a coverglass.

4.2.2 Microscope alignment

Before each imaging session, the alignment of the microscope is checked using fluorescent beads embedded in agarose without dura on top. The beam is first focused on the coverslip and if needed, the objective is rotated to ensure that it is orthogonal to it. Then beads are imaged and their shape should be ellipsoidal. If not, this means that the laser beam does not come in straight into the microscope, which can be corrected by better alignment of the beam.

4.2.3 Estimation of the effective attenuation length

We have established that the intensity of a laser beam travelling through a sample of EAL l_e is given by : $I(z) = I_0.exp(-\frac{z}{l_e})$ (see Equation 2.1). Besides, for 2PM, $F = \frac{1}{2}.\sigma.I^2$ (see Equation 2.2). Therefore,

$$F(z) \propto F_0.exp(-\frac{2z}{l_e}) \tag{4.1}$$

with $F(z)$ the normalized fluorescence intensity at a depth z inside the sample, F_0 the normalized fluorescence intensity at the surface of the sample and l_e the EAL of the sample.
Similarly, if the fluorescence is generated by 3PM,

$$F(z) \propto F_0.exp(-\frac{3z}{l_e}). \tag{4.2}$$

To estimate the EAL, a z-stack of the dura is performed with a 3μm step and 15 to 40 frames per plane over the full thickness of the dura. The signal quickly drops with depth during these recordings, so small z-stacks are acquired with different power values to avoid large variations of signal intensity over depth.

Then, for each plane, the frames are averaged and the mean intensity of the 1% brightest pixels is calculated. This intensity is then divided by the square of the power measured at the surface of the sample as the signal corresponds to the SHG for both 960nm and 1300nm.
This is plotted against depth in a semi-logarithmic scale and the EAL is estimated using the slope coefficient of the linear regression using the following formula : $l_e = 2/a$ with a corresponding to the slope coefficient (Figure 4.2).

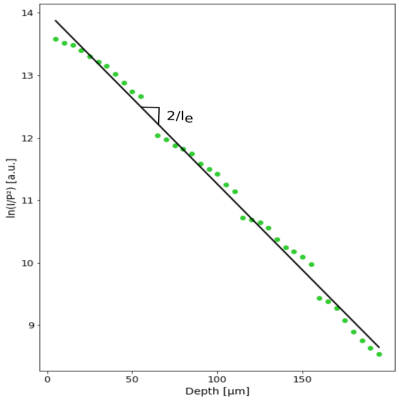

Figure 4.2 – Plot of the intensity of the post-mortem dura sample according to the imaging depth (green dots). The intensity is measured as the mean intensity of the 1% brightest pixels of the frames. A linear fit is used to estimated the effective attenuation length from the slope coefficient.

4.2.4 Results and discussion

The EAL was estimated at 6 different locations of the dura at 1300nm and 960nm for thicknesses ranging from 160 to 215μm. The estimations of the EAL as well as the coefficient of determination (R^2) of the linear fit are given in the following table.

Acquisition	EAL at 1300nm	R^2 at 1300nm	EAL at 960nm	R^2 at 960nm
1	82.0	0.997	41.3	0.938
2	74.9	0.972	48.1	0.915
3	82.0	0.949	63.7	0.928
4	73.6	0.987	52.0	0.971
5	82.3	0.948	70.2	0.986
6	89.4	0.975	54.8	0.926
6b	89.8	0.951		

The average EAL at 1300nm is **80.7$\pm$5.3μm** and it is **56.5$\pm$10.1μm** at 960nm.
One acquisition was repeated twice (acquisitions 6 and 6b) at 1300nm, before and after the corresponding acquisition at 960nm, and lead to consistent values.

The EAL is higher at 1300nm than 960nm which is expected since the combined effect of absorbance and scattering of the tissue have less impact at 1300nm (see Figure 2.3).
These values are small compared to the EAL of the mouse cortex, which is between 250 and 300μm for 1300nm [41], and comparable to the value for white matter, which is about 100μm for 1300nm [53]. This shows how disruptive the dura is to MPM imaging and explains why a durectomy is commonly performed prior to imaging.

4.2.5 Model of the maximum imaging depth below the dura

Knowing the effective attenuation length of the dura, it is possible to estimate the maximal imaging depth inside the cortex using 2PM or 3PM, similarly to section 3.2.1. This is without taking the signal-background ratio into account, and assuming one laser pulse per pixel and a required signal strength of 0.1 photons per pixel (see Section 3.2.1).

Let's consider a dura mater of thickness d at the surface of the cortex and set z the depth inside the cortex (without taking into account the dura), l_e^d and l_e^c the EAL of the dura and cortex respectively, I_0 the laser intensity at the surface of the dura mater.

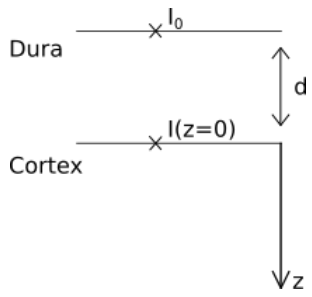

$z^d_{max} = ln(\frac{P_{0max}}{E_{lim}.R})l^c_e - \frac{d}{l^d_e}.l^c_e$

We have $I(z) = I(z=0).exp(-\frac{z}{l^c_e})$
and $I(z=0) = I_0.exp(-\frac{d}{l^d_e})$ (Equation 2.1).
So, $I(z) = I_0.exp(-\frac{d}{l^d_e} - \frac{z}{l^c_e})$
i.e. $ln(\frac{I_0}{I(z)}) = \frac{d}{l^d_e} + \frac{z}{l^c_e}$
and $z = ln(\frac{I_0}{P(z)})l^c_e - \frac{d}{l^d_e}.l^c_e$.

Therefore,

$$z^d_{lim} = ln(\frac{I_{0max}}{E_{plim}.R})l^c_e - \frac{d}{l^d_e}.l^c_e \tag{4.3}$$

$$z^d_{lim} = z^c_{lim} - d.\frac{l^c_e}{l^d_e} \tag{4.4}$$

with z^d_{lim} the maximum imaging depth inside the cortex with a dura layer of thickness d above, I_{0max} the maximum laser intensity that can be used at the surface of the tissue without causing damage and E_{plim} the minimum pulse energy that is required to generate fluorescence.

In the Equation 4.3, one can recognize the expression of the limiting imaging depth in the absence of dura (Equation 3.1). Therefore, the presence of a dura mater of thickness d causes a **corresponding loss of imaging depth of** $d.\frac{l^c_e}{l^d_e}$.

This equation can be used to plot the maximum imaging depth inside the cortex according to the thickness of the dura and the repetition rate of the laser for 2PM and 3PM (Figure 4.3).

According to this model, with a large repetition rate (about 80MHz) and in the absence of dura it is possible to image the cortex down to about 400μm using 2PM. However, any regrowth of tissue is highly detrimental and 100μm of dura is sufficient to limit the imaging to the first 100μm of the cortex. This is in line with previous findings in macaque monkeys, where 2PM is often limited to layer 1 [77] [32].
By lowering the repetition rate to 0.8-4MHz, which is common for 3PM, it is possible to image deep into the cortex for both 2PM and 3PM, even in the presence of several hundreds of micrometers of dura above the cortex. Using a repetition rate of 2MHz, this model predicts that we should be able to image down to 400μm into the cortex with up to 250μm of dura for 3PM and up to 200μm for 2PM, which is impressive.

It is important to keep in mind that this model only takes into account scattering and absorption inside the tissue, and does not consider the signal-to-background ratio, which is expected to be particularly problematic for 2PM.

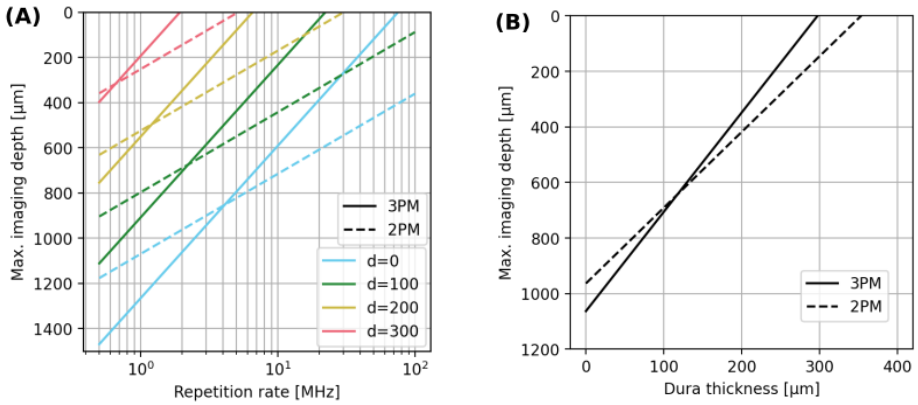

Figure 4.3 – (A) : Plot of the maximum imaging depth inside the cortex according to the repetition rate of the laser for different thicknesses of dura for 2PM (960nm) and 3PM (1300nm). (B) : Plot of the maximum imaging depth inside the cortex according to the thickness of the dura for 2PM at 960nm (dashed) and 3PM at 1300nm (continuous) for a fixed repetition rate of 2MHz.

4.3 Estimation of the resolution below a layer of dura mater at 960nm and 1300nm

In this section, the apparent size of fluorescent polystyrene beads in the axial direction is estimated for different thicknesses of dura to estimate the loss in resolution caused by a layer of dura mater.

4.3.1 Estimation of the resolution

As for the previous recordings (see subsection 4.2.2), the alignment of the microscope is checked at the beginning of each session.

Data acquisition

To estimate the resolution of the microscope in the absence of the dura, beads in a location of the sample away from the dura are imaged. A z-stack with a 1μm step and 15 frames per plane is acquired over 100μm to record about 100 beads. This z-stack is acquired at 1300nm and 960nm. The mean intensity of the fluorescent beads remains constant over the 100μm z-stacks so the power can be kept constant during this recording.

For the beads below the dura, a location of the dura mater is chosen and its thickness is measured. To record the intensity of the beads, a z-stack with a 1μm step and 15 to 50 frames per plane is recorded from 200μm to 100μm below the dura. Beads at the same location are recorded at 1300nm and 960nm.

Depending on the thickness of the dura, the power may need to be adjusted during the recording to maintain a similar intensity throughout the recording. Beads are not recorded just below the dura because, at 960nm, the SHG signal of the dura is recorded in the same channel as the 2PM signal of the beads which would increase the background fluorescence and could lead to an underestimation of the resolution (which is not the case at 1300nm). Also, since layer 1 of the cortex barely contains any neurons, it seems more relevant to compare the apparent size of the beads at larger depths.

Data analysis

To estimate the resolution, the axial resolution is considered because it is significantly lower than the lateral resolution in MPM. In addition , the beads have a diameter of 500nm which is more suitable to study the axial resolution (see section 3.5.2).
First, the frames of each plane of the z-stack are averaged and the module "3D Objects Counter" of Fiji is used to locate the position of the beads. The Tiff file of the averaged z-stack as well as the coordinates of the beads are the loaded into Python.

To estimate the resolution along the axial direction, the intensity of the pixels in the planes orthogonal to this axis are considered at every step and the average of the 5% brightest pixels is used as the intensity of the bead for the step. This step corresponds to the step size of the z-stack : it is supposed to be 1μm but a precise value is calculated using the the axial coordinate of the beginning and the end of the stack. The dimension of the planes that are averaged is chosen to be larger than the beads and is 11x15 pixels (i.e. 2.2μm x 2.2μm) (Figure 4.4.A). Averaging the intensity of selected pixels over a plane is done to avoid an error due to an imprecision on the center position of the beads that is given by Fiji.
The intensity of each bead is then normalized and plotted against the distance. It is fitted to a gaussian curve and the resolution is given by the average of the full width at half maximum (FWHM) of the beads that have been fitted with coefficient of determination higher than 0.9 (Figure 4.4.B). The analysis is detailed further in Appendix A.

4.3.2 Results and discussion

We have measured the apparent size of polystyrene fluorescent beads that measure 500nm in diameter that were positioned below a piece of post-mortem rhesus macaque monkey dura tissue with a thickness ranging from 0 to 190μm.

In the absence of dura, the apparent size of the beads is similar for the two wavelengths, with a median of 2.79μm at 1300nm and 2.80μm at 960nm (see

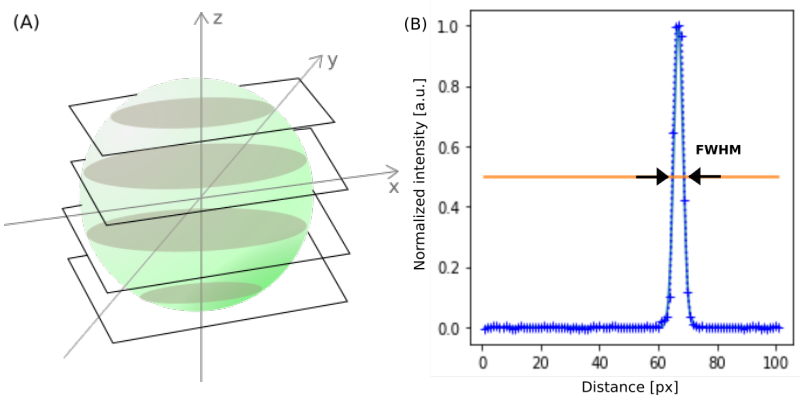

Figure 4.4 – (A) Schematic of the analysis process to measure the apparent size of a bead along the axial direction. The 5% brightests pixels out of a 2.2 x 2.2 μm^2 square around the center coordinate of the bead are averaged at every step of the z-stack. (B) Plot of the normalized intensity of one bead that is fitted to a gaussian curve to estimate the apparent size of the bead using the FWHM.

Section 3.5.2). The resolution starts decreasing at 70μm at 960nm while it remains constant up to 165μm at 1300nm. For larger thicknesses, the resolution drops faster for both wavelengths (Figure 4.5). Some measures has been made for a thickness of 220μm as well but the signal-to-background ratio was approaching 1 and no useful information could be extracted (see Appendix A.3).

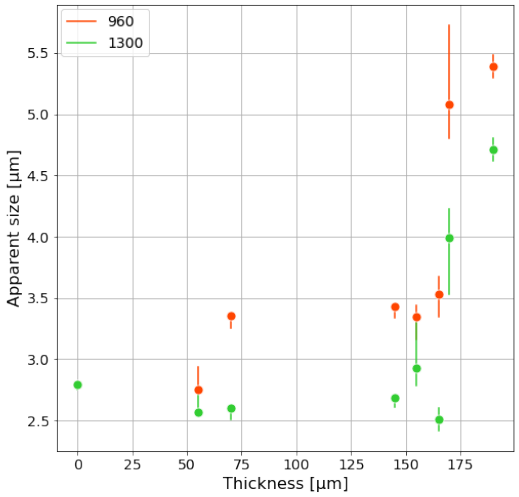

Figure 4.5 – Plot of the apparent size of polystyrene fluorescent beads that are position below a post-mortem dura of varying thickness. The dots correspond to the median and the error bars to a 95% bootstrap confidence interval. The apparent size of the beads is indistinguishable in the absence of dura.

In conclusion, the resolution of both 2PM and 3PM are impacted by the presence of a layer of dura mater at the surface of the sample. The impact is larger on 2PM but the trend seem similar and 165μm appears as a cut-off thickness when considering the deterioration of resolution. This is rather surprising as we expected the resolution to be better preserved for 3PM.
An additional observation is that post-mortem tissue usually shrinks by 20 to 30% during the fixation process [88] so 165μm of fixed tissue would actually correspond to 210 to 235μm of *in vivo* tissue.

4.4 Conclusion

In this chapter we have studied the dura mater using a post-mortem sample. We have further detailed the model established in Section 3.2.1 by taking into account the presence of a layer of dura mater at the surface of cortex. The effective attenuation length of dura mater has been estimated using the post-mortem sample to predict the maximum imaging depth inside the cortex according to the repetition rate of the laser, the non-linearity order of the excitation process and the thickness of the dura mater. This model predicts the possibility to image down to 400μm inside the cortex using a regular 2PM setup in the absence of dura mater but that any regrowth of tissue would prevent the imaging. However, for lower repetition rates, it would be possible to image over 1mm of cortex using either 2PM or 3PM.
Yet, this model does not consider the loss of signal-to-noise ratio due to an increased background signal caused by fluorescence emitted close to the surface of the sample. This is particularly an issue for deep imaging using 2PM.

Another consequence of the presence of dura mater at the surface of cortex is the distortion of the point-spread function of the laser beam that can lower the resolution. This has been tested of polystyrene beads positioned below a layer of post-mortem dura mater of varying thickness. It has been found that, although the resolution is similar without the layer of tissue, the resolution starts decreasing with a 70μm-thick layer of dura mater at 960nm while it is preserved for dura thicknesses lower than 155μm at 1300nm. Finally, there appears to be a cut-off thickness of 165μm after which the resolution degrades rapidly. This thickness of post-mortem tissue would correspond to 210-235μm of in-vivo dura when considering the shrinkage induced by tissue fixation. Following this study, we can postulate that, beyond 210μm of scattering tissue at the surface of the cortex, the imaging quality is significantly deteriorated and this can prevent the imaging of fine structures such as neuronal dendrites and boutons.

5 - MULTI-PHOTON IMAGING IN NON-HUMAN PRIMATES

MPM imaging in macaque monkeys requires specific adaptations of the setup as well as the implantation of a dedicated imaging chamber. For awake imaging, animals also need to be implanted with a headpost and viral injections are required for functional imaging. Yet, despite all these technical advances, the dura remains a limiting factor for *in vivo* MPM imaging in large animals.

5.1 Animal procedures

5.1.1 Designing the headpost and the imaging chamber

Headposts

The headpost is an implant that is fixed to the skull of the animal and is used to maintain its head immobile. The main parameters to consider when choosing or designing a headpost are its **sturdiness**, the headpost has to withstand the constraints due to the animal moving while being head-fixed, and its **biocompatibility**, the implant should be accepted by the body. Biocompatibility is also key to osseointegration, meaning the encapsulation of the implant by bone over time [89][90][91].

In order to satisfy these requirements, the choice of the materials composing the headpost and its shape are essentials. Medical grade titanium grade 5 has been chosen for the latest headposts because it is lighter and more biocompatible than medical grade stainless steel while maintaining a great yield strength (resistance to deformation), albeit being somewhat less stiff than stainless steel [92]. While pure titanium is the most biocompatible, it has a low yield strength. Titanium grade 5 has been specifically developed to have a high yield strength, and is therefore most commonly used for medical implants [93]. Although titanium is less stiff than stainless steel, it is still much more stiff than bone. It is this mismatch that is thought to make implants less biocompatible, which could potentially be overcome by making the surface of the implant porous [93][92]. Also, a porous interface is thought to promote osseointegration, in particular when combined with hydroxyapatite, a material that is slowly absorbed by the tissue [89][94]. Our implants are therefore coated with thin layers of titanium oxide and hydroxyapatite (each of them 60μm thick).
As for its shape, a CT scan of each animal is performed and headposts are custom

made to fit the shape of the skull and taking into account the desired position of the future imaging chambers that are intended for each animal (Figure 5.1). Relatively large legs are used for the headpost to increase the stability, which is crucial for high resolution imaging. First, the bone screws at the end of the legs grab into the bone at larger angles relative to each other (like the legs of spiders). This is similar to the practice of triangulation in structural engineering (e.g. in bridges and space frames). Furthermore, the legs are placed such that the different cranial bones are all connected. Finally, the skin around the implant tend to retract over time. By extending the legs, the tips of the legs will be further removed from the part of the implant that is exposed, and therefore will remain better protected by the skin above it. A downside of a large legs is that the implant will be heavier, and it leaves less room for additional implants like the imaging chambers. Commonly, a headpost contains one central fixation point that extrudes through the skin, but it is possible to design a headpost with multiple fixation points. The advantage of additional fixation points is a better stability and therefore a reduction of the motion artefacts during recordings. Again, it is useful to place the fixation points at different angles relative to eachother for improved stability [95].

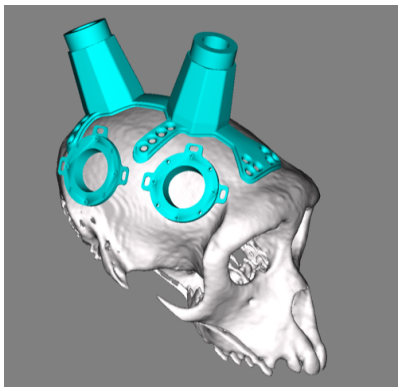

Figure 5.1 – Model of a headpost and two imaging chambers, form-fitted to the surface of the skull of a macaque monkey, extracted from a CT scan. The position of the legs of the headpost are chosen according to the location of the imaging chambers.

Imaging chambers

An imaging chamber is an interface between the cortex and the outside world that allows imaging the cortex while protecting it from mechanical damage and pathogens. The chamber has to be stable and well attached to the skull, as well as biocompatible to maintain clean wound margins over time. This MPM setup has been designed for cognitive neuroscience experiments and the chambers should be stable for several years.

The chambers that we have designed are made of grade 23 titanium (a more

pure but expensive variant of grade 5) and the surfaces that are in contact with the skull are coated with titanium oxide and hydroxyapatite to promote osseointegration.
Although the insert containing the glass interface does not need to be removed to perform MPM, it is essential to be able to remove it to do viral injections inside the cortex for functional imaging or to clean in case of local infections. For this purpose, the chamber is composed of three parts : a ring, an insert and a lid (Figure 5.2).
The **ring** is attached to the skull using three bone screws, ensuring the mechanical stability of the chamber. The ring is not meant to be removed once it has been implanted. Over time, the ring should merge with the underlying bone thanks to osseointegration.
The **insert** can be attached to the ring using four screws. These screws are M2-3 stainless steel screws with an hexagonal socket flat head which ensures a more resistant socket. This part can be removed to access the brain and can be changed : inserts of several heights are made to match the thickness of the skull and adjust the pressure applied by the imaging window on the dura and cortex below it. The ring has a small ridge on which is resting the coverglass that is used as the imaging interface. The coverglass is 15mm wide and 0.23mm thick (72227-01, Electron Microscopy Sciences), and is fixed to the insert using dental cement (Super-Bond, C&B), both from the top and the bottom side of the insert to smooth the edge between the insert and the coverglass. We have tried applying a layer of silicon gel (Kwik-sil, WPI) on the bottom side of the coverglass to improve the biocompatibility, but we have not seen an advantage in terms of biocompatibility, similar to previous reports [16]. In particular, we observed that the silicon gel was sometimes sticking to the surface of the cortex, which compromised the removal of the insert.
The **lid** can be positioned on top of the insert using four screws as well. The lid is used to protect the cover glass from mechanical damage and keep it clean.

Special care was taken to seal the inside of the chamber from the outside. A rubber ring is placed between the ring and the insert as well as between the insert and the lid. In addition, the screws are positioned inside the rubber rings and the threads of the screws from the lid do not go through the insert. Finally, osseointegration should ensure that a seal is provided between the bottom of the ring and the skull.

The chamber has been designed to be thin enough so that the objective XLSLPLN25XSVMP2 can be used to record from the cortex while remaining above the chamber. This is useful to allow the chamber to remain small in diameter and still be able to image the whole chamber, without being mechanically restricted by the edges. The thickness of the chamber above the skull is 2.5mm and the height of the insert ranges from 1.5 to 3mm. So the chamber is 4 to 5.5mm high in total,

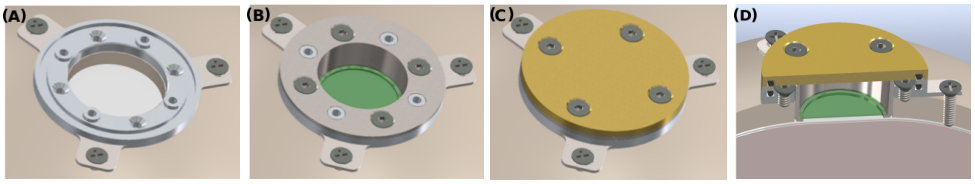

Figure 5.2 – Schematics of the imaging chamber with (A) the ring that is screwed in the skull, (B) the insert with the imaging window (green) screwed onto the ring and (C) the lid (yellow) closing the full chamber. (D) A section view of the full chamber with the two rubber rings (black) onto the skull (cream), the dura (white) and the cortex (pink).

while the working distance of the objective is 8mm, leaving enough room between the objective and the top of the chamber (Figure 5.3).

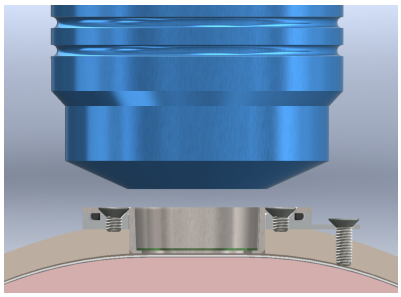

Figure 5.3 – Model of the XLSLPLN25XSVMP2 objective above the chamber. The focal point of the objective is at the surface of the dura (white) in this picture. The chamber (gray) is screwed into the skull (cream) above the dura (white) and the cortex (pink).

5.1.2 Surgical procedures

Prior surgery, the head of the animal is thoroughly shaved, cleaned and disinfected (vetedine savon and vetedine solution) before it is brought to the surgery room.

During the surgical procedures, the animal is under general anesthesia (induction using ketamine and dexdomitor and maintained using gaseous sevoflurane) and hydrated using an intravenous line of glucose 5%. Its head is held in position using a stereotaxic frame (Kopf 1530). A good hydration and a good posture with the head held higher than the body helps lowering the brain pressure to avoid swelling during the procedures [84].

At the beginning of the surgery, sub-cutaneous injections of adrenaline can be used for vasoconstriction and lidocaine for local pain management.

Implantation of the headpost and the imaging chamber

The first surgical procedure is the implantation of an imaging chamber as well as a headpost. The skin is opened using a coronal cut. This cut is preferred to a longitudinal one as lateral areas are more vascularized [96] which is considered to be advantageous for the healing process and can be placed such that it is less overlapping with the implants positions.
For an implantation of the imaging chamber over the ventro-lateral prefrontal cortex (vlPFC), the temporal muscle is detached from the skull without being resected. Relatively young and female animals are chosen as their cranial muscles are relatively thin. Both the imaging chamber and the headpost are positioned on the skull to choose the optimal position of the former and the skull is locally flattened with a drill to improve the fixation of the imaging chamber and minimize any gap between it and the skull.
A craniotomy of 18mm in diameter is performed using a hand-held Horsley trephine (Cross Instruments Inc.), and a Kerrison rongeur (Aesculap, Inc.) for the removal of small ridges of bone around the edges of the craniotomy. Care is taken not to damage the dura while performing the craniotomy. The lid and insert are then screwed onto the ring before using bone screws to screw the ring to the skull. Assembling the chamber ensures that the ring does not get deformed in the process. The depth of the insert is chosen according to the skull thickness. The imaging window should be in contact with the dura or cortex below it without applying too much pressure on them. Using a curved glass for the imaging window could be helpful to apply a more homogeneous pressure on the tissue below the window [97], but it is not clear how much a curved interface would affect the imaging quality for 3-photon imaging.
Once the imaging chamber is in place, the headpost can then be attached to the skull using bone screws. We have chosen not to use dental cement to attach the imaging chamber, nor the headpost, because it is less biocompatible than the implants themselves and we wish to maintain clean wound margins to limit the risk of infection or an inflammatory response and the growth of tissue at the surface of the cortex.
Finally, the skin is sutured over the complete imaging chamber to optimize the healing and integration process as well as minimize the risk of infections. It will be reopened five to eight weeks later to access the chamber, either to perform viral injections or imaging. In order to close back the skin, a small incision is made at the position of the pole of the headpost that is passed through it and the skin is sutured back along the original coronal cut. Using a small incision and suturing the skin away from the extruding pole has lead to a cleaner wound margin in our experience (Figure 5.4).
The early implantation of a headpost is a great advantage to be able to regularly check and clean the wound margins around the imaging chamber as well as inspect the inside of the imaging chamber by opening the lid, without using anesthesia.

Opening the skin over the chamber

Five to eight weeks after the implantation of the imaging chamber, a circular incision, slightly smaller than the chamber's diameter, is made over it. This small opening has the advantage not to require sutures and leaves a wound margin that fits tightly around the chamber edges (Figure 5.4). After a healing period of 2-4 weeks, the lid can easily be opened and closed.
The temporal muscle may need to be partially resected if it covers the chamber.

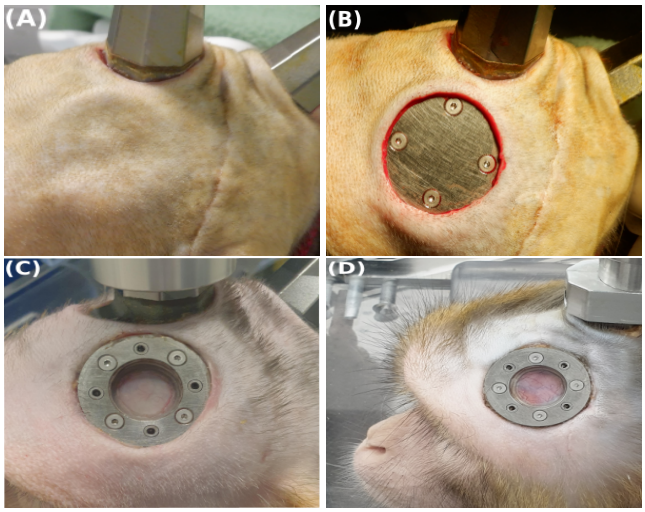

Figure 5.4 – Pictures of the chamber implantation process. (A) : At the end of the implantation surgery the skin is sutured over the chamber and an incision is made to let the post through the skin. (B) : Five to height weeks post-implantation a circular incision is made over the chamber. (C,D) : One month post-opening of the skin, the wound margins are stable for the two animals.

Evolution of the imaging chamber

Once the skin is opened over the chamber, it needs to be regularly cleaned (at least twice a week using local antiseptics) to prevent infections and the lid of the chamber is opened at least once a week to check that there is no infection inside. The animals are also implanted with a headpost which makes the cleaning process easier and safer for the animals that do not need to be anesthetized.
While the dura mater is a white and opaque membrane, it quickly thins down and becomes more transparent once the imaging chamber is implanted and applying pressure on it. It is then possible to visualize the sulci through the dura. After the first few weeks, the thickness becomes stable (Figure 5.5).

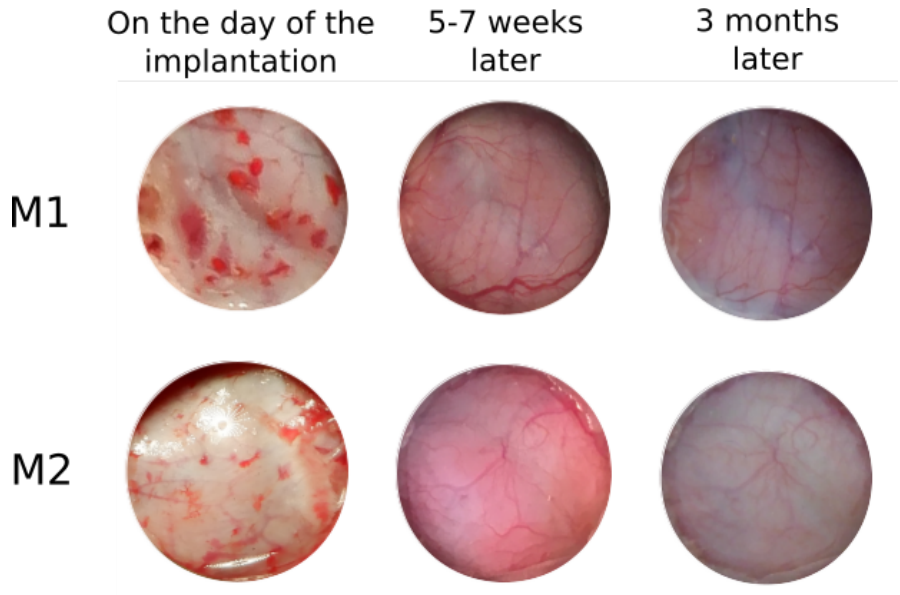

Figure 5.5 – Pictures of the imaging chamber of the two NHPs on the day of the chamber implantation (without the imaging window on top), 5-7 weeks later and 3 months after implantation (with the imaging window in place). The pictures taken during the implantation of the chamber and 5 to 7 weeks later are taken under anaesthesia while the latest ones are taken awake which explains the differences in coloration.

5.2 Imaging through the natural dura

In two NHPs, the dura was left intact during the implantation of the imaging chamber to study its optical properties *in vivo* using MPM and to compare them to the post-mortem data. In addition, we were interested in quantifying the power that is required to image through the dura and the corresponding loss in maximum imaging depth to test the model made in Section 4.2.5. This study has been carried out at 1300nm for 3PM and 960nm for 2PM and using fluorescein isothiocyanate–dextran (Sigma-Aldrich, FD70S) injected intra-venously (1mL/kg with a 5wt% solution).

5.2.1 Optical properties of the dura

EAL of the dura

Similarly to what was done using a post-mortem piece of dura mater, the recording of the SHG of the natural dura can be used to estimate the EAL at 1300nm and 960nm.
It is also possible to use the fluorescence signal generated by fluorescein dextran to estimate the EAL and this is what will be done inside the cortex but inside the dura the blood vessels are restrained to specific and discrete depths so the SHG is used instead and provides an homogeneous labeling.

Z-stacks are recorded with 40 frames per step and a 10μm step. However, unlike the post-mortem recordings, there are motion artefacts during the recordings. The animal is under anesthesia (sevoflurane) and breaths using a ventilator which creates a substantial axial motion following the breathing pattern. For each step of each stack, 10 consecutive frames out of the 40 are hand-selected. These frames are then averaged and can be used for the following analysis.

The estimations are summarized in the following table, the EAL values and the dura thicknesses are in μm.

Animal	EAL (1300nm)	r^2	EAL (960nm)	r^2	Dura thickness
Monkey 1			150.8	0.900	120
			147.4	0.907	140
	81.5	0.950	91.5	0.924	145
	85.7	0.973	88.4	0.972	155
	105.4	0.912	122.0	0.915	155
	85.8	0.915	97.2	0.965	170
	95.0	0.975			180
Average	**90.7$\pm$8.6**		**116.2 $\pm$25.7**		
Monkey 2			70.4	0.976	230
			205.6	0.922	270
			176.5	0.917	300
	190.2	0.932	176.3	0.924	305
	238.4	0.946	227.4	0.975	350
	161.3	0.980	142.8	0.947	400
Average	**196.6 $\pm$31.8**		**166.5 $\pm$50.4**		

First, it was not always possible to have an estimation of the EAL with a determination coefficient higher than 0.9 which is what we have selected as a threshold.

There is no significative difference between the EAL estimation of the dura mater at the two wavelengths used for the analysis for each animal individually (Mann-Whitney U test, p=0.08 and p=0.86 respectively) (Figure 5.6).
This does not match the post-mortem data analysis for which the EAL was larger at 1300nm which is similar to what is known for the mouse cortex. The theoretical model of the EAL of the cortex is based on water absorption and scattering measured inside a solution of particles meant to mimic cortex tissue [43] so it could be that the absorption and scattering properties of dura mater be dissimilar to that of the cortex.
An alternative hypothesis is that the signal generated by fluorescein dextran interferes with the EAL estimations at 960nm. Indeed, at 1300nm, the SHG signal of the dura fibers is recorded by the red channel of the microscope while the three-photon excitation signal generated by fluorescein dextran is recorded by the green channel.

This is no longer the case at 960nm and both are recorded with the green channel. Therefore, although an attenuation of the overall signal can still be observed and analyzed, it may no longer be comparable to the EAL measured at 1300nm.
To test this, with have recorded a z-stack of the dura mater at 960nm, before and after the injection of fluorescein dextran. While the EAL was 99μm before the injection of dextran, it became 176μm afterwards. At 1300nm, it went from 190μm to 178μm. The presence of the markers inside the blood vessels may have led to an overestimation of the EAL at 960nm and the later may actually be lower than the EAL at 1300nm, as expected from the post-mortem data and the literature.

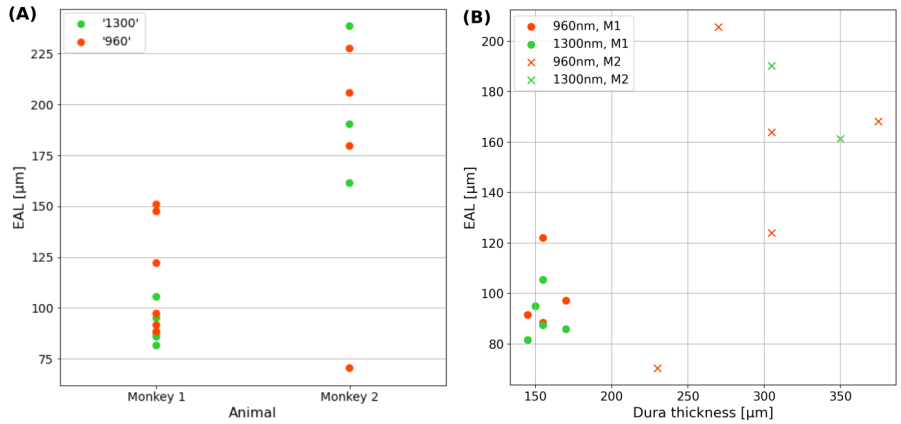

Figure 5.6 – (A) : Effective attenuation length (EAL) of the dura mater of two rhesus macaque monkeys (M1 and M2), grouped by animal. (B) : EAL according to the thickness of the dura mater.

Another interesting point about this dataset, is that the EAL of the dura seems to be different between the two animals. The subjects are two six-year old female rhesus macaque monkey with similar heights and weights. However, during the implantation of the imaging chambers, a deeper insert that applies a larger pressure onto the dura mater was implanted in Monkey 1. As a result, its dura thinned down to a greater extent down to 120-170μm whereas it ranges from 190 to 375μm for Monkey 2. The hypothesis is that, as the dura is pressed down by the imaging chamber, it gets denser and its EAL decreases. This would explain the larger EAL measurements in Monkey 2 (Figure 5.6).
One way to test this is to investigate the maximum imaging depth according to the thickness of the dura mater. If the EAL of the dura mater decreases as the dura gets thinner and perfectly compensates for it, then the maximum imaging depth below the dura mater should remain constant independently of its thickness. On the contrary, if the EAL remains constant when the dura thins down, then the maximum imaging depth should decrease linearly with the dura thickness according to Equation 4.4. However, this model does not take into account the increase of background signal and the corresponding loss of signal-to-background

SBR that can further limit the imaging depth. Furthermore, we are limited by power at 1300nm so our maximum imaging depth is underestimated at that wavelength.

In conclusion, we have not found a significative difference between the EAL at 960nm and 1300nm and this can be because the signal generated by dextran is recorded from the same channel as the SHG of the dura at 960nm and not at 1300nm.
Besides, the EAL of the dura mater may vary between individuals or we may be changing the EAL of the dura mater by implanting the imaging chamber on top of it and applying pressure.

EAL of the cortex of NHPs *in vivo*

Thanks to the intravenous injections of fluorescein dextran, it is possible to estimate the EAL of the cortex as well. The vasculature is then used instead of the tissue and signal is generated by 2PM at 960nm and by 3PM at 1300nm so the EAL corresponds to $l_e = 2/a$ at 960nm and $l_e = 3/a$ at 1300nm with *a* the slope coefficient of the linear regression.

Animal	EAL (1300nm)	r^2	EAL (960nm)	r^2	Dura thickness
Monkey 1	238.5	0.985	126.9	0.981	120
			327.7	0.978	155
			293.2	0.982	145
			237.7	0.993	170
Monkey 2	119.6	0.973	160.0	0.933	190
	357.1	0.952			240
			151.4	0.983	270
			244.3	0.991	230

We have less values for the cortex than the dura mater as it was not always possible to image deep enough to have a nice plot. Although we cannot check *in vivo*, the EAL of the cortex should not be impacted by the implantation of an imaging chamber so we can group the values from the two subjects. The average EAL of the cortex measured on these animals is **238.4 $\pm$ 97 μm** at 1300nm and **220.2 $\pm$ 71 μm** at 960nm. These estimations are close to the ones measured in the mice cortex (293μm at 1320nm and 154μm at 920nm [41]) despite a large standard deviation. Getting a more accurate measure of the EAL of the macaque monkey cortex would be interesting to compare it to that of the mouse and adjust the parameters of our model but using the one of the mouse cortex for now appears justified.

5.2.2 Dura thickness and maximum depth of imaging

Description

We have imaged the natural dura of two NHPs in a total of 17 positions for a dura thickness ranging from 120μm to 400μm. For each position, the thickness of the dura is measured manually, the power used for the imaging is stored and an estimation of the maximum imaging depth is made.

To measure the thickness of the dura, finding its surface is simple and straightforward as the fibers are well visible using their SHG is the red channel at 1300nm and the green channel at 960nm. However, the transition between the dura and the cortex is more difficult to pinpoint. For thin dura maters, it can be visible as there seems to be some reflection when imaging the bottom of the dura and fibers are no longer visible afterwards. For thicker membranes, the imaging quality is degraded at the bottom of the dura which makes is less visible. There usually are blood vessels in the interstitial space that can help find an upper bound for the thickness. The estimation is done at 1300nm because the imaging quality is higher.

These structural acquisitions of the SHG of the dura or the fluorescence of the vasculature are done using z-stacks. During the recordings, the intensity of the signal is kept within the mid-range of our PMTs and small z-stacks with varying power values are recorded to adjust for the change of intensity level as the depth evolves. Both the power used during the acquisitions and the depths are recorded.

Fluorescein dextran is used to visualize the vasculature using MPM. This allows us to record inside the cortex, at any position and depth. The maximum depth at which it is possible to discriminate blood vessels is considered as the maximum imaging depth, this can be characterized by an SNR higher than 1. This is again straightforward at 1300nm as there is little noise since we are power limited so the maximum depth is when we are using the maximum amount of power available and that no blood vessel can be seen anymore. During scanning, we see the single-frame image as well as a real-time preview of an average frame that helps for this. At 960nm, the images are noisier and there is a higher risk of damaging the tissue as we are not power limited so this is less precise.

Results and discussion

The maximum imaging depth that has been acquired with a signal-to-noise ratio higher than one is plotted against the corresponding dura thickness at that location in Figure 5.7. On the same plot is reported the theoretical limit for the imaging depth as per the model established in Section 4.2.5.

As previously mentioned, the setup is power limited at 1300nm so an SNR of

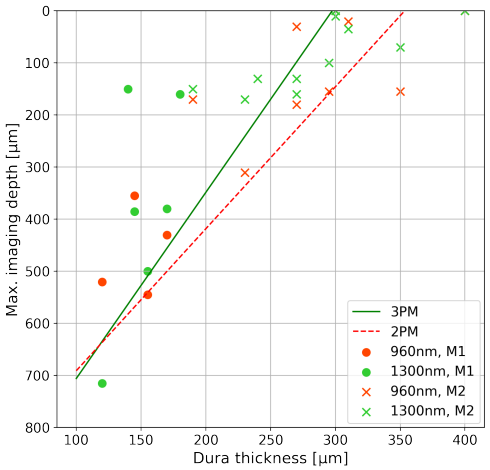

Figure 5.7 – Plot of the theoretical (red and green lines) and experimental (dots and crosses) maximum imaging depth inside the cortex of two rhesus macaque monkeys (M1 and M2) according to the thickness of dura for 2PM (960nm) and 3PM (1300nm). The model is the one from Section 4.2.5 using the most-mortem analysis for the estimation of the EAL of the dura and values from the mouse literature for the EAL of the cortex.

one is not reached and we could image deeper with more power although in the current configuration we're close to the limit of 100mW. In addition, the SNR is also impacted by an elevation of the background fluorescence which decreases the maximum imaging depth with respect to our model. As a result, the experimental evaluations of the maximum imaging depths should be lower than the predictions of the model.
Besides, the *in vivo* measurements of the EAL of the dura suggest that it may not be constant and could be increasing with the dura thickness. In particular, the post-mortem estimation of the EAL that is used here may be an underestimation of the *in vivo* value, especially for large thicknesses of dura.
It could be interesting to consider the EAL of the dura as a variable instead of a constant here as it seems to increase with the thickness of the dura, according to our *in vivo* measurements (see Section 5.2.1).

The experimental data are coherent with these observations : they are mostly below the theoretical limit up to a thickness of 250μm and become larger beyond that point where the EAL is the most underestimated.

5.2.3 Comparison of the natural dura with a regrown neomembrane

EAL of a neomembrane

In two other macaque monkeys, a durectomy was performed on the day of the chamber implantation. Yet, three months post-durectomy there was a 125μm-thick layer of granulation tissue at the surface of the cortex. This seems to be pial tissue rather than dura mater since the layer remains below the most superficial layer of blood vessels.
We have one z-stack at 1300nm and **the EAL of the neomembrane was 77.7μm** with a determination coefficient of 0.959. This is only one value but it is in the same range as the EAL of the post-mortem dura mater which was 80.7$\pm$5.3μm (see Section 4.2.4) and in the low range of the values acquired from *in vivo* recordings. This suggests that the EAL of a neomembrane be similar to that of a natural dura that has been pressed-down by an imaging chamber.
This is interesting and it would be nice to have additional data to confirm this result because it would mean that the granulation tissue that grows back after a durectomy is similar or worse with respect to the imaging quality. This would mean that leaving the dura mater in place could be a good alternative to a durectomy when using 3PM for long-term imaging.

Structure of the natural dura *in vivo*, post-mortem and of the neomembrane

Visually, the structure of the natural dura mater, post-mortem dura mater and the neomembrane that grows back after a durectomy are very similar. This suggests that positioning the imaging chamber on top of the dura mater and applying pressure on it thins it down without changing its mechanical properties by rearranging the fibers for example.
As for the neomembrane, it seems to be constituted of similar fibers as the dura mater but the fibers seem less organized. In the dura mater, the fibers are often aligned with an orientation that changes with depth as if there were a succession of sheets of fibers whereas the fibers of the neomembrane seem to be more randomly oriented. This can explain that the EAL be in the same range or lower for the neomembrane as the scattering is related to the structure of a sample.

5.3 Discussion

Following this study, one can wonder whether it is better to remove the dura or leave it in place to perform functional 3PM in NHPs.
The dura mater is a membrane that surrounds the cortex to protect it from mechanical constraints and bacterial infections. Omitting the durectomy therefore makes

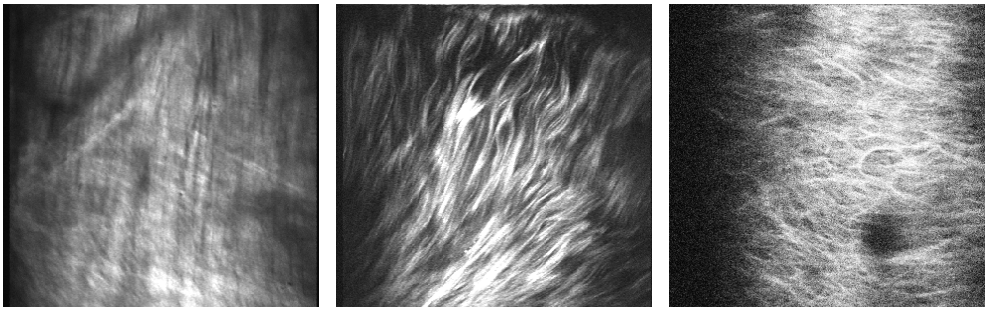

Figure 5.8 – Pictures of the natural dura (left), post-mortem dura (middle) and granulation layer (right) taken from recording. Each picture corresponds to the average of 10 frames. The fibers look similar in structure and are mostly going in the same direction for the dura mater (*in vivo* and *ex vivo*) whereas it is less regular for the granulation layer. The field of view is 620x630μm^2.

for a safer and **less invasive** setup. The durectomy can be a direct cause of damage to the cortex if blood vessels of the cortex are attached to the dura. Also in the longer term, there is evidence that removing the dura may disturb the vascular architecture [84] [98], so one can wonder if the cortical organization and activity is preserved.
Removing the dura also leads to a **greater risk of infections** of the cortex, which can be lethal if not treated immediately. Especially, the implantation of an imaging chamber remains a foreign body despite our efforts to increase its biocompatibility, and the evoked local inflammation can lead to the growth of 'opportunistic bacteria' : bacteria that are commonly present on the skin and do no lead to an infection in a healthy animal but can cause an infection if the immune response is lowered. Besides the risk for the animal, it is clearly not possible to record from an infected chamber because of the presence of pus or other secretion, and the evoked inflammatory response causes a faster growth of tissue at the surface of the cortex and can also compromise the integrity of the imaging chamber with the bone.

Yet, even if the natural dura thins down, it obscures or at least lowers the visibility of the cortex surface with the bare eye, or with epifluorescence imaging. The vasculature of the dura represents an additional layer of blood vessels above the cortex and the vasculature at the surface of the cortex is less visible. This makes the viral injections more complicated. Indeed, it is preferred to avoid blood vessels during the injections and to target regions with less blood vessels as large blood vessels can absorb the energy of the laser beam and prevent the imaging below it. The additional layer of blood vessels in the dura will therefore cast additional shadows on the neuronal populations below it, making them less visible.
Finally, leaving the dura in place is possible if the imaging chamber applies sufficient pressure onto it to thin it down, and there is no way to precisely quantify this pressure. So far we have no evidence that it is detrimental to the cortex. Al-

though previous papers have suggested that the cortex thins down below imaging chambers, it is not completely clear whether this was because of pressure applied by the cover glass or because of the damage done by repeatedly removing the neomembrane [30] [78].

In the end, for 3PM, I would recommend leaving the dura in place for recordings of imaging chambers that are intended for long-term experiments. This makes for a less invasive preparation, limiting the risks of infections spreading to the cortex. For short-term imaging or imaging sessions pushing the limits of the microscope in terms of imaging depth, removing the dura may be necessary.

5.4 Functional recordings from awake and behaving non-human primates

5.4.1 Adaptation of the setup

The setup has been designed for awake recordings of NHPs. As previously mentioned, the arm of the microscope has three translation stages and the objective can be rotated to accommodate for any position of the imaging chamber on the head of the animals.
NHPs are brought to the microscope in a transportation chair that can slide onto the optical table using a ramp. The animal is head-fixed and its head is then rotated depending on the position of the imaging chamber. The objective is positioned on top of the chamber and orthogonal to the imaging window during the imaging. A screen to present visual stimuli and speakers for auditory stimuli are available. A button-press system that can be rotated can also be positioned in front of the NHP chair for cognitive tasks. The sensory stimuli and responses of the animals are stored using TTL pulses that are collected and stored using a data acquisition card (USB-6001, National Instruments). The TTL pulses can then be aligned to the frame acquisition times for analysis using a TTL pulse that is recorded both by the data acquisition card and the Scanbox tower.

This allows to record awake NHPs while they are performing complex cognitive task and to match the neuronal responses to the nature and identity of the stimuli.

5.4.2 Awake and functional recordings in mice

This has been tested using mice. First, mice have been injected with GCaMP6s and implanted with an imaging chamber and a head-fixation bar according to the protocol described in Appendix C. The mice are then head-fixed for awake recordings.

Testing for bleaching

During functional recordings, the same area is recorded over a relatively long period of time in comparison with structural recordings using z-stacks. It is then important to check that the power needed to get a good signal level and a good SNR does not cause bleaching.

In order to check that, we have recorded the spontaneous functional activity of neurons within the anterior cingulate cortex during 24 minutes at a frame rate of 5.7Hz. The recording site is located 375μm deep in the cortex where neurons have been infected by GCaMP6s. The average power at the surface of the cortex is 24.5mW which was suitable to get a good signal level.

The average intensity of the frames has been plotted according to time to check for a decrease of signal intensity characteristic of photobleaching. The recording is averaged to see the location of the neurons and the average intensity of smaller areas surrounding neurons are also considered to check that bleaching is not visible at the scale of a single neuron (Figure 5.9 and Figure 5.10).

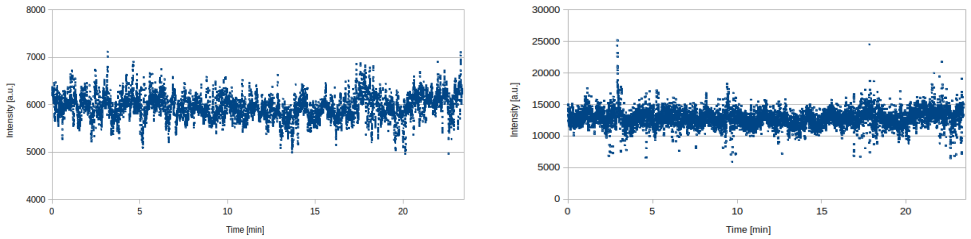

Figure 5.9 – Average intensity of the frames of a functional recording over time (left). Average intensity of a small area surrounding one neuron over time (right). The average intensity does not decrease during a 24-minute recording which suggest that the intensity is kept below the photobleaching threshold and is suitable for the analysis.

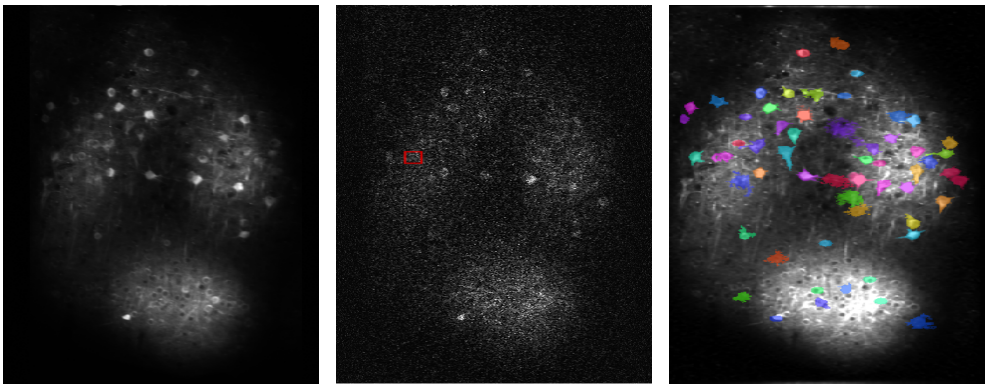

Figure 5.10 – Frame obtained by averaging all the frames of the recording, this is used to select areas surrounding neurons (left). Single frame from the recording that shows a satisfactory signal level and an example of selection to check the intensity of a single neuron (red square) (middle). Average frame obtained with Suite2P with the ROI superimposed (right). The field of view is 620x780μm^2, the recorded site is 375μm deep in the cortex and the average power at the surface of the cortex is 24.5mW.

The average intensity of the frames and neurons do not decrease over time during this recording which indicate that there is no photobleaching and that the power used during this recording is suitable for *in vivo* functional recordings in the mice.

Preprocessing functional data

Once functional data is acquired, it needs to be preprocessed : the file is registered and motion corrected, the regions of interest (ROI) are selected and the corresponding traces are plotted. To do these steps, we have decided to use Suite2P, a software developed by the Stringer Lab [6]. It has given us satisfactory results so far.

Here is an example using the same recording. The ROI are first established by Suite2P (using the pixels correlation) and can be manually adjusted to add or remove some (Figure 5.10). The traces are extracted for each ROI and can be used for further analysis (Figure 5.11).

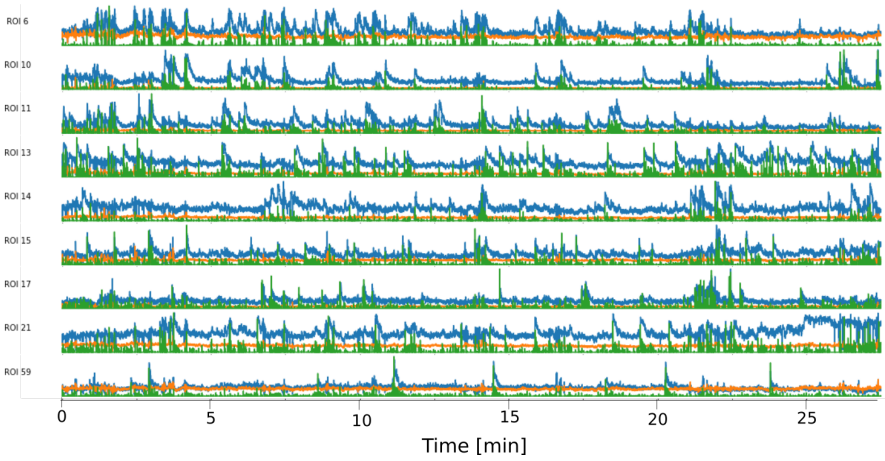

Figure 5.11 – Examples of traces obtained with Suite2P. Each line corresponds to the fluorescent signal of one ROI over the course of the recording. The cell fluorescence (blue), neuropil fluorescence (orange) and deconvolved signal (green) are extracted and plotted for each ROI using Suite2P.

5.4.3 Recording the functional activity of non-human primates

The aim of this setup is to record the functional activity of NHPs while they are performing cognitive tasks. In order to do so, the neurons need to be producing a genetically encoded calcium indicator such as GCaMP. We are using viral injections to locally infect the neurons with a virus that will trigger the production of GCaMP. However, finding good injection parameters is not easy. The expression level should be high enough to be recorded without using too much power but without saturating the neurons or else their functional activity may be impaired. The infection sites should be large with a good sparsity to be able to image large fields of view or to include the area responding to specific stimuli and to be able to record the activity of single neurons without too much background fluorescence

from the neuropile.

Since we have a very limited number of NHPs and that they are all very precious, we cannot perform a lot of tests on them. Therefore, some tests have been made in mice to infer on the impact of the injection volume, speed and titer. The surgeries and post-mortem analysis of the injection sites have been performed by Melissa Glatiny, an engineer in the team, together with Timo van Kerkoerle. Increasing either the volume or the injection speed results in a bigger injection site and increasing the volume or the titer results in a denser injection site.

We have performed viral injections in two NHPs using an AAV1 virus with an hSyn promoter to express GCaMP6s and mRuby. GCaMP6s is a green calcium indicator while mRuby is a red structural indicator so it can be used for motion correction. We have performed injections of 1.5 to 5μL with a titer of 1.5x10^{12} to 1.5x10^{13}vg/mL and an injection speed ranging from 25 to 1000nL/min. Trypan blue, a blue coloring, was mixed to the viral solution to help us visualize the injection sites on the day of the surgery and the eventual back-flow.

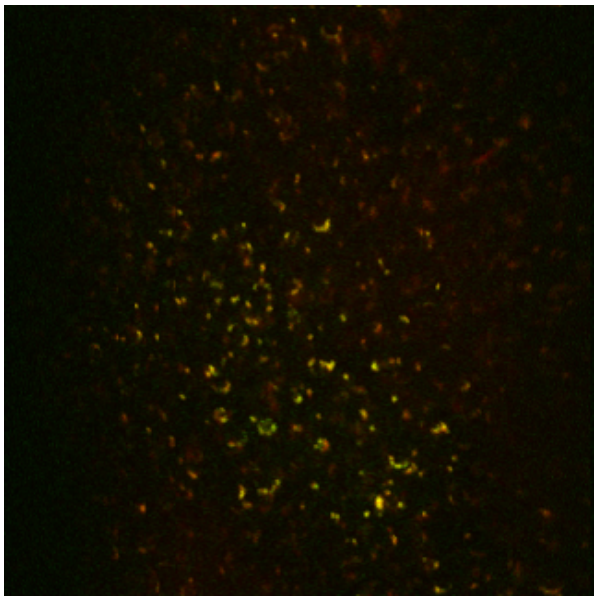

Figure 5.12 – Picture of neurons recorded *in vivo* under anesthesia by averaging 10 frames. The neurons are labelled with a green functional indicator (GCaMP6s) and a red structural indicator (mRuby).

One *in vivo* acquisition was performed in a NHP under anesthesia (sevoflurane) using 3PM at 1300nm. Expression was detected both in the green and the red channel corresponding respectively to functional and structural expression. Unfortunately, we have not been able to perform further experiments on this animal.

A post-mortem analysis has been performed by Melissa Glatiny to characterize the injection sites : the labeling was estimated to 25% which is suitable for us and the injection site that showed successful infection were large (5mm in diameter for the 5μL injections and 1mm for the 1.5μL injections). However, there was a high variability in the success rate of the injections (1/6 and 2/8) that we cannot explain.

This is a first proof of principal that shows that we are able perform viral injections within the cortex of NHPs and to detect the fluorescence using our setup despite a variability in the infection success.

For future viral injections, it is planned to use a virus with a Tet-Off enhancer (TTA-3G) to express GCaMP8s to have a better control on the expression level. A soma-restricted expression will also be used to minimize the neuropil and background fluorescence.
A Tet-Off enhancer is based on the administration of tetracycline to the animal to switch off the transcription process of the gene in order to control its expression level. A Tet-On enhancer also exists and the administration of tetracycline is then needed for the transcription of the gene to happen [99] [100].

5.4.4 Awake non-human primates recordings

Finally, we would like to record the activity from awake non-human primates to investigate cognitive questions involving conscious animals. One recording was made of the dura mater mater of one awake and head-fixed NHP to estimate the stability of the system. This animal had not been trained on remaining motionless or on eye-fixation prior to the recording and was therefore moving a lot which is representative of the most motion that we should have during an imaging session. The subject has a head-post with one central fixation point.
Body motions of the animal create large motion artefacts on the recording : the largest shifts are shown in Figure 5.13 and correspond to the animal turning its body around. These large motion artefacts are not compatible with the study of functional activity. However, the image goes back to the same position throughout the recording and is stable when the animal is motionless (Figure 5.13).

The first way to lower the motion artefacts is to train the animals on eye-fixation and on keeping their body straight and facing forward during the recordings which is very reasonable and required by most cognitive task. If the task requires large motions of the limbs, it may be necessary to check that it does not hinder the recording or take the motion into account in the task protocol so that the functional response is not studied during the motion of the animal.
The second possibility is to use a head-post with a second fixation point to increase

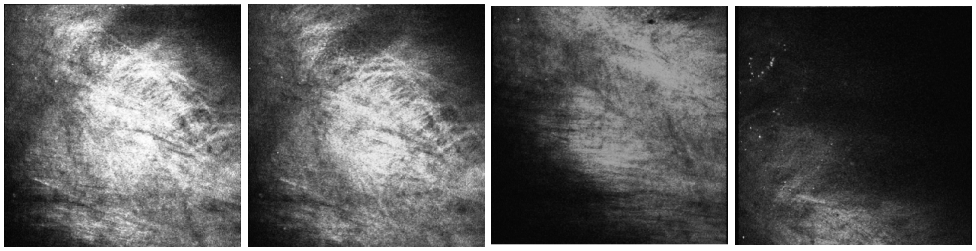

Figure 5.13 – Single frames from a 8.5 minute recording of the dura mater of an awake NHP. The first two images correspond to the first and last frames and show that the field of view is stable when the subject is. The last two images represent the largest motion visible during the recording and show the necessity to train the animal on remaining motionless during the recordings.

the stability of the system. We have already implanted one NHP with such a headpost to test this in the future (Figure 5.1).

5.5 Discussion on the use of two- and three-photon microscopy

The aim of the setup is to perform MPM in NHPs in a stable and reliable way to be able to investigate cognitive neuroscience questions.
Over the course of this project, we have used two-and three-photon microscopy extensively to image mice and macaque monkeys *in vivo*. In this section, I discuss the performance of two- and three-photon microscopy using our setup.

5.5.1 Expectations and theory

The main reason that has led us to 3PM in the first place is the possibility to image deeper and to image through the natural dura of the macaque monkey or a neomembrane.

Concerning imaging power, 2PM requires a smaller pulse energy at the focus to generate the same fluorescence signal and this is related to the difference in excitation probability. Therefore, the pulse energy of the excitation beam needs to be lower for 2PM to record signal from the surface of the sample.
Yet, because the EAL of the cortex is larger at 1300nm than at 920 or 960nm, there is a cross-over depth after which the pulse energy of the excitation beam and therefore the average power (if the repetition rate is the same) at the surface of the sample has to be larger for 2PM to generate the same signal [41] (Figure 5.14). The cross-over depth was experimentally measured to be between 600 and 700μm in the mouse cortex. In the presence of a membrane at the surface of the cortex, it would be shifted towards the surface. This means that 2PM is more energy-efficient until the cross-over depth and it is 3PM for deep imaging.
Using a larger pulse energy or average power leads to more tissue heating and a greater risk for damage. Yet, the limit in average power to avoid damage is larger for 2PM than 3PM (250mW against 100mW, see Section 3.2.1).
In mice, deeper imaging of the cortex was possible using 3PM without causing damage [40] [41] [38] [59].

Furthermore, it is expected that the background noise increases faster for 2PM which would decrease the corresponding imaging limit more significantly [38] [40] [101].

Therefore, we have decided to use 3PM to study the macaque monkey brain, expecting it to give us a larger imaging depth than 2PM. We have optimized our setup for 3PM and added an optical path for 2PM in order to compare the modalities.

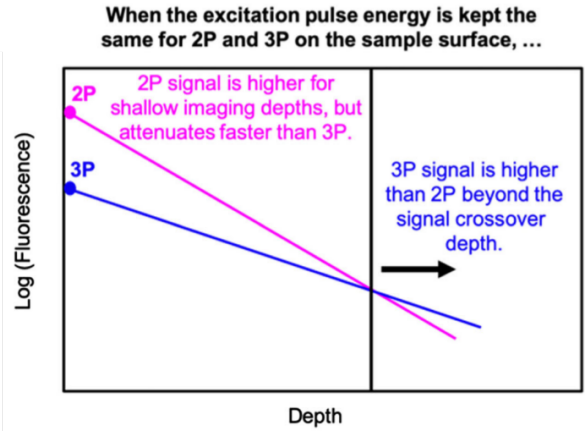

Figure 5.14 – Schematic of the signal generation using 2PM (pink) and 3PM (blue) inside the sample according to the imaging depth while the pulse energy of the excitation beam is the same. The 2PM signal is higher for shallow depths and there exists a cross-over depth after which the 3PM generated signal becomes higher. Image taken from [59].

5.5.2 Summary of the parameters and results of our study

In this study, 2PM has been performed at 960nm with a pulse width of 183fs while 3PM has been performed at 1300nm with a pulse width of 60fs and both are done with a laser that has a repetition rate of 2MHz. We have collected z-stacks of the vasculature of mice and NHPs to investigate the limit in imaging depth and some functional recordings were made in mice.

We have modelled the theoretical limit in imaging depth by taking into account the average power, absorption and scattering using data from the mouse literature. We have found that 3PM with a 2MHz laser would allow a much larger imaging depth than a common 2PM with a 80MHz laser but that it would be similar to a 2PM with a 2MHz laser (Figure 5.15).
Yet, since SNR is not taken into account in this model so far, we were still expecting a larger imaging depth for 3PM, even at 2MHz.

Throughout the project, we have been surprised to find little difference in the imaging performance between our 3PM and 2PM optical paths.
We have measured the maximum imaging depth over multiple imaging sessions in two macaque monkeys with a variable thickness of dura mater at the surface of the cortex. These measurements, unlike the model, take into account the SNR but there is no clear difference in the imaging depth. There is however a difference in the imaging quality.

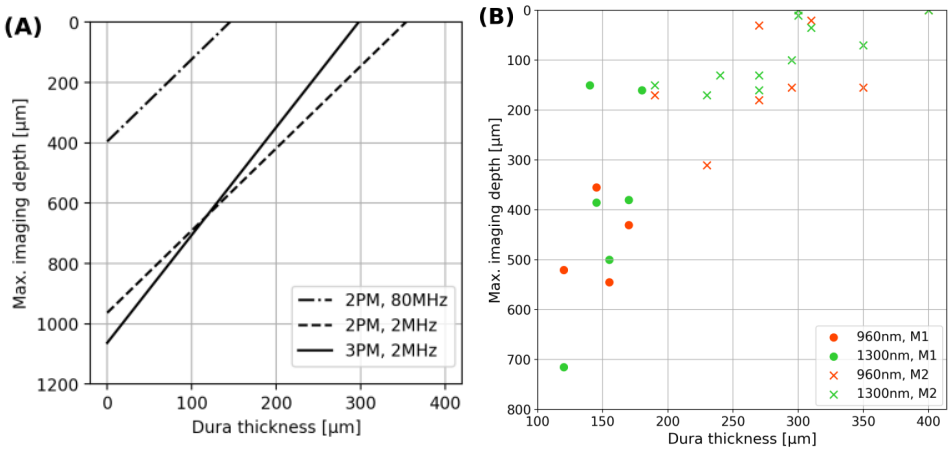

Figure 5.15 – (A) : Plot of the maximum imaging depth inside the cortex according to the thickness of the dura for 2PM using either 2MHz or 80MHz for the repetition rate of the laser and 3PM using 2MHz. (B) : Experimental imaging limit, taking the SNR into consideration.

5.5.3 Comparison of the imaging quality

We have not yet performed a detailed study of the SBR comparison between 2PM and 3PM but an example is shown in Figure 5.16. In the presence of dura mater or a neomembrane, the background level inside the cortex is larger for 2PM throughout the cortex and starting at its surface.
Besides, out-of-focus large blood vessels are visible using 2PM but not with 3PM, even at shallow depths (Figure 5.16 at depths -100 and -500μm).
This is an issue for the study of the vasculature where large blood vessels represent a big source of background fluorescence, it is not yet clear whether it will be problematic for functional recordings of labelled neurons. The density of the labelling, and whether or not the expression is restricted to the soma [9] [49] could play an important role in this.

5.5.4 Discussion

All in all, we have been pleasantly surprised with the imaging performance of our 2PM at 2MHz, especially as the current setup has been optimized for the 3PM path. In particular, it should be possible to get a better pulse width for 2PM than 183fs. Using the three-photon path is more enjoyable during the recording sessions thanks to the reduced noise and the absence of out-of-focus objects that can be confusing but we have not found a clear distinction in the imaging depth that would justify the need for 3PM. It seems possible to use a two-photon microscope to record from the NHP cortex if the laser has a low repetition rate to be able to use a larger pulse energy that is required to image deep. An optimized objective

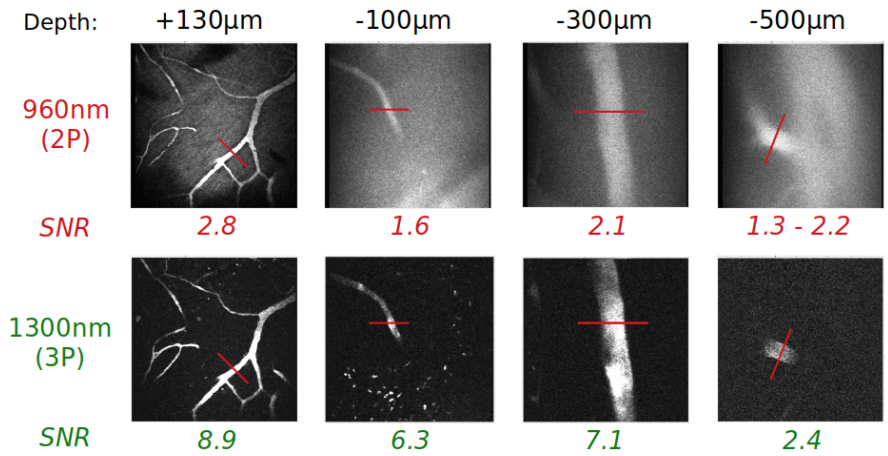

Figure 5.16 – Estimation of the signal-to-noise ratio (SNR) at different depths of the cortex. Each image corresponds to the average of 10 frames from a recording of a rhesus macaque monkey cortex using fluorescein dextran to image the vasculature. This recording took place at a location of the cortex with 120μm of dura mater at its surface and the surface of the cortex is used as the reference for the depth of recording.

with a high numerical aperture is also necessary for deep imaging, and local or sparse labelling is probably required [102].

Indeed, setting up and optimizing a three-photon microscope is more expensive and requires more knowledge in optics. The lower excitation probability of 3PM leads to the need of a shorter pulse width which means the addition of a negative dispersion unit and custom optics (lenses, filters and mirrors) optimized for 1300nm in terms of transmission or reflection. New lasers have recently been designed specifically for 3PM and can be used to set up a microscope faster, with less maintenance and with higher output power. In addition, the lower requirement in pulse energy and the higher limit in imaging power make 2PM more forgiving in terms of tissue damage.

In the current configuration, it would not help much to use a more powerful laser source. We are currently not reaching the maximum imaging depth at 1300nm when using the maximum power (70-90mW) as there was still little noise even at large depths. However, the limit to avoid damaging the tissue is 100mW average power at the surface of the cortex, so in the current imaging configuration there is little room to increase the laser power. Our setup is using resonance-galvo imaging to allow relatively fast imaging. 2MHz is about the slowest repetition rate that still gives a reasonable number of pixels per line (160).

One way to increase the maximum imaging depth would be to go to galvo-galvo imaging and using a lower repetition rate, this would allow an increase of the pulse energy while remaining below the 100mW time averaged power limit. For our application, the imaging speed is important, and the maximum imaging depth we reach with 2MHz is sufficient.

There still is a possibility to increase the maximum imaging depth, even at a repetition rate of 2MHz, by changing the scanning configuration. In the current configuration, we were already using unidirectional scanning where we were blanking every other line of the imaging plane, allowing us to double the pulse energy relative to bidirectional scanning. (The maximum time averaged power for bidirectional scanning is 180mW in our setup, so in that scanning configuration we always need to lower the power and therefore the pulse energy, limiting the maximum imaging depth.) It could be possible to further reduce the time averaged power by imaging every other frame for example, or image for a short period of time (e.g. 1 second) to collect one trial, and then blank the laser for an equivalent time period. Using this scanning configuration would allow us to further increase the pulse energy while keeping the maximum time averaged power at 100mW and doubling the pulse energy corresponds to an addition of $ln(2)$ times the EAL in imaging depth so about 200μm (see Equation 3.1). But this would require a more powerful laser source.

5.6 Conclusion

In this final chapter, we are testing the microscope on macaque monkeys. The design of the implants necessary to the imaging and surgical procedures are detailed. The imaging chambers and headposts have been designed to optimize their longevity to be suitable with the imaging of NHPs that have been trained for months on complex cognitive tasks and that have a life expectancy of over two decades. This encompasses the choice of the materials of the implants, the addition of rubber rings to seal the imaging chamber at each step, the surgical procedures and a regular cleaning of the wound margins after implantation to lower the risk of infections.

As a first step, MPM was performed on NHPs under anesthesia. This is simpler as it does not require any training from the animals and the imaging sessions can be longer although there are limited to once every two weeks per animal.
Acquisitions of the anatomy of the natural dura and cortex of two macaque monkeys were made using the second harmonic generation of the dura mater as well as the 2PM and 3PM signal of fluorescein dextran particles running in the blood vessels of the animals. This has enabled us to record z-stacks of the cortex and dura to evaluate their EAL. The goal was to get a more accurate value for dura mater than the one obtained from the post-mortem sample and to get a value for the cortex as well to update the model and have a better estimation of the maximum imaging depth. It appears that the EAL of the dura mater decreases as it shrinks down, either because of the pressure applied by the imaging chamber or during the preservation process of the post-mortem tissue. As for the EAL of the cortex, we observe variability in our measurements but the EAL is larger at 1300nm than at 960nm and is in the same order of magnitude as the one of the mouse mentioned in the literature.
In two other NHPs, the dura has been surgically removed during the implantation of the imaging chamber and a 125μm-thick neomembrane has regrown over the following three months. One acquisition suggests that its EAL be similar to that of the post-mortem dura mater. In this study, the maximum imaging depth has been modelled using the experimental values from the post-mortem dura mater but it can easily be adjusted to account for a neomembrane rather than dura mater by adjusting the EAL of the overlaying tissue.
In addition to the EAL, we have measured the maximum imaging depth using our setup at 960nm and 1300nm at different locations of the imaging chamber of two NHPs. These values have been plotted against our model. The general trend of the experimental data follows nicely the model for dura thicknesses below 250μm but for larger thicknesses we could image deeper than predicted. This corroborates with the hypothesis that the EAL of the dura may be decreasing as it becomes thinner, in agreement with the *in vivo* acquisitions.

The possibility to leave the dura mater in place to perform MPM in NHPs is discussed. The main advantage is the improved stability over time : the thickness of the dura mater remains stable or decreases over time which ensure a constant imaging quality of the ROI over time and the dura continues to protect the brain. However, the presence of the dura mater decreases the maximum imaging depth, at least for short-term imaging.

The next step for this imaging setup is to perform awake and functional recordings. It has been designed for this application with the large mobility of the objective that can accommodate to various positions of the imaging chamber while the animal can maintain its head straight. The setup can be used to present visual and auditory stimuli and the animals can respond using two buttons. All these events can be aligned to the recordings to study the cortical activity and this has been tested in mice so far.
The functional activity of mice has been recorded and preprocessed using Suite2P. Besides, we have tested viral injection parameters in two NHPs and the infection has been quantified using histology by a member of the team. We were also able to record in-vivo signal corresponding to both structural and functional activity in one animal.
Finally, we have done a first proof of concept in one NHP to quantify the motion artefacts and stability of the recording. This was done in an untrained animal that was moving a lot and large body motions are causing large motion artefacts that would not be compatible with the recording of functional activity. However, the imaging is stable enough to record from trained animals.

To conclude the project, the use of 2PM and 3PM with our setup and the aim of recording from the cortex of macaque monkeys is discussed. While 3PM leads to a better signal-to-background ratio and a better axial resolution in the presence of dura or a neomembrane, from the surface of the cortex to the limiting depth of imaging, there is no significant difference in the imaging depth. Therefore 2PM performed with a laser that has a repetition rate of 2MHz is sufficient to record in the cortex of macaque monkeys and presents the advantage to be simpler to set-up.

6 - CONCLUSION AND PERSPECTIVES

6.1 A summary of the work done during the PhD

Over the course of the PhD, a multi-photon microscopy setup dedicated to three-photon imaging at 1300nm has been developed and optimized to be able to image the cortex of macaque monkeys despite the presence of a dura mater of a neomembrane. The output power of the laser is 40W and the repetition rate has been set to 2MHz. The field of view is 620x630μm^2 with a frame rate of 15.6Hz using bidirectional scanning. We have reached a pulse width of 60fs and an averaged power at the sample of 150-200mW using bidirectional scanning and 70-100mW using unidirectional scanning. This was possible thanks to the addition of a dispersion compensation unit and a telescope to adjust the filling of the back aperture of the objective. Yet, the power remains the limiting factor for deep imaging using three-photon microscopy.
In parallel of the three-photon path, a two-photon microscopy path has been set up to directly compare two- and three-photon microscopy on a same setup. The pulse width is 183fs and the average power at the sample can reach 100mW using unidirectional scanning. The imaging depth is limited by the signal-to-background ratio.

This setup is dedicated to non-human primates and a number of technical developments have been made to make it possible.
First, surgical implants, a headpost and an imaging chamber, have been designed to stand the test of time, reduce the risk of infections, limit the motion artefacts during awake imaging and optimize the imaging area while keeping the implant to a reasonable size.
In addition, we are using an objective with a large numerical aperture of 0.95 and a large working distance of 8mm to accommodate for three-photon microscopy and the imaging chamber of the animals. The choice of the objective, together with the design of the imaging chamber, enables to image the full surface of the imaging window. Deep imaging is possible thanks to the development of an imaging gel made with deuterium oxide that transmits 97% of power as compared to 50% for distilled water or ultrasound gel.
An opaque and flexible cover has also been designed to fit on the objective and effectively reduce ambient light, the photons coming from the recording room (computer screens and visual stimuli presented to the animals), which create an elevation of the noise level.

With the goal of long-term and deep imaging of the non-human primate cortex,

imaging through the dura mater has been investigated.
The first step has been to use a sample of post-mortem dura mater to estimate its effective attenuation length using its second harmonic generation at 1300nm and 960nm. It was found to be 80.7$\pm$5.3μm at 1300nm and 56.5$\pm$10.1μm at 960nm. Using these values, a model has been elaborated to estimated the maximal depth that can be reached in the non-human primate cortex while being constrained by the maximal amount of power that can be used at the surface of the cortex without damaging it and the minimum amount of power at the focus that is required to elicit fluorescence.
Besides, fluorescent polystyrene beads embedded in agarose have been placed below the post-mortem dura mater sample to study the optical aberrations generated by the later. The apparent size of the beads have been measured in the absence of dura and below different thicknesses of the dura membrane. The dura mater is a scattering and inhomogeneous layer of tissue that can introduce optical aberrations that will in turn distort the point-spread-function of the microscope and lower its resolution. It was found that the resolution of the setup was preserved up to 155μm of dura for three-photon microscopy while it already starts deteriorating with 70μm of dura mater for two-photon microscopy and that the resolution drops beyond 165μm of dura mater for both modalities. Since the sample has gone through a fixation process, it is likely that the thicknesses aforementioned be underestimated by 20-30%.

Two non-human primates have been implanted with an imaging chamber while keeping the dura mater in place. Using the second harmonic generation of the dura, its effective attenuation length has been measured. For both subjects and for both two- and three-photon microscopy, it is increasing with the thickness of the dura mater. It ranges from 81 to 238μm at 1300nm for a thickness ranging from 145 to 400 μm. The hypothesis is that, as the imaging chamber presses more on the dura, it becomes thinner and denser and its effective attenuation length decreases to match a value similar to fixed dura mater. We have also been able to make one measurement of the effective attenuation length of a neomembrane that had grown after a durectomy in a macaque monkey and it was 77.7μm which is lower than the natural dura and similar to the fixed sample.
As the dura mater thins down in the imaging chambers, it becomes more transparent and the sulci become visible through it. Yet, there is no visible difference in the structure of in-vivo and post-mortem dura mater. They are made of fibers with a directional organization. The structure of the neomembrane that grows after a durectomy is similar but qualitatively less organized.
Using recordings of the vasculature, we have measured the maximum imaging depth for different thicknesses of dura mater using two- and three-photon microscopy at the same locations. We have been surprised to find that the limit in imaging depth decreases with the dura thickness was similar for both excitation processes, we

could image down to over 500μm into the cortex with 120μm of dura mater at the surface. This is mostly thanks to the low repetition rate of the laser that allows us to increase the pulse energy while maintaining a safe average power at the surface of the cortex. However, the main limitation for 2-photon imaging is the drop in signal-to-background ratio.

Finally, the set-up is meant for recordings of awake and behaving non-human primates. In addition to the technical developments already mentioned, events can be recorded and aligned to a recording for further analysis. The recording and pre-processing of functional activity has been tested in mice. We are able to record and extract traces of neurons using Suite2P and we have tested that there was no sign of bleaching during a recording lasting 24 minutes.
As for non-human primates, we have tested injections parameters in three macaque monkeys. *in vivo* we were able to visualize neurons infected with a structural and functional marker and an histology analysis was used to quantify the injection sites. The sites where the infection had been successful were satisfying but there was a large variability in the infection success. Future injections will be done with a tetracycline control of the transcription to control the expression level.

To conclude, we have designed and optimized a multi-photon microscope and surgical implants to successfully image the cortex of macaque monkeys down to 710μm at 1300nm and 520μm at 960nm with 120μm of natural dura mater at the surface. We have shown that it was possible to leave the intact dura mater during the implantation of the imaging chamber and to image through it afterwards. Assessing the correct pressure to apply on the dura can be explored further to obtain a thin dura without damaging the cortex. If one chooses to perform a durectomy instead, this setup allows imaging through a neomembrane and this is essential to long-term imaging. Throughout the project, we have been surprised by the performance of two-photon microscopy using 2MHz for the repetition rate of the laser and it represents a viable option for deep imaging of the cortex, even with a neomembrane. In addition to be easier and cheaper to install, it is more forgiving in terms of tissue damage as it requires a pulse energy 8 folds lower and has a power limit 2.5 times larger.
Current work is focusing on a detailed comparison of the signal-to-background ratio between two- and three-photon microscopy. Our current dataset allows using the vasculature, but this poses issues as the vasculature is not homogeneous making the measurements highly dependent on the pattern and diameters of the surrounding blood vessels, more so than on depth. In the end, it would be most relevant to study the signal-to-background ratio for neurons expressing a functional indicator, but this will be highly dependent on the type of expression that is used. Two-photon microscopy is more sensitive to out-of-focus fluorescence and has a lower axial resolution, so a sparse labeling and/or soma-restricted labelling would probably be

necessary for deep imaging.

6.2 Perspectives

6.2.1 Awake and functional recordings in macaque monkeys

We have demonstrated that the setup is ready for awake and functional recordings.
The first test of the microscope with an awake macaque monkey shows that the mechanical and optical sides of the project are working properly and compatible with awake imaging. We now required animals that are trained on passive fixation and training them on maintaining their paws at a fixed location would also be useful to limit the motion artefacts.
A headpost with two fixation points has also been implanted in an animal and a comparative study should be done to evaluate the motion artefacts with either one or two fixation points and see if it is necessary.
Besides, mostly vascular imaging has been performed on NHPs during this project but we have been able to image neurons and one next step to is perform viral injections in new subjects to record and characterize functional traces. This would also be the opportunity to compare the SNR at 1300nm and 960nm for different depths.

6.2.2 Study of attention in the visual area V4

Awake three-photon imaging in macaque monkeys opens up a lot of doors to study cognitive questions. In parallel to what has been discussed so far, we have started working on a project to study the cortical mechanisms of attention in the visual area V4 of the rhesus macaque monkey. This project requires NHPs able to perform cognitive tasks involving feature-based attention, the implantation of an imaging chamber that is stable over the course of the data acquisitions and hopefully longer to reuse the same animals and chambers for other projects and the possibility to record neurons from the first two layers of the cortex.

Background

At any given time, we are receiving a multitude of sensory information from our surrounding, too many to be processed by our brain. Selective attention is a crucial mechanism to filter this information and select only the behaviorally relevant ones. Spatial attention refers to the attention towards a specific location in space while feature-based attention refers to the attention towards a specific feature, irrelevant of its location.

Psychophysic studies have focused on spatial and feature-based attention at the behavioral level [103] [104] [105] [106]. Yet, the cortical mechanisms remain largely unknown.
Individual neurons have a **receptive field** : an area of the space that can stimulate it and a neuron can respond differently according to the stimulus that is in its receptive field. A **tuning curve** shows the response, measured by the firing rate, of a neuron to various stimuli. Neurons can be tuned to specific features such as color or orientation and there exists a spatial organization of the neurons according to there tuning in the macaque monkey brain, this is called **feature maps** [107] [108] [109] [110].

Project description

We are interested in the effects of feature-based selective attention at the level of large populations of individually defined neurons in macaque monkey V4. In particular, we would like to study the modulation of tuning curves of these neurons and the spatial organization of this modulation relative to feature maps.

Our setup can be used to record the functional activity of neurons while macaque monkeys are performing a well-controlled selective attention task. In order to characterize the effect of attention on tuning curves (either positive or negative), a clearly defined baseline is required. This can be obtained using a multi-modal task where attention is switched between visual and auditory stimuli, making the

visual stimuli be in turn at the focus of attention or ignored. This represents a challenging task for macaque monkeys and a classic passive fixation task could provide a baseline otherwise [111].
A delayed match-to-sample task would be used, similar to the one used in *David and al, 2008* [112], where a cue is followed by a string of stimuli and the subject has to signal when a stimulus matches the cue (Figure 6.1). The cue is used to control the object of attention of the animal while the distractors (the stimuli that do not match the cue) can be used to extensively map the area V4 to find feature maps as well as record the tuning curves of neurons.
The stimuli that have been envisioned are a subset of the ones used by the group of Anitha Pasupathy [113] as well as similar ones but rectilinear. These stimuli have already been used to map the V4 area where they elicit a strong enough response of the neurons. Furthermore, patches for curved versus rectilinear stimuli can be found in V4 [108] and could be used for this study.
These stimuli will be embedded in noise and most distractors will only be constituted of noise (Figure 6.2). These texture-defined figure-ground stimuli have been shown to strongly drive attention modulation in monkey V4 [114] [115] and lesion studies have also indicated a critical role of V4 [116] [117] [118]. By controlling the configuration of the background elements, we can study the effect of the attention template on local contours within the receptive field of the neurons, similar to a previous study by *McManus and al., 2011* [119]. In particular, we expect the shape that the animal is looking for will shift the orientation tuning of neurons in V4 to increase the detectability of the shape.
Using this, we want to extensively map out the effect of an attention template on a nearly complete population of neurons in a V4 receptive field. One of the specific questions is whether the neurons will try to align the peak or the slope of their tuning function in their search for the orientation of a local feature of the target stimuli.

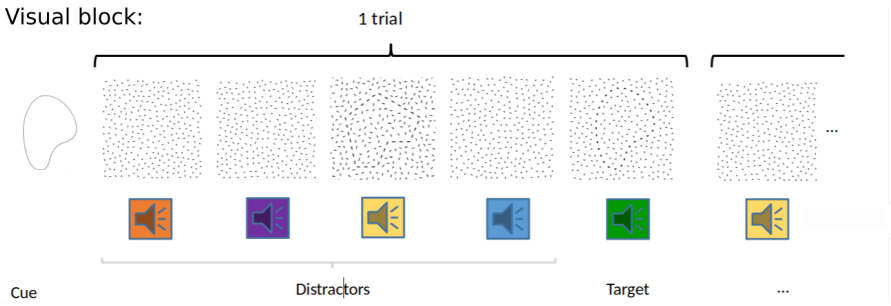

Figure 6.1 – Example of one visual block of the task. A visual cue is presented and followed by a string a sting a both visual and audio stimuli. The audio stimuli are irrelevant here and the animal has to signal (by pressing a button) when a stimulus matching the cue appears on the screen again. During an audio block, the cue would be a tone and the animal would have to respond for matching tones. If the multimodal task is too complicated, a purely visual task would be used.

Stimuli generation

The code to generate the stimuli has been written using GERT (Grouping Elements Rendering Toolbox) [120], a toolbox created to generate visual stimuli. With it, we can generate stimuli where a chosen contour is embedded in noise (Figure 6.2). The size and number of elements can be adjusted to tune the difficulty of the task. The animals should have a performance of about 80% so that it requires a high level of attention.

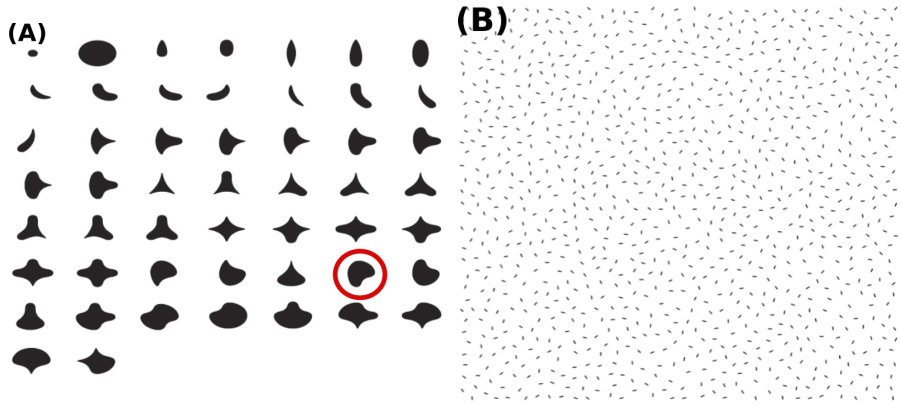

Figure 6.2 – (A) Visual stimuli used by the group of Anitha Pasupathy, image taken from [113]. (B) Example stimuli that would be used in the task made from the contour of the circled item and embedded in noise. The stimuli has been generated using GERT [120]

6.2.3 Human psychophysic study of the modulation of the extra-classical receptive field of neurons

As mentioned in the previous section, the receptive field of neurons is the area of the space that can elicit a response. The **extra-classical receptive field** (eCRF) is the area of the space that cannot directly elicit a response from a neuron but may modulate its activity by activating neighboring neurons that interact with this neuron.
We wanted to design a psychophysic experiment to study the impact of attention on the eCRF using a tilt-illusion experiment [121] [122] combined with a search task to tune the attention of participants. They would have been asked to look for a contour within a noisy stimulus which has been shown to strongly involve attention [114] [115]. The shape of the contour is designed to drive attention opposite the tilt-illusion effect.
Then, participants would be questioned on the orientation of one of the noisy background elements. Since feature-based attention is a global phenomenon, it will impact similarly neurons which receptive fields overlap the contour or the specific background element. This element of the background would be designed with a well-controlled surrounding that unables us to predict its perceived orientation without feature-based attention.

Our first step was to replicate a study [121] of the tilt-illusion. In this study, three segments are presented away from a fixation point. Participants have to give the orientation of the center element. However, the orientation of the two side elements, called flanks, can influence the perceived orientation of the center element [123].
Using the responses of a participant, it is possible to plot a psychometric curve from which the **'induced tilt'**, a measure of the influence of the orientation of the flanks on the perceived orientation of the target, can be estimated (Figure 6.3).
In their study, they obtain a positive induced tilt when the flanks are colinear with the target, meaning that the target seems to be attracted by the flanks. We have coded an online experiment to reproduce this result as a prerequisite to future tasks. However, we have observed a negative tilt when we tried to reproduce the task (Figure 6.3). We have only done it on ourselves and members of the team so we could try on a larger pool of subjects but we have tested the same parameters as in the article as well as to change them without success.

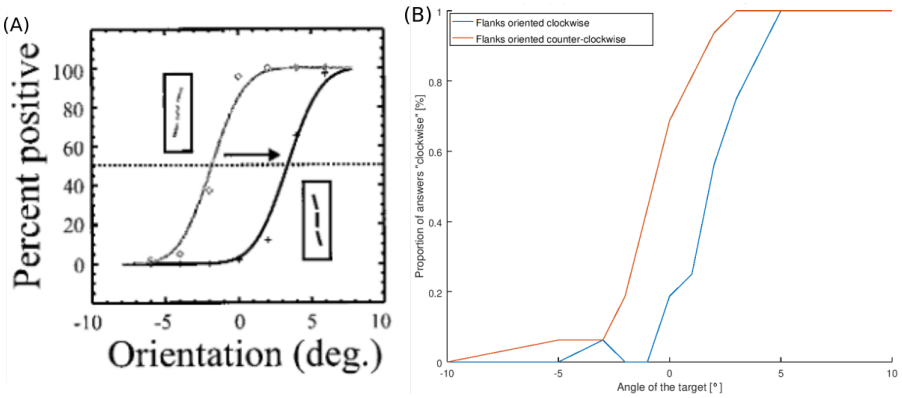

Figure 6.3 – (A) Psychometric curved obtained in the article, showing a positive induced tilt. Image taken from [121]. The induced tilt corresponds to half of the distance marked by the arrow. (B) One example psychometric curve obtained for one participant to our task. Plot of the proportion of answers stating that the target is oriented clockwise according to the actual orientation of the target. The blue curve corresponds to stimuli with flanks oriented clockwise and the orange one with flanks oriented counter-clockwise. This plot is similar to the one of the article but shows a negative induced tilt instead.

Appendices

A - Measure of the resolution

To measure the resolution of the microscope, fluorescent polystyrene beads (FluoSpheres carboxylate, Invitrogen, yellow-green (505/515), 0.5μm, 2% solids) are embedded in agarose gel. Then, they are imaged and the full-width at half maximum of their intensity along one direction in space is used as the resolution.

A.1 Preparation of the sample

The protocol of the preparation is as follow :

- agarose powder (Sigma-Aldrich) is diluted in distilled water with a ratio of 1.5 wt%
- the solution is heated up on a hot plate until the solution clears up and becomes homogeneous
- fluorescent polystyrene beads (FluoSpheres carboxylate, Invitrogen, yellow-green (505/515), 0.5μm, 2% solids) are added to the agarose to a concentration of 0.1 wt%
- a coverslip is placed on top before the solution becomes rigid and distilled water can be used to ensure that no air is trapped below the coverglass
- agarose is used to seal the edge of the coverslip and a layer of distilled water is kept at the surface of to avoid drying of the agarose

A.2 Image acquisition and data analysis

Data acquisition

First, before the acquisition, the alignment of the microscope is checked and adjusted so that the objective be orthogonal to the coverslip of the sample, that the illumination of the field of view be centered and optimized by tuning the dispersion compensation unit and the refractive index of the objective.

Then, a z-stack is acquired with 15 to 50 frames per plane with a 1μm step. The power may be adjusted to keep the signal level around the mid-range of the PMT. The recordings are converted into a tiff file using Matlab for further analysis.

Data analysis

Using Fiji, the frames of each plane are averaged and the "3D Objects Counter" module is used to locate the beads and extract their coordinates.

In python, the tiff file of the averaged z-stack is loaded as well as the coordinates of the beads. To estimate the resolution along one direction, a matrix with the intensity of the beads along the corresponding axis is generated.
For the lateral resolution, the analysis is done over 80 pixels that are centered on the bead's coordinates while for the axial resolution the analysis is done over the full length of the z-stack and the bead may not be centered (Figure A.1).
The intensity of the 5% brightest pixels of an orthogonal area are averaged at every step and used as the signal. This step corresponds to one pixel for the lateral resolution and to the step size of the z-stack for the axial resolution. The dimensions of the area are 2.2x2.8μm^2 for the lateral position and 2.2x2.2μm^2 for the axial resolution. Averaging the intensity of pixels over a plane is done to avoid an error due to an imprecision on the center position of the beads.

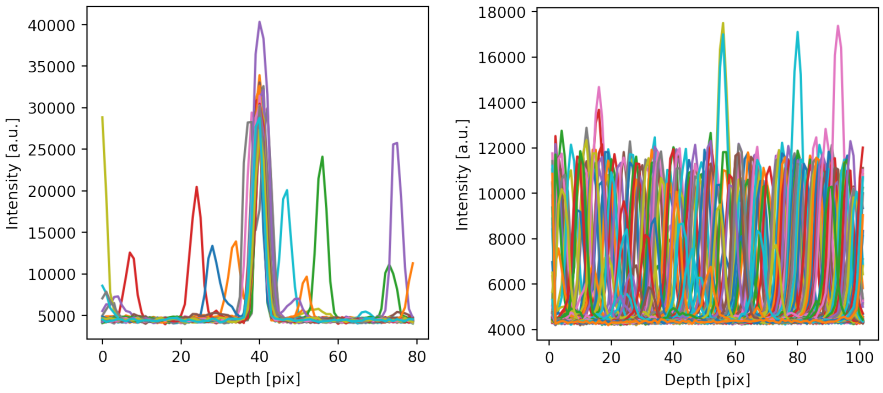

Figure A.1 – Example of the signal of all the beads of a z-stack along the axis X (left) and Z (right). The signals are aligned and centered on the beads for the lateral axis (the secondary peaks of intensity away from the center correspond to other beads located close to the considered one in the sample) whereas the intensity along the axial axis is measured for the full stack (100 steps here) and the beads are not aligned.

Baseline estimation

In order to normalize the data and fit it to a gaussian curve, an estimation of the baseline is required. This is done differently for the lateral axis than the axial one.
For the lateral resolution, the baseline is first calculated by averaging the signal of all the traces away from the bead. The signal is calculated over 80 pixels and the

first and last 20 pixels are used for this estimation of the baseline.
For the axial resolution, the beads are not aligned so another approach is used to find the baseline. For each step, an histogram of the signal is generated and the most frequent signal value is used as the baseline for that step.

Gaussian fit

The intensity of each bead is then normalized, plotted against distance and fitted to a gaussian curve. For the calculation of the coefficient of determination, the signal value is set to 0 away from the bead location to avoid that the presence of another bead nearby decrease it ('Signal bead only' in Figure A.2).
The resolution is given by the average of the full width at half maximum of the beads that have been fitted with coefficient of determination superior of 0.9.

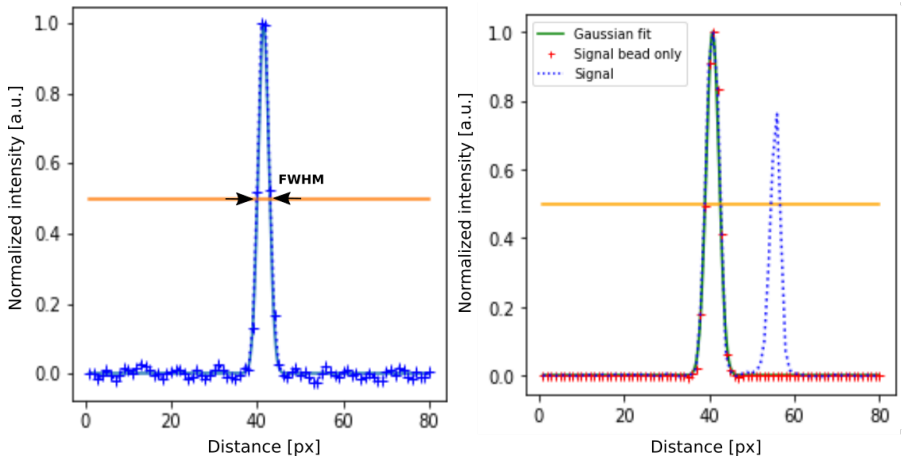

Figure A.2 – Example of the estimation of the apparent size of one bead along the direction X in pixels (left). Example plot of the signal, the gaussian fit and the modified signal so that it remains 0 away from the bead position. Thus, the presence of noise or a second bead does not degrade the coefficient of determination (right).

A.3 Estimation of the apparent size of beads positioned below 220μm of post-mortem dura mater

In Section 4.3.2, the apparent size of beads positioned below a layer of dura mater with a thickness ranging from 0 to 190μm is estimated. During the study, data for an additional thickness of 220μm has also been acquired.

Yet, the resulting apparent size is lower than expected (Figure A.3). This could be explained by a low signal-to-noise ratio (SNR). To measure the apparent size

of the beads, their signal is fitted to a gaussian curve and its full width at half maximum (FWHM) is estimated. However, in the presence of noise, part of the signal is below the noise level. The signal may still appear as a gaussian curve but with a lower FWHM and this would result in a smaller apparent size of the beads (Figure A.4).

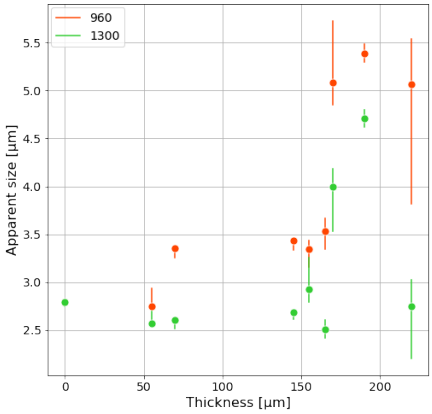

Figure A.3 – Plot of the apparent size of polystyrene fluorescent beads that are position below a post-mortem dura of varying thickness with the additional values with 220μm of dura mater. The apparent size is then smaller than expected.

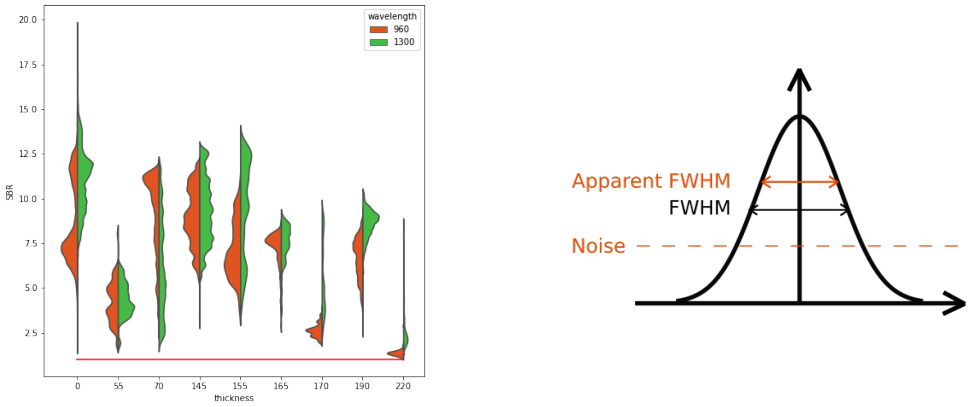

Figure A.4 – Signal-to-noise ratio of the beads for the different thicknesses of dura mater. An SNR of one (red line) correspond to the limit of signal detection. For a dura thickness of 220μm, the SNR is close to one (left). Schematic of a gaussian curve and its FWHM without noise (black) and its apparent FWHM in the presence of noise (orange). The apparent size is then under-estimated (right).

Estimation of the signal-to-noise ratio

To calculate the SNR, the signal of the beads and their surrounding noise level need to be estimated. To do so, a matrix of the pixel intensity surrounding the center coordinates (11x15x11 pix^3 i.e. 2.2x2.2x10.3 μm^3) of each bead is set up. The signal is then calculated as the maximum of that matrix and the baseline, as calculated previously, is used for the noise level. The SNR corresponds to the ratio of these two values.

In conclusion, the apparent size of the beads below a dura mater that is 220μm thick has been discarded from the study because the SNR is too close to 1 which can lead to an under-estimation of the size of the beads.

B - Deuterium oxide gel

During *in vivo* experiments on non-human primates, the objective that is used has a 8mm working distance and is designed for imaging under immersion. As our setup is power-limited at 1300nm, it is important to find an immersion medium compatible with a large working distance and with a large transmission of power at this wavelength.
Because of the working distance, a gel is required. Ultrasound gel is easy and cheap to use and stable over time but it absorbs a large portion of the power of the laser : compared to air, the transmission of power is divided by two through 8mm of ultrasound gel. However, deuterium oxide (D_2O) is known to have a large transmission so we have decided to develop a deuterium-oxide based gel [71] [72].

B.1 Preparation of the sample

The protocol is inspired from Rothstein et al. [73].

First, carbopol powder (Carbopol 940, Natural group) is mixed with deuterium oxide (151882, Sigma-Aldrich) at a concentration of 0.5wt% at room temperature until the solution is homogeneous.
Then, a strong base (10μL for sodium hydroxide solution per millimeter of solution) is mixed in the solution to create a gel. The viscosity of the gel can be modulated by changing the concentration of the strong base in the gel.
The gel is collected in a large volume syringe that will be used to dispense it as well. In order to remove air bubbles from the mixture, centrifugation can be used (10 seconds at 400cpf).

B.2 Testing the power transmission

To test the transmission of the deuterium oxide gel, the power is measured after travelling though 8mm of air, distilled water, ultrasound gel, a gel following the previous protocol but using distilled water instead of deuterium oxide and the deuterium oxide gel. The results, using air as a reference, are summarized in the following table.

Medium	Transmission
air	1
distilled water	0.51
ultrasound gel	0.50
distilled water gel	0.49
D_2O gel	0.97

Besides, the transmission over time has been tested for deuterium oxide to check its stability.

Liquid deuterium oxide and the prepared gel have been placed in a petri dish over the powermeter and the power transmission has been measured for one hour (Figure B.1). No decrease of transmission has been observed. However, measurements of transmission were performed 4.5h apart for the liquid solution and revealed a 20% loss which suggest some instability for longer periods. On the contrary, measurements done 5.5h apart using the deuterium oxide gel amounted to a 5 to 10% loss. Using gel that had just been prepared or gel that had stayed three months in a clear syringe at room temperature led to the same transmission so these storage conditions allow to preserve the optical properties of the gel over time.

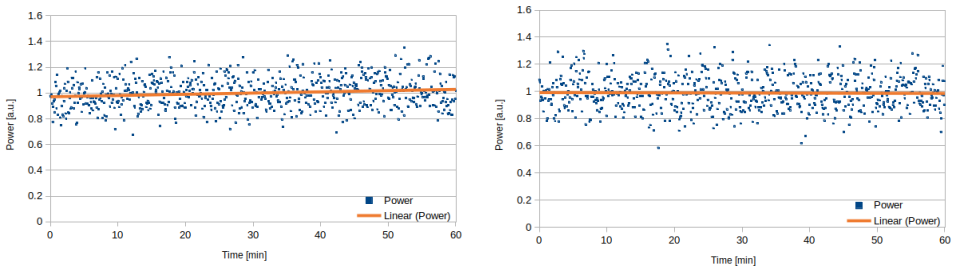

Figure B.1 – Power transmission through liquid deuterium oxide (left) and a deuterium oxide gel (right) over one hour. A linear regression is plotted and shows no decay of power over one hour.

This gel has been used for the *in vivo* recordings on non-human primates. The gel has been kept several months inside a transparent syringe at room temperature and used every two weeks during that period. There was no noticeable drop of power throughout four-hour recording sessions and the D_2O gel has been swapped at the end of a session to check if that would lead to an increase of signal but that was not the case. This further suggests that the gel is stable over time and suited for the recordings.

C - Mice surgeries : imaging window and head-bars implantation, viral injections

Within a single surgery, a craniotomy is performed, followed by viral injections and the implantation of an imaging window as well as head-bars that will be used to fix the head of the animal during imaging.
Here is the protocol received and copied with permission from Sara Jamali :

- Part of the right masseter is surgically removed to expose the temporal bone.
- A 5 mm in diameter craniotomy was drilled over the auditory cortex on the right hemisphere.
- Three injections of 150 nl of AAV1.Syn.GCaMP6s or AAV1.Syn.Flex.GCaMP6s ($1x10^{-12}$ vg.ml^{-1}), obtained from Addgene and Vector Core (Philadelphia, PA, USA), was performed with glass micropipettes and a programmable oil-based injector (Nanoliter 2000 & Micro 4 ; World Precision Instruments) at 30 nl.min^{-1}.
- The craniotomy was sealed with a glass window comprising a circular coverslip (5 mm diameter, pre-sealed with cyano-acrylate glue) and a metal post for head-fixation was implanted using two dental cements : Super-Bond C&B (Sun Medical Co. Ltd.) directly on the bone and Orthojet (Lang Dental, Wheeling, Illinois) for final sealing of the cranial window and the fixation post.
- Mice were given one week to recover from the surgery. Imaging was performed starting 4 weeks after the virus injection.

D - Résumé subtantiel en français

La microscopie multiphotonique est une technique d'imagerie qui repose sur la fluorescence et permet de visualiser l'activité fonctionnelle de neurones *in vivo*. Elle est devenue un outil essentiel pour les études sur la souris mais son application à de plus gros animaux se heurte à plusieurs obstacles. Il serait particulièrement avantageux de pouvoir l'appliquer aux macaques car ils représentent un modèle animal de choix pour comprendre les mécanismes neuronaux des fonctions cognitives de haut niveau telles que l'attention, la mémoire et la conscience. L'un des principaux facteurs limitant à l'imagerie chez ces animaux est la dure-mère. Cette couche de tissu épaisse et opaque enveloppe et protège le cerveau, mais elle est si épaisse chez les grands animaux qu'elle entrave l'imagerie. Elle est donc couramment enlevée mais cela conduit à une préparation hautement invasive et instable. L'objectif principal de ce travail est d'étudier la possibilité d'enregistrer l'activité fonctionnelle du cortex du macaque rhésus à travers la dure-mère naturelle.

Un microscope multiphotonique a été conçu avec des chemins optiques de microscopie à deux et trois photons pour pouvoir faire des enregistrements sur des primates non humains vigiles. La fréquence de répétition du laser est de 2MHz, ce qui permet une profondeur d'imagerie maximale à l'intérieur du cortex de 520μm à 960nm et 715μm à 1300nm en la présence d'une dure-mère de 120μm d'épaisseur à la surface. Le champ de vision est de 620x630μm2 avec une fréquence d'acquisition de 7,8Hz en utilisant un balayage unidirectionnel ou 15,6Hz avec un balayage bidirectionnel. La puissance moyenne maximale à la surface de l'échantillon est de 70 à 90mW à 1300nm et 150mW à 960nm.
Par ailleurs, l'installation prévoit l'emplacement pour un primate non humain et la possibilité d'enregistrer son activité fonctionnelle lorsqu'il effectue une tâche cognitive. En parallèle de la mise en place de cette installation, des implants chirurgicaux ont été développés pour une imagerie stable sur le long-terme et adaptée à l'imagerie de sujets vigiles.

En utilisant une étude *ex vivo* de la dure-mère d'un macaque rhésus, les aberrations optiques induites par celle-ci ont été étudiées en mesurant la diminution de la résolution spatiale du microscope pour une épaisseur variable de dure-mère. Cette étude révèle que la présence d'une dure-mère à la surface du cortex n'a pas d'impact significatif sur la résolutiondu microscope pour une épaisseur allant jusqu'à 150μm à 1300nm. Cette valeur pourrait être sous-estimée de 20 à 30%, ce qui correspond au coefficient de rétraction subi par les tissus conservés *ex-vivo*.
La longueur d'atténuation effective d'un tissu est une mesure caractéristique de la diminution relative de la puissance du laser au cours de sa transmission. Pour la dure-mère naturelle *ex vivo*, elle est estimée à 56.5$\pm$10.1μm à 960nm et 80.7$\pm$5.3μm

à 1300nm. Ces valeurs sont utilisées pour modéliser la profondeur maximale d'imagerie dans le cortex en tenant compte de la diffusion et de l'absorption d'énergie par le tissue. Elle limitée par l'énergie d'impulsion minimale nécessaire à une génération de fluorecence satisfaisante d'une part, et la puissance moyenne maximale à la surface du tissu permettant d'enregistrer sans risquer d'endomager le tissu d'autre part. La profondeur d'imagerie est étudiée en fonction de la fréquence de répétition du laser, de l'épaisseur de la dure-mère et de lu degré d'excitation de l'imagerie (à 960nm et 1300nm). Ce modèle est confronté à des données *in vivo* provenant de deux primates non humains.
A la suite d'une durotomie (résection chirurgicale de la dure-mère), une membrane peut se former à nouveau, appelée 'néomembrane'. Une mesure de la longueur d'atténuation effective d'une néomembrane a été effectuée et est comparable à la valeur de la dure-mère *ex vivo*.
Afin de compléter ce modèle, il est nécessaire d'étudier le rapport signal sur bruit pour l'imagerie à deux et trois photons qui pourrait limiter davantage la profondeur d'imagerie. Une étude préliminaire indique que le rapport reste suprérieur à un pour l'imagerie profonde à trois photon et que le bruit n'est donc pas un facteur limitant. Au contraire, pour l'imagerie à deux photons, le rapport signal sur bruit est dégradé dès la surface du cortex par la présence de la dure-mère à sa surface et la profondeur d'imagerie est limitée par celui-ci.

Des enregistrements fonctionnels ont été réalisés chez la souris. Il a été vérifié qu'aucun photoblanchiment (perte de fluorescence des molécules suite à des réactions chimiques) n'était détectable au cours d'un enregistrement fonctionnel d'une durée de 20 minutes en utilisant une puissance suffisante pour enregistrer l'activité des neurones. Les enregistrements fonctionnels sont ensuite prétraités avec Suite2P.
Les paramètres d'injection virale ont été testés chez trois macaques et nous avons enregistré l'activité structurelle et fonctionnelle de neurones pour l'un d'entre eux au moment de l'étude.

Enfin, la comparaison entre l'utilisation de la microscopie à deux ou trois photons pour l'étude du primate non humain est discutée ainsi que la pertinance d'une durotomie lors de l'implantation de la chambre d'imagerie.

En conclusion, nous avons mis en place et optimisé un microscope multiphotonique pour l'imagerie vigile et à long-terme du cortex de primates non humains et montré qu'il était possible d'enregistrer le cortex jusqu'à plus de 700μm de profondeur (ce qui correspond aux couches L2/L3) tout en gardant la dure-mère naturelle en place. Les propriétés optiques de la dure-mère ont été étudiées ainsi que son impact sur la qualité de l'imagerie du cortex et la profondeur d'imagerie.

Bibliographie

[1] Guoping Feng, Frances E. Jensen, Henry T. Greely, Hideyuki Okano, Stefan Treue, Angela C. Roberts, James G. Fox, Sarah Caddick, Mu-ming Poo, William T. Newsome, and John H. Morrison. Opportunities and limitations of genetically modified nonhuman primate models for neuroscience research. 117(39) :24022–24031.

[2] W. T. Newsome and J. A. Stein-Aviles. Nonhuman primate models of visually based cognition. 40(2) :78–91.

[3] Pieter R. Roelfsema and Stefan Treue. Basic neuroscience research with nonhuman primates : A small but indispensable component of biomedical research. 82(6) :1200–1204.

[4] Winfried Denk, J.H. Strickler, and Watt W. Webb. Two-photon laser scanning fluorescence microscopy.

[5] Chris Xu, Jeffrey Guild, Watt W. Webb, and Winfried Denk. Determination of absolute two-photon excitation cross sections by in situ second-order autocorrelation. *Opt. Lett.*, 20(23) :2372–2374, Dec 1995.

[6] Marius Pachitariu, Mario Dipoppa, Sylvia Schröder, L. Federico Rossi, Henry Dalgleish, Matteo Carandini, Kenneth D. Harris, and Kenneth D. Harris. Suite2p : beyond 10,000 neurons with standard two-photon microscopy. preprint, Neuroscience, June 2016.

[7] Jean Livet, Tamily A. Weissman, Hyuno Kang, Ryan W. Draft, Ju Lu, Robyn A. Bennis, Joshua R. Sanes, and Jeff W. Lichtman. Transgenic strategies for combinatorial expression of fluorescent proteins in the nervous system. *Nature*, 450(7166) :56–62, November 2007.

[8] Jiesi Feng, Changmei Zhang, Julieta E. Lischinsky, Miao Jing, Jingheng Zhou, Huan Wang, Yajun Zhang, Ao Dong, Zhaofa Wu, Hao Wu, Weiyu Chen, Peng Zhang, Jing Zou, S. Andrew Hires, J. Julius Zhu, Guohong Cui, Dayu Lin, Jiulin Du, and Yulong Li. A genetically encoded fluorescent sensor for rapid and specific in vivo detection of norepinephrine. 102(4) :745–761.e8.

[9] Yiming Chen, Heeun Jang, Perry W.E. Spratt, Seher Kosar, David E. Taylor, Rachel A. Essner, Ling Bai, David E. Leib, Tzu-Wei Kuo, Yen-Chu Lin, Mili Patel, Aygul Subkhangulova, Saul Kato, Evan H. Feinberg, Kevin J. Bender, Zachary A. Knight, and Jennifer L. Garrison. Soma-Targeted Imaging of Neural Circuits by Ribosome Tethering. *Neuron*, 107(3) :454–469.e6, August 2020.

[10] Simon Chamberland, Helen H Yang, Michael M Pan, Stephen W Evans, Sihui Guan, Mariya Chavarha, Ying Yang, Charleen Salesse, Haodi Wu, Joseph C

Wu, Thomas R Clandinin, Katalin Toth, Michael Z Lin, and François St-Pierre. Fast two-photon imaging of subcellular voltage dynamics in neuronal tissue with genetically encoded indicators. *eLife*, 6 :e25690, July 2017.

[11] Hod Dana, Yi Sun, Boaz Mohar, Brad K. Hulse, Aaron M. Kerlin, Jeremy P. Hasseman, Getahun Tsegaye, Arthur Tsang, Allan Wong, Ronak Patel, John J. Macklin, Yang Chen, Arthur Konnerth, Vivek Jayaraman, Loren L. Looger, Eric R. Schreiter, Karel Svoboda, and Douglas S. Kim. High-performance calcium sensors for imaging activity in neuronal populations and microcompartments. 16(7) :649–657.

[12] Seung-Jae Kim, Sandeep C. Manyam, David J. Warren, and Richard A. Normann. Electrophysiological Mapping of Cat Primary Auditory Cortex with Multielectrode Arrays. *Annals of Biomedical Engineering*, 34(2) :300–309, February 2006.

[13] Bahareh Ghane-Motlagh and Mohamad Sawan. Design and Implementation Challenges of Microelectrode Arrays : A Review. *Materials Sciences and Applications*, 04(08) :483–495, 2013.

[14] Jana Bürgers, Irina Pavlova, Juan E. Rodriguez-Gatica, Christian Henneberger, Marc Oeller, Jan A. Ruland, Jan P. Siebrasse, Ulrich Kubitscheck, and Martin K. Schwarz. Light-sheet fluorescence expansion microscopy : fast mapping of neural circuits at super resolution. *Neurophotonics*, 6(01) :1, February 2019.

[15] Dan D. Stettler, Homare Yamahachi, Wu Li, Winfried Denk, and Charles D. Gilbert. Axons and synaptic boutons are highly dynamic in adult visual cortex. 49(6) :877–887.

[16] Ming Li, Fang Liu, Hongfei Jiang, Tai Sing Lee, and Shiming Tang. Long-Term Two-Photon Imaging in Awake Macaque Monkey. *Neuron*, 93(5) :1049–1057.e3, March 2017.

[17] Kenichi Ohki, Sooyoung Chung, Yeang H. Ch'ng, Prakash Kara, and R. Clay Reid. Functional imaging with cellular resolution reveals precise micro-architecture in visual cortex. 433(7026) :597–603.

[18] Liron Sheintuch, Alon Rubin, Noa Brande-Eilat, Nitzan Geva, Noa Sadeh, Or Pinchasof, and Yaniv Ziv. Tracking the same neurons across multiple days in ca2+ imaging data. 21(4) :1102–1115.

[19] Yang Xie, Peiyao Hu, Junru Li, Jingwen Chen, Weibin Song, Xiao-Jing Wang, Tianming Yang, Stanislas Dehaene, Shiming Tang, Bin Min, and Liping Wang. Geometry of sequence working memory in macaque prefrontal cortex. *Science*, 375(6581) :632–639, February 2022.

[20] Alexandr Klioutchnikov, Damian J. Wallace, Michael H. Frosz, Richard Zeltner, Juergen Sawinski, Verena Pawlak, Kay-Michael Voit, Philip St. J. Russell, and Jason N. D. Kerr. Three-photon head-mounted microscope for imaging deep cortical layers in freely moving rats. 17(5) :509–513.

[21] Baris N. Ozbay, Gregory L. Futia, Ming Ma, Victor M. Bright, Juliet T. Gopinath, Ethan G. Hughes, Diego Restrepo, and Emily A. Gibson. Three dimensional two-photon brain imaging in freely moving mice using a miniature fiber coupled microscope with active axial-scanning. 8(1) :8108.

[22] Weijian Zong, Runlong Wu, Shiyuan Chen, Junjie Wu, Hanbin Wang, Zhe Zhao, Guoqing Chen, Rui Tu, Danlei Wu, Yanhui Hu, Yangyang Xu, Yao Wang, Zhuoli Duan, Haitao Wu, Yunfeng Zhang, Jue Zhang, Aimin Wang, Liangyi Chen, and Heping Cheng. Miniature two-photon microscopy for enlarged field-of-view, multi-plane and long-term brain imaging. 18(1) :46–49.

[23] Andres de Groot, Bastijn JG van den Boom, Romano M van Genderen, Joris Coppens, John van Veldhuijzen, Joop Bos, Hugo Hoedemaker, Mario Negrello, Ingo Willuhn, Chris I De Zeeuw, and Tycho M Hoogland. NINscope, a versatile miniscope for multi-region circuit investigations. 9 :e49987.

[24] Rajeevan T. Narayanan, Daniel Udvary, and Marcel Oberlaender. Cell type-specific structural organization of the six layers in rat barrel cortex. 11 :91.

[25] Demirhan Kobat, Nicholas G. Horton, and Chris Xu. In vivo two-photon microscopy to 1.6-mm depth in mouse cortex. *Journal of Biomedical Optics*, 16(10) :106014, 2011.

[26] Mark L. Andermann, Nathan B. Gilfoy, Glenn J. Goldey, Robert N.S. Sachdev, Markus Wölfel, David A. McCormick, R. Clay Reid, and Michael J. Levene. Chronic cellular imaging of entire cortical columns in awake mice using microprisms. 80(4) :900–913.

[27] Amiram Grinvald, D. Shoham, A. Shmuel, D. Glaser, I. Vanzetta, E. Shtoyerman, H. Slovin, C. Wijnbergen, R. Hildesheim, and A. Arieli. In-vivo optical imaging of cortical architecture and dynamics. In Uwe Windhorst and Håkan Johansson, editors, *Modern Techniques in Neuroscience Research*, pages 893–969. Springer Berlin Heidelberg.

[28] R D Frostig, E E Lieke, D Y Ts'o, and A Grinvald. Cortical functional architecture and local coupling between neuronal activity and the microcirculation revealed by in vivo high-resolution optical imaging of intrinsic signals. 87(16) :6082–6086.

[29] A Grinvald, R D Frostig, R M Siegel, and E Bartfeld. High-resolution optical imaging of functional brain architecture in the awake monkey. 88(24) :11559–11563.

[30] Li Min Chen, Barbara Heider, Graham V. Williams, Francine L. Healy, Benjamin M. Ramsden, and Anna Wang Roe. A chamber and artificial dura method for long-term optical imaging in the monkey. 113(1) :41–49.

[31] Hequn Zhang, Peng Fu, Yin Liu, Zheng Zheng, Liang Zhu, Mengqi Wang, Marwan Abdellah, Mubin He, Jun Qian, Anna Wang Roe, and Wang

Xi. Large-depth three-photon fluorescence microscopy imaging of cortical microvasculature on nonhuman primates with bright AIE probe in vivo. 289 :121809.

[32] Eric M. Trautmann, Daniel J. O'Shea, Xulu Sun, James H. Marshel, Ailey Crow, Brian Hsueh, Sam Vesuna, Lucas Cofer, Gergő Bohner, Will Allen, Isaac Kauvar, Sean Quirin, Matthew MacDougall, Yuzhi Chen, Matthew P. Whitmire, Charu Ramakrishnan, Maneesh Sahani, Eyal Seidemann, Stephen I. Ryu, Karl Deisseroth, and Krishna V. Shenoy. Dendritic calcium signals in rhesus macaque motor cortex drive an optical brain-computer interface. 12(1) :3689.

[33] Timo van Kerkoerle, unpublished observations.

[34] Shiming Tang, Yimeng Zhang, Zhihao Li, Ming Li, Fang Liu, Hongfei Jiang, and Tai Sing Lee. Large-scale two-photon imaging revealed super-sparse population codes in the V1 superficial layer of awake monkeys. *eLife*, 7 :e33370, April 2018.

[35] Nian-Sheng Ju, Shu-Chen Guan, Shi-Ming Tang, and Cong Yu. Macaque v1 responses to 2nd-order contrast-modulated stimuli and the possible subcortical and cortical contributions. *Progress in Neurobiology*, 217 :102315, 2022.

[36] Rundong Jiang, Ian M. Andolina, Ming Li, and Shiming Tang. Clustered Functional Domains for Curves and Corners in Cortical Area V4. preprint, Neuroscience, October 2019.

[37] Nicholas G. Horton, Ke Wang, Demirhan Kobat, Catharine G. Clark, Frank W. Wise, Chris B. Schaffer, and Chris Xu. In vivo three-photon microscopy of subcortical structures within an intact mouse brain. *Nature Photonics*, 7(3) :205–209, March 2013.

[38] Dimitre G Ouzounov, Tianyu Wang, Mengran Wang, Danielle D Feng, Nicholas G Horton, Jean C Cruz-Hernández, Yu-Ting Cheng, Jacob Reimer, Andreas S Tolias, Nozomi Nishimura, and Chris Xu. In vivo three-photon imaging of activity of GCaMP6-labeled neurons deep in intact mouse brain. *Nature Methods*, 14(4) :388–390, April 2017.

[39] Lina Streich, Juan Carlos Boffi, Ling Wang, Khaleel Alhalaseh, Matteo Barbieri, Ronja Rehm, Senthilkumar Deivasigamani, Cornelius T. Gross, Amit Agarwal, and Robert Prevedel. High-resolution structural and functional deep brain imaging using adaptive optics three-photon microscopy. 18(10) :1253–1258.

[40] Tianyu Wang, Dimitre G. Ouzounov, Chunyan Wu, Nicholas G. Horton, Bin Zhang, Cheng-Hsun Wu, Yanping Zhang, Mark J. Schnitzer, and Chris Xu. Three-photon imaging of mouse brain structure and function through the intact skull. *Nature Methods*, 15(10) :789–792, October 2018.

[41] Tianyu Wang, Chunyan Wu, Dimitre G Ouzounov, Wenchao Gu, Fei Xia, Minsu Kim, Xusan Yang, Melissa R Warden, and Chris Xu. Quantitative analysis of 1300-nm three-photon calcium imaging in the mouse brain. *eLife*, 9 :e53205, January 2020.

[42] Alberto Diaspro, Paolo Bianchini, Giuseppe Vicidomini, Mario Faretta, Paola Ramoino, and Cesare Usai. Multi-photon excitation microscopy. *BioMedical Engineering OnLine*, 5(1) :36, December 2006.

[43] Mengran Wang, Chunyan Wu, David Sinefeld, Bo Li, Fei Xia, and Chris Xu. Comparing the effective attenuation lengths for long wavelength in vivo imaging of the mouse brain. *Biomedical Optics Express*, 9(8) :3534, August 2018.

[44] Shu-Chen Guan, Sheng-Hui Zhang, Yu-Cheng Zhang, Shi-Ming Tang, and Cong Yu. Plaid Detectors in Macaque V1 Revealed by Two-Photon Calcium Imaging. *Current Biology*, 30(5) :934–940.e3, March 2020.

[45] Teppei Ebina, Yoshito Masamizu, Yasuhiro R. Tanaka, Akiya Watakabe, Reiko Hirakawa, Yuka Hirayama, Riichiro Hira, Shin-Ichiro Terada, Daisuke Koketsu, Kazuo Hikosaka, Hiroaki Mizukami, Atsushi Nambu, Erika Sasaki, Tetsuo Yamamori, and Masanori Matsuzaki. Two-photon imaging of neuronal activity in motor cortex of marmosets during upper-limb movement tasks. *Nature Communications*, 9(1) :1879, December 2018.

[46] Tsai-Wen Chen, Trevor J. Wardill, Yi Sun, Stefan R. Pulver, Sabine L. Renninger, Amy Baohan, Eric R. Schreiter, Rex A. Kerr, Michael B. Orger, Vivek Jayaraman, Loren L. Looger, Karel Svoboda, and Douglas S. Kim. Ultrasensitive fluorescent proteins for imaging neuronal activity. 499(7458) :295–300.

[47] Qian Chen, Joseph Cichon, Wenting Wang, Li Qiu, Seok-Jin R. Lee, Nolan R. Campbell, Nicholas DeStefino, Michael J. Goard, Zhanyan Fu, Ryohei Yasuda, Loren L. Looger, Benjamin R. Arenkiel, Wen-Biao Gan, and Guoping Feng. Imaging Neural Activity Using Thy1-GCaMP Transgenic Mice. *Neuron*, 76(2) :297–308, October 2012.

[48] Jung Eun Park, Xian Feng Zhang, Sang-Ho Choi, Junko Okahara, Erika Sasaki, and Afonso C. Silva. Generation of transgenic marmosets expressing genetically encoded calcium indicators. 6(1) :34931.

[49] Sverre Grødem, Ingeborg Nymoen, Guro Helén Vatne, Valgerdur Björnsdottir, Kristian Kinden Lensjø, and Marianne Fyhn. An updated suite of viral vectors for *in vivo* calcium imaging using local and retro-orbital injections. preprint, Neuroscience, May 2021.

[50] FPBase. Gcamp6f. https://www.fpbase.org/protein/gcamp6f/. Accessed : 2022-09-21.

[51] ThermoFisher Scientific. Fluorescein (fitc). https://www.thermofisher.com/search/supportSearch?query=dextran&persona=DocSupport&resultsPerPage=30&resultPage=7. Accessed : 2022-09-21.

[52] Fritjof Helmchen and Winfried Denk. Deep tissue two-photon microscopy. *Nature Methods*, 2(12) :932–940, December 2005.

[53] Murat Yildirim, Hiroki Sugihara, Peter T. C. So, and Mriganka Sur. Functional imaging of visual cortical layers and subplate in awake mice with optimized three-photon microscopy. *Nature Communications*, 10(1) :177, December 2019.

[54] Li-Chung Cheng, Nicholas G. Horton, Ke Wang, Shean-Jen Chen, and Chris Xu. Measurements of multiphoton action cross sections for multiphoton microscopy. 5(10) :3427.

[55] Hod Dana, Boaz Mohar, Yi Sun, Sujatha Narayan, Andrew Gordus, Jeremy P Hasseman, Getahun Tsegaye, Graham T Holt, Amy Hu, Deepika Walpita, Ronak Patel, John J Macklin, Cornelia I Bargmann, Misha B Ahrens, Eric R Schreiter, Vivek Jayaraman, Loren L Looger, Karel Svoboda, and Douglas S Kim. Sensitive red protein calcium indicators for imaging neural activity. 5 :e12727.

[56] A.P.E. Dispersion compensation & pulse compression for microscopy. https://www.ape-berlin.de/en/dispersion-compensation-pulse-compression/. Accessed : 2022-09-19.

[57] Hongying Liu, Tian Lan, Xiaomei Chen, and Guoqiang Ni. Dispersion compensation based on prism compressor. page 102521D, Yokohama, Japan, April 2017.

[58] Nicholas G. Horton and Chris Xu. Dispersion compensation in three-photon fluorescence microscopy at 1,700 nm. *Biomedical Optics Express*, 6(4) :1392, April 2015.

[59] Tianyu Wang and Chris Xu. Three-photon neuronal imaging in deep mouse brain. *Optica*, 7(8) :947, August 2020.

[60] Delphine Débarre, Nicolas Olivier, Willy Supatto, and Emmanuel Beaurepaire. Mitigating phototoxicity during multiphoton microscopy of live drosophila embryos in the 1.0–1.2 µm wavelength range. 9(8) :e104250.

[61] Scientifica. Galvo v resonant scanning guide. https://www.scientifica.uk.com/neurowire/galvo-or-resonant-scanning-guide. Accessed : 2022-09-20.

[62] Bhaskar Jyoti Borah and Chi-Kuang Sun. Construction of a high-NFOM multiphoton microscope with large-angle resonant raster scanning. 3(2) :101330.

[63] Bo Li, Chunyan Wu, Mengran Wang, Kriti Charan, and Chris Xu. An adaptive excitation source for high-speed multiphoton microscopy. *Nature Methods*, December 2019.

[64] R. Salomé, Y. Kremer, S. Dieudonné, J.-F. Léger, O. Krichevsky, C. Wyart, D. Chatenay, and L. Bourdieu. Ultrafast random-access scanning in two-

photon microscopy using acousto-optic deflectors. *Journal of Neuroscience Methods*, 154(1-2) :161–174, June 2006.

[65] Michael D. Young, Jeffrey J. Field, Kraig E. Sheetz, Randy A. Bartels, and Jeff Squier. A pragmatic guide to multiphoton microscope design. *Advances in Optics and Photonics*, 7(2) :276, June 2015.

[66] Martin Wilson. Collecting light : The importance of numerical aperture in microscopy. https://www.leica-microsystems.com/science-lab/collecting-light-the-importance-of-numerical-aperture-in-microscopy/, jul 2017. Accessed : 2022-09-21.

[67] Yusaku Hontani, Fei Xia, and Chris Xu. Multicolor three-photon fluorescence imaging with single-wavelength excitation deep in mouse brain. *Science Advances*, 7(12) :eabf3531, March 2021.

[68] Kaspar Podgorski and Gayathri Ranganathan. Brain heating induced by near-infrared lasers during multiphoton microscopy. 116(3) :1012–1023.

[69] F. Orlando Galashan, Hanna C. Rempel, Anneke Meyer, Eva Gruber-Dujardin, Andreas K. Kreiter, and Detlef Wegener. A new type of recording chamber with an easy-to-exchange microdrive array for chronic recordings in macaque monkeys. 105(6) :3092–3105.

[70] Thorlabs. Protected silver mirrors. https://www.thorlabs.com/newgrouppage9.cfm?objectgroup_id=903. Accessed : 2022-09-28.

[71] Yuxin Wang, Wenhui Wen, Kai Wang, Peng Zhai, Ping Qiu, and Ke Wang. Measurement of absorption spectrum of deuterium oxide (D $_2$ O) and its application to signal enhancement in multiphoton microscopy at the 1700-nm window. *Applied Physics Letters*, 108(2) :021112, January 2016.

[72] S. Kedenburg, M. Vieweg, T. Gissibl, and H. Giessen. Linear refractive index and absorption measurements of nonlinear optical liquids in the visible and near-infrared spectral region. 2(11) :1588.

[73] Emily C. Rothstein, Michael Nauman, Scott Chesnick, and Robert S. Balaban. Multi-photon excitation microscopy in intact animals. 222(1) :58–64.

[74] Giorgio M. Innocenti and Roberto Caminiti. Axon diameter relates to synaptic bouton size : structural properties define computationally different types of cortical connections in primates. 222(3) :1169–1177.

[75] Ahmet Kinaci, Wilhelmina Bergmann, Ronald LAW Bleys, Albert van der Zwan, and Tristan PC van Doormaal. Histologic comparison of the dura mater among species. 70(2) :170–175.

[76] Octavio Ruiz, Brian R. Lustig, Jonathan J. Nassi, Ali Cetin, John H. Reynolds, Thomas D. Albright, Edward M. Callaway, Gene R. Stoner, and Anna W. Roe. Optogenetics through windows on the brain in the nonhuman primate. 110(6) :1455–1467.

[77] Timo van Kerkoerle, Sally A. Marik, Stephan Meyer zum Alten Borgloh, and Charles D. Gilbert. Axonal plasticity associated with perceptual learning in adult macaque primary visual cortex. *Proceedings of the National Academy of Sciences*, 115(41) :10464–10469, October 2018.

[78] Azadeh Yazdan-Shahmorad, Camilo Diaz-Botia, Timothy L. Hanson, Viktor Kharazia, Peter Ledochowitsch, Michel M. Maharbiz, and Philip N. Sabes. A large-scale interface for optogenetic stimulation and recording in nonhuman primates. 89(5) :927–939.

[79] James M Anderson. Biological responses to materials. *Annual Review of Materials Research*, 31(1) :81–110, 2001.

[80] J. N. Turner, W. Shain, D. H. Szarowski, M. Andersen, S. Martins, M. Isaacson, and H. Craighead. Cerebral astrocyte response to micromachined silicon implants. 156(1) :33–49.

[81] D. H. Szarowski, M. D. Andersen, S. Retterer, A. J. Spence, M. Isaacson, H. G. Craighead, J. N. Turner, and W. Shain. Brain responses to micromachined silicon devices. 983(1) :23–35.

[82] Vadim S. Polikov, Patrick A. Tresco, and William M. Reichert. Response of brain tissue to chronically implanted neural electrodes. *Journal of Neuroscience Methods*, 148(1) :1–18, 2005.

[83] Michail Kastellorizios, Namita Tipnis, and Diane J. Burgess. Foreign body reaction to subcutaneous implants. In John D. Lambris, Kristina N. Ekdahl, Daniel Ricklin, and Bo Nilsson, editors, *Immune Responses to Biosurfaces*, pages 93–108, Cham, 2015. Springer International Publishing.

[84] Amos Arieli, Amiram Grinvald, and Hamutal Slovin. Dural substitute for long-term imaging of cortical activity in behaving monkeys and its clinical implications. 114(2) :119–133.

[85] Conor Liston and Wen-Biao Gan. Glucocorticoids are critical regulators of dendritic spine development and plasticity in vivo. 108(38) :16074–16079.

[86] Glenn J Goldey, Demetris K Roumis, Lindsey L Glickfeld, Aaron M Kerlin, R Clay Reid, Vincent Bonin, Dorothy P Schafer, and Mark L Andermann. Removable cranial windows for long-term imaging in awake mice. 9(11) :2515–2538.

[87] Homare Yamahachi, Sally A. Marik, Justin N.J. McManus, Winfried Denk, and Charles D. Gilbert. Rapid axonal sprouting and pruning accompany functional reorganization in primary visual cortex. 64(5) :719–729.

[88] Geoffrey Rolls. Process of fixation and the nature of fixatives. https ://www.leicabiosystems.com/fr-fr/knowledge-pathway/fixation-and-fixatives-1-the-process-of-fixation-and-the-nature-of-fixatives. Accessed : 2022-12-16.

[89] Daniel L. Adams, John R. Economides, Cristina M. Jocson, and Jonathan C. Horton. A biocompatible titanium headpost for stabilizing behaving monkeys. 98(2) :993–1001.

[90] Daniel L. Adams, John R. Economides, Cristina M. Jocson, John M. Parker, and Jonathan C. Horton. A watertight acrylic-free titanium recording chamber for electrophysiology in behaving monkeys. 106(3) :1581–1590.

[91] Noel Fitzpatrick, Thomas J. Smith, Catherine J. Pendegrass, Russell Yeadon, Michael Ring, Allen E. Goodship, and Gordon W. Blunn. Intraosseous transcutaneous amputation prosthesis (ITAP) for limb salvage in 4 dogs : Intraosseous transcutaneous amputation prosthesis. pages n/a–n/a.

[92] Alireza Nouri, Peter D., and Cuie We. Biomimetic porous titanium scaffolds for orthopedic and dental applications. In Amitava Mukherjee, editor, *Biomimetics Learning from Nature*. InTech.

[93] C N Elias, J H C Lima, R Valiev, and M A Meyers. Biomedical applications of titanium and its alloys.

[94] Xing Chen, Jessy K. Possel, Catherine Wacongne, Anne F. van Ham, P. Christiaan Klink, and Pieter R. Roelfsema. 3d printing and modelling of customized implants and surgical guides for non-human primates. 286 :38–55.

[95] R. Lemon. Methods for neuronal recording in conscious animals. by r. lemon. (pp. 162 ; illustrated ; £9.50.) john wiley & sons : Chichester. 1984. 14(3) :719–719.

[96] Walter A. Castelli and Donald F. Huelke. The arterial system of the head and neck of the rhesus monkey with emphasis on the external carotid system. 116(1) :149–169.

[97] Tony Hyun Kim, Yanping Zhang, Jérôme Lecoq, Juergen C. Jung, Jane Li, Hongkui Zeng, Cristopher M. Niell, and Mark J. Schnitzer. Long-term optical access to an estimated one million neurons in the live mouse cortex. 17(12) :3385–3394.

[98] Thom P. Santisakultarm, Calvin J. Kersbergen, Daryl K. Bandy, David C. Ide, Sang-Ho Choi, and Afonso C. Silva. Two-photon imaging of cerebral hemodynamics and neural activity in awake and anesthetized marmosets. 271 :55–64.

[99] Osamu Sadakane, Yoshito Masamizu, Akiya Watakabe, Shin-Ichiro Terada, Masanari Ohtsuka, Masafumi Takaji, Hiroaki Mizukami, Keiya Ozawa, Hiroshi Kawasaki, Masanori Matsuzaki, and Tetsuo Yamamori. Long-term two-photon calcium imaging of neuronal populations with subcellular resolution in adult non-human primates. 13(9) :1989–1999.

[100] Peichao Li, Anupam K. Garg, Li A. Zhang, Mohammad S. Rashid, and Edward M. Callaway. Cone opponent functional domains in primary visual cortex combine signals for color appearance mechanisms. 13(1) :6344.

[101] Patrick Theer and Winfried Denk. On the fundamental imaging-depth limit in two-photon microscopy. page 11.

[102] Wolfgang Mittmann, Damian J Wallace, Uwe Czubayko, Jan T Herb, Andreas T Schaefer, Loren L Looger, Winfried Denk, and Jason N D Kerr. Two-photon calcium imaging of evoked activity from l5 somatosensory neurons in vivo. 14(8) :1089–1093.

[103] Thomas Zhihao Luo and John H.R. Maunsell. Attentional Changes in Either Criterion or Sensitivity Are Associated with Robust Modulations in Lateral Prefrontal Cortex. *Neuron*, 97(6) :1382–1393.e7, March 2018.

[104] Thomas Zhihao Luo and John H.R. Maunsell. Neuronal Modulations in Visual Cortex Are Associated with Only One of Multiple Components of Attention. *Neuron*, 86(5) :1182–1188, June 2015.

[105] Taosheng Liu. Feature-based attention : effects and control. *Current Opinion in Psychology*, 29 :187–192, October 2019.

[106] John H.R. Maunsell and Stefan Treue. Feature-based attention in visual cortex. *Trends in Neurosciences*, 29(6) :317–322, June 2006.

[107] M. Li, F. Liu, M. Juusola, and S. Tang. Perceptual Color Map in Macaque Visual Area V4. *Journal of Neuroscience*, 34(1) :202–217, January 2014.

[108] Rundong Jiang, Ming Li, and Shiming Tang. Discrete neural clusters encode orientation, curvature and corners in macaque V4. preprint, Neuroscience, October 2019.

[109] Pinglei Bao, Liang She, Mason McGill, and Doris Y. Tsao. A map of object space in primate inferotemporal cortex. *Nature*, 583(7814) :103–108, July 2020.

[110] Rosa Lafer-Sousa, Bevil R. Conway, and Nancy G. Kanwisher. Color-Biased Regions of the Ventral Visual Pathway Lie between Face- and Place-Selective Regions in Humans, as in Macaques. *The Journal of Neuroscience*, 36(5) :1682–1697, February 2016.

[111] Dina V. Popovkina and Anitha Pasupathy. Task context modulates feature-selective responses in area V4. preprint, Neuroscience, April 2019.

[112] Stephen V. David, Benjamin Y. Hayden, James A. Mazer, and Jack L. Gallant. Attention to Stimulus Features Shifts Spectral Tuning of V4 Neurons during Natural Vision. *Neuron*, 59(3) :509–521, August 2008.

[113] Anitha Pasupathy and Charles E. Connor. Shape Representation in Area V4 : Position-Specific Tuning for Boundary Conformation. *Journal of Neurophysiology*, 86(5) :2505–2519, November 2001.

[114] Jasper Poort, Florian Raudies, Aurel Wannig, Victor A.F. Lamme, Heiko Neumann, and Pieter R. Roelfsema. The Role of Attention in Figure-Ground Segregation in Areas V1 and V4 of the Visual Cortex. *Neuron*, 75(1) :143–156, July 2012.

[115] Minggui Chen, Yin Yan, Xiajing Gong, Charles D. Gilbert, Hualou Liang, and Wu Li. Incremental Integration of Global Contours through Interplay between Visual Cortical Areas. *Neuron*, 82(3) :682–694, May 2014.

[116] Hans Supèr and Victor A. F. Lamme. Altered figure-ground perception in monkeys with an extra-striate lesion. 45(14) :3329–3334.

[117] William H. Merigan. Basic visual capacities and shape discrimination after lesions of extrastriate area v4 in macaques. 13(1) :51–60.

[118] Rujia Chen, Feng Wang, Hualou Liang, and Wu Li. Synergistic Processing of Visual Contours across Cortical Layers in V1 and V2. *Neuron*, 96(6) :1388–1402.e4, December 2017.

[119] J. N. J. McManus, W. Li, and C. D. Gilbert. Adaptive shape processing in primary visual cortex. *Proceedings of the National Academy of Sciences*, 108(24) :9739–9746, June 2011.

[120] Maarten Demeyer and Bart Machilsen. The construction of perceptual grouping displays using GERT. 44(2) :439–446.

[121] Mitesh K. Kapadia, Gerald Westheimer, and Charles D. Gilbert. Spatial Distribution of Contextual Interactions in Primary Visual Cortex and in Visual Perception. *Journal of Neurophysiology*, 84(4) :2048–2062, October 2000.

[122] Timothy Ledgeway, Robert F. Hess, and Wilson S. Geisler. Grouping local orientation and direction signals to extract spatial contours : Empirical tests of "association field" models of contour integration. *Vision Research*, 45(19) :2511–2522, September 2005.

[123] David J. Field, Anthony Hayes, and Robert F. Hess. Contour integration by the human visual system : Evidence for a local "association field". *Vision Research*, 33(2) :173–193, January 1993.